Understanding r-process Nucleosynthesis in the Milky Way

Author:

Christopher HAYNES

Supervised by:

Dr. C. KOBAYASHI

Centre for Astrophysics Research

School of Physics, Astronomy and Mathematics

University of Hertfordshire

Submitted to the University of Hertfordshire in partial fulfilment of the requirements of the degree of Doctor of Philosophy.

September 2019

Abstract

Elements heavier than Fe are formed by neutron capture processes when fusion becomes energetically unfavourable; the slow s-process and site are reasonably well understood, but the rapid r-process site is still a highly debated topic. In this thesis I will discuss the current best understanding of both the s-process and r-process, including potential sites. I also discuss the modelling of galaxies using smoothed particle hydrodynamics simulations with the inclusion of nucleosynthesis models to simulate the chemical evolution of galaxies. I then present the results of such chemodynamical simulations including nucleosynthesis yields for neutron star mergers, magneto-rotational supernovae, electron capture supernovae and neutrino driven winds. Using the [Eu/(Fe,α)] - [Fe/H] relation I show the neutron star mergers are unlikely to be able to drive r-process enrichment in the early universe but that magneto-rotational supernovae, or a combination of sources including them, may be able to. I then include a metallicity dependence in the magneto-rotational supernova model, and show that a combined model with neutron star mergers and electron-capture supernovae gives an excellent match to observations of [(Eu, Nd, Dy, Er, Zr)/(Fe, α)]. Finally I discuss the effects of supernova feedback on chemical evolution. I compare four models: a thermal model, a thermal model with a kinetic component, a stochastic model and a mechanical model and show that the kinetic, stochastic and mechanical models can suppress the star formation within isolated dwarf disc galaxies when using optimal parameters and that this has little effect on the fraction of metals ejected from the galaxy.

Declaration

I declare that no part of this work is being submitted concurrently for another award of the University or any other awarding body or institution. This thesis contains a substantial body of work that has not previously been submitted successfully for an award of the University or any other awarding body or institution.

The following parts of this submission have been published previously and/or undertaken as part of a previous degree or research programme:

1. Chapter 4: This chapter has been accepted and published as Haynes & Kobayashi 2019 in *Monthly Notices of the Royal Astronomical Society*, **Volume 483, Issue 4, March 2019, Pages 5123 - 5134**

2. Chapter 5: This chapter is a completed paper at the time of writing and due to be submitted to *Monthly Notices of the Royal Astronomical Society*.

Except where indicated otherwise in the submission, the submission is my own work and has not previously been submitted successfully for any award.

Acknowledgements

Contents

List of Figures

List of Tables

Chapter 1

Introduction and Motivation

The nucleosynthesis of chemical elements is key to our understanding of the universe as a whole. For over 90 years efforts have been made to understand the abundances we observe in our solar system, galaxy and the wider universe and to understand how these elements are created. The mechanisms by which each element is synthesised can broadly be split up into several groups; whilst some of these are well understood, others are still very much active areas of research.

Galactic archaeology is built on the premise of chemical recycling throughout the galaxy. Over time the originally pristine gas is polluted with the metals forged in a host of different astrophysical sites; the primary site for this is the process of stellar nucleosynthesis. At the end of their lives these stars often eject large quantities of their matter in the surrounding gas through stellar winds and violent supernovae and the gas becomes enriched with metals. Eventually this gas can form stars itself, which build upon the metals formed previously and again recycle their material into the surrounding gas. Galactic archaeology is the process of trying to understand the conditions and processes that resulted in the metal content of the stars we observe; in essence, to try and reverse engineer the enrichment process from the final stellar abundances.

Big bang nucleosynthesis accounts for the production of H, He and Li shortly after the formation of the universe. Proton-capture elements are formed by the fusion of light elements and hydrogen nuclei, including C, N, O, F, Na, Mg and Al, and the α elements, C, O, Mg, Si, S and Ca, are formed similarly by the capture of helium nuclei. Both of these processes take place in the fusion reactions that power stars and synthesise the elements up to the iron peak elements (Sc through to Zn). To fuse elements heavier than this is not energetically favourable; instead they are formed largely through the process of neutron capture. Discussion of this began with Burbidge et al. (1957) and Cameron (1957) which gave rise to the suggestion that almost all heavy elements could be produced using two processes: slow neutron capture (s-process) and rapid neutron capture (r-process). These processes both used the same mechanisms of neutron capture and subsequent beta decay but differed in the relative timescales. The s-process had a

neutron capture timescale much longer than that of beta decay so would always decay prior to absorbing another neutron. As a result it would operate very close to the valley of stable nuclides over a long time period. The r-process had a much faster neutron capture timescale and was able to undergo multiple neutron captures before beta decay would occur. In doing so it created unstable very neutron rich isotopes over a shorter time, operating far from the valley of stability before decaying back to stable nuclides.

In the time since the terms were coined a number of other processes have arisen; the p-process (Arnould and Goriely, 2003) which describes the capture of protons to form proton-rich stable isotopes, the i-process (Cowan and Rose, 1977) which provides an intermediate to the s-process and r-process and the ν-process (Woosley et al., 1990) which takes account of the effects of extremely high neutrino flux on heavy elements. However, these processes contribute only a small proportion of galactic heavy elements, with the majority still thought to be contributed by the s-process and r-process.

Both the s-process and r-process require different physical conditions to operate. Relatively recent works have shown that the steady neutron flux required for the s-process to operate can occur in both the centre of rotating massive stars (Prantzos et al., 1990; Frischknecht et al., 2016) and the He burning layers of low mass AGB stars (Smith and Lambert, 1990; Bisterzo et al., 2011).

While the s-process sites are reasonably well understood the r-process sites remain a much debated topic in the galactic archaeology community. Historically there have been four main proposed sites: the neutron rich dynamic ejecta of neutron star (NS) mergers (Lattimer and Schramm, 1974; Freiburghaus et al., 1999b), the accretion discs formed around the cores of rapidly rotating, massive, highly magnetised stars (Cameron, 2003), the O-Ne-Mg cores of 8 - 10 $M_\odot$ stars (the exact mass range depends on metallicity) electron capture supernovae (Wanajo et al., 2011) and in the neutrino-driven winds of NS-forming supernovae (Wanajo et al., 2001). Recent observations of the gravitational wave event GW170817 (Abbott et al., 2017b), thought to be the result of a NS-NS merger, and the kilonova associated with the simultaneous astronomical transient AT2017gfo (Valenti et al., 2017) have strongly suggested that NS mergers must contribute in some way to the galactic r-process; analysis of the kilonova found evidence of r-process production including lanthanides, e.g, (Tanaka et al. 2017).

Broadly speaking, galactic archaeology models attempt to simulate the chemical evolution of a model galaxy by considering the theoretical nucleosynthesis yields. The simplest of these models are galactic chemical evolution (GCE) models which combine the nucleosynthesis yields with an assumed star formation history to provide an abundance trend evolving with time. At the opposite end of the scale are full chemodynamical simulations which model the 3D movement of stars and gas hydrodynamics in time from cosmological initial conditions. These also include

physical processes such as gas cooling, feedback from supernovae events and the distribution of nucleosynthesis products into the evolving interstellar medium (ISM).

The introduction of supercomputers and parallel computing is responsible for the rise of chemo-dynamical simulations as it has become possible to track the evolution of multiple elements over time. The most common methods used to model the hydrodynamics are smoothed particle hydrodynamics (SPH, Lucy 1977, Gingold and Monaghan 1977), where gas, stars and dark matter are represented by discrete particles and interactions are calculated between those particles after accounting for the effect of other nearby particles, and grid methods, where space is divided into a grid and the quantities of gas, stars and dark matter are measured by their mass within grid spaces and interactions are calculated between these spaces (such as adaptive mesh refinement, Berger 1989). Both particles and grid spaces can also be used to trace the mass of chemical elements they contain, as this can impact physical processes (such as cooling). It is possible for chemodynamical simulations to model formation of Milky Way-type galaxies from cosmological initial conditions, including star formation and nucleosynthesis yields (e.g. Kobayashi and Nakasato 2011). These are particularly useful in galactic archaeology as nucleosynthesis models can be tested by comparing the predicted chemical abundance trends, patterns and scatters with the values observed in stars.

In this thesis I will present my research into nucleosynthesis using these chemodynamical simulations, with a particular focus on the r-process. The core question that I attempt to address is the astrophysical site of the r-process. To this end, Chapter 2 will present a review of the theory behind galactic nucleosynthesis, including s-process and r-process sites and operation. In chapter 3 I discuss the nucleosynthesis code I use and the models implemented. In chapters 4, 5 and 6 I present three papers written during the course of my research. The first is a comparison of r-process sites included in chemodynamical simulations, which finds that magneto-rotational supernovae (MRSNe) are expected to play a key role in the r-process in the early universe). The second is an expansion of the MRSNe model from the previous paper to include metallicity dependence and presents a best fit model to the observed galactic elemental abundances. This model shows an improved fit on the previous model and has the benefit of including NS mergers (which are expected to contribute to the r-process based on observations). The last paper is a discussion and comparison of supernova feedback models and the effect on elemental abundances. Finally, chapter 7 presents a summary of the thesis and discussed possible further work.

Chapter 2

Theory and Background

2.1   Nucleosynthesis and Elements Lighter than Iron

The question of how each element is produced is fundamental to the understanding of our Galaxy and the universe as a whole. The very first elements to occur were the H, He and Li produced in the Big Bang. Beyond that the majority of light elements (up to the Fe-peak) are formed in the fusion process that powers stars. The Fe-peak elements sit at the peak of the nuclear binding energy curve: lighter elements can fuse to release the energy that counteracts the gravity of stars. Heavy elements are instead formed predominantly via neutron capture, first outlined in Burbidge et al. (1957) and Cameron (1957). In this Chapter I outline the current understanding of heavy element nucleosynthesis, beginning with the basics of neutron capture and moving on to the production of the heaviest elements via neutron capture processes. This will be the primary focus of the chapter, including discussion of the processes themselves and potential astrophysical sites.

2.2   Neutron Capture

At its core the neutron capture process is very simple. Where the fusion of heavy elements would require energy to take place, neutron capture only requires that a seed nucleus absorb a neutron:

$$^{A}_{Z}\mathrm{X} + n \Rightarrow ^{A+1}_{Z}\mathrm{X} + \gamma \tag{2.1}$$

If the resulting isotope is beta unstable then a neutron can decay via β decay to form a proton:
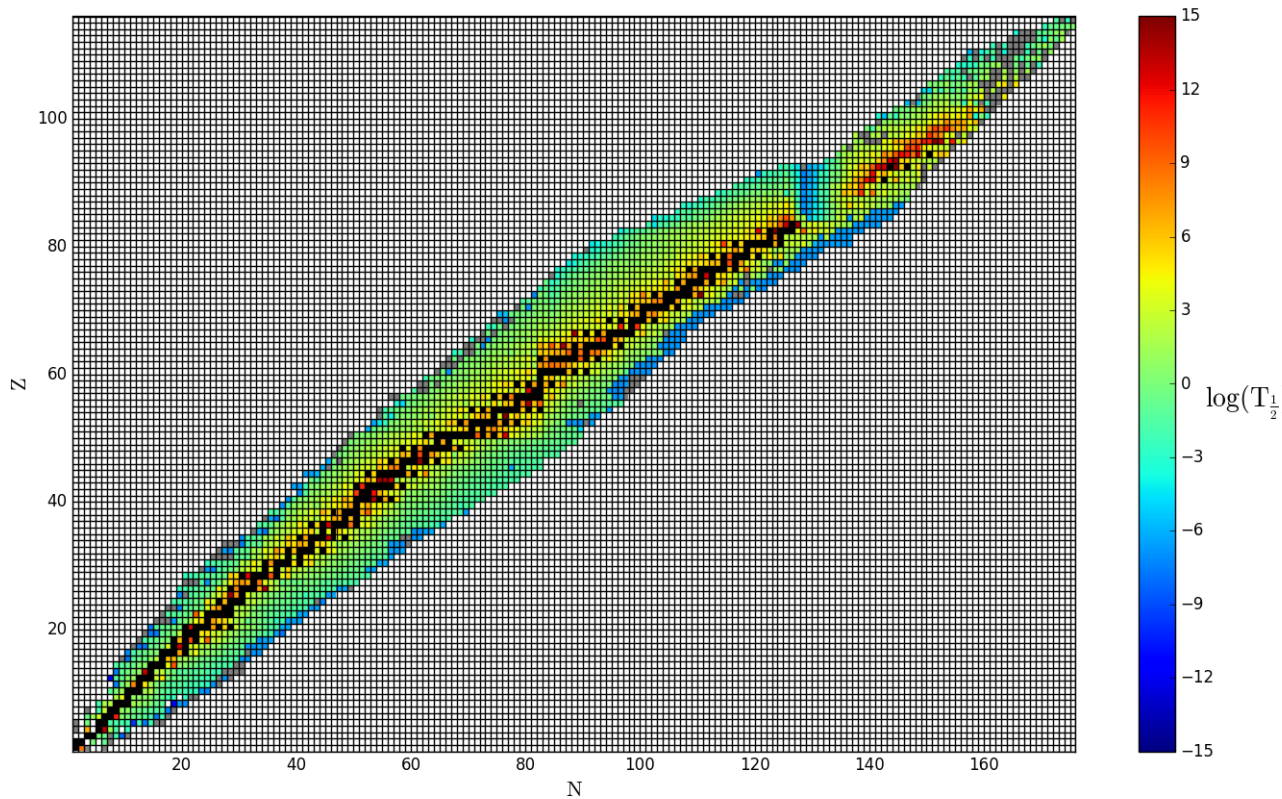
FIGURE 2.1: The chart of nuclides showing proton number against neutron number for all nuclei listed in the nuclear wallet cards from the National Nuclear Data Centre's NuDat2.7. The colour indicates half life in seconds (doesn't distinguish decay type) between 10^{-15} and 10^{15}, with black indicating a greater half life (i.e. stable or effectively stable except on the longest timescales), white indicating a lower lifetime and grey indicating unavailable data.

$$^{A+1}_{Z}X \Rightarrow ^{A}_{Z+1}Y + e^{-} + \overline{\nu} \tag{2.2}$$

These two processes allow a seed nucleus to increase its proton number by absorbing neutrons which subsequently decay to protons, increasing the atomic number and moving through the periodic table. Figure 2.1 shows the chart of nuclides, a plot of proton number (Z) against neutron number (N), colour-coded according to the half life of the nuclei with given Z and N (colouring indicates half lives between 10^{-15} and 10^{15} seconds, black indicates a half life above this range, white indicates a half life below this range and grey indicates an unknown half life). In this diagram a nucleus absorbing a neutron will step to the right by one and a nucleus undergoing β decay will move diagonally up and left by one. The s-process, characterised by a neutron capture timescale much longer than that of β decay will operate close to the valley of stability; a seed nucleus will absorb a neutron but will almost invariably undergo β decay prior to absorbing another and therefore never moves far right from stability. The r-process requires a much higher neutron flux, such that the timescale is significantly greater than the timescale for β decay; a nucleus can absorb many neutrons and move far right from stability before decaying
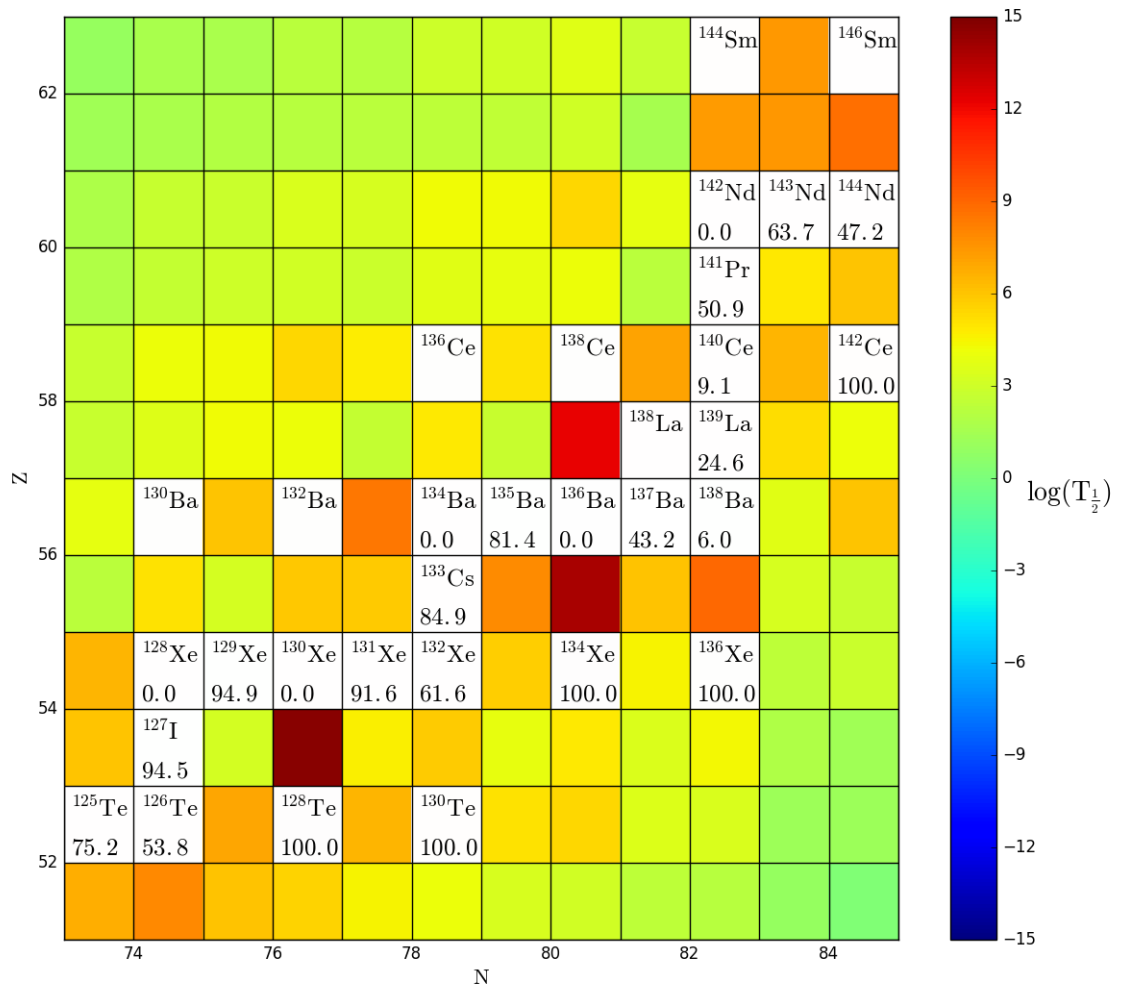
FIGURE 2.2: A zoomed in section of Figure 2.1. Stable isotopes are shown in white with the element and nucleon number shown. Below this is shown the abundance fraction not accounted for by the s-process according to Sneden et al. (2008).

multiple times back to stability. In this way the two processes form different elements. The r-process will form elements along the neutron rich edge of stability. When the nucleus reaches a stable isotope that does not undergo β decay that isotope can shield the nucleus configurations diagonally up and left from being formed by decay from the neutron rich r-process path. These elements are typically formed via the s-process instead. This can be seen easily in Figure 2.2. It shows a zoomed in section of Figure 2.1 for $52 < Z < 62$. Stable elements (half life $> 10^{15}$ s) are listed with their nucleon number and r-process fraction displayed. The fraction number in each box is derived from the works in Sneden et al. (2008) and the r-process contribution is assumed to be all material not accounted for by the s-process. Note that the proton rich isotopes ^{130}Ba, ^{132}Ba, ^{136}Ce, ^{138}Ce, ^{144}Sm and ^{146}Sm are formed via the p-process so have no r-process fraction displayed. The shielding effect can be seen in the elements ^{134}Ba and ^{136}Ba which are shielded from the r-process by ^{134}Xe and ^{136}Xe respectively. ^{128}Xe, ^{130}Xe and ^{142}Nd are similarly shielded. In this way some nuclides are r-process only as they are separated

from the s-process path by unstable nuclides that will decay before enough neutron can be absorbed and some nuclides are s-process only as they are shielded from the r-process path by stable isotopes. Other nuclides are both s-process and r-process, although often dominated by one process. Individual effects can have strong impacts on the s/r process split for particular nuclides, the neutron magic numbers for example define the s-process peaks discussed in the next section.

2.3   s-process

The s-process is substantially better understood than the r-process. A primary reason for this is the wealth of experimental data available for the formation of s-process nuclides (see Käppeler et al. 2011 for a review of experimental s-process) that allows for determination of the s-process path using the experimental neutron capture cross sections. Comparisons have led to the idea that the s-process is formed from two primary parts: a main process forming s-process nuclides in the range $A \gtrsim 90$, and a weak process forming nuclides in the range $A \lesssim 90$.

The description for the s-process where β decay timescales are much longer than neutron capture timescales yields a fixed s-process path, with only one direction the evolving seed nuclei can travel. In reality, there can be several branching paths that arise due to increased neutron density or decay rates giving conditions where the timescales are more similar (see below for ^{86}Rb branching for the ^{22}Ne neutron source as an example).

Additionally, nuclide build ups can occur for magic numbers. The magic numbers are a set of nuclides with a specified number of nucleons that lend themselves to stability. This is the result of the nucleons being arranged into complete shells and results in stronger binding energy per nucleon than would otherwise be expected. This is of particular interest to the s-process; the neutron magic numbers 50, 82 and 126 result in a build up of nuclides that are more resistant to neutron capture (i.e. they have smaller neutron capture cross sections). This build up can be seen in Figure 2.2 for N = 82, which shows the second s-process peak (Ba, La, Ce, Pr, Nd). It also results in Ba being a largely s-process element despite formation being possible by both the s-process and r-process as the neutron magic ^{138}Ba builds up. The neutron magic numbers 50 and 126 correspond to the first (Sr, Y, Zr) and third (Pb) s-process peaks respectively.

Observations of s-process element enhanced stars have helped to narrow down the s-process sites, beginning with the observation of the radionuclide ^{99}Tc, an s-process nuclide with a half life of 2.1×10^5 years (Merrill, 1952). The observation of short lived isotopes suggests that the s-process must operate within the stars where the isotopes are observed rather than occur a result of enrichment by previous generations of stars. Observations have largely found s-process

production occurs in low-mass Asymptotic Giant Branch (AGB) stars (Smith and Lambert 1986, Sterling and Dinerstein 2008, van Aarle et al. 2013).

The site for the main s-process is during the thermal pulse phase of AGB stars. In order to understand how these pulses occur and facilitate the s-process, it is important to briefly cover the evolution of these stars prior to the AGB phase. The progenitors of AGB stars lie within the mass range $\sim$ 1 - 8 $M_\odot$ (stars below this range are not massive enough for any significant burning beyond H burning and stars above this range will end their lives as core collapse supernovae). These stars spend the majority of their lives on the main sequence fusing H into He to generate radiation pressure sufficient to balance gravity. As the H in the core becomes depleted the now largely He core contracts, leaving behind a nuclear burning H layer. The contracting core causes the outer layers of the envelope to expand and cool and the star begins to move onto the red giant branch of the Hertzsprung-Russell diagram. The cooling of the outer layers increases convection, which eventually extends deep enough to begin mixing between the convective layers and the region about the H burning zone. This results in what is known as the first dredge up where the products of nuclear burning are able to move into the envelope. These dredge up events are particularly important, as the outer layers of the envelope are diffuse and can easily be lost to stellar winds. Eventually temperatures in the core of the star become sufficient for He burning. When the He core becomes depleted, it once again contracts forming a C-O core and leaving behind a He burning layer. This core is highly electron degenerate and as a result of the increased density energy loss via neutrinos is significant. In stars with initial mass roughly $> 4 M_\odot$ a second dredge up occurs as the He core contracts and the convective zone penetrates deeper into the H burning layer. Regardless of the second dredge up event, the star now begins to travel up the AGB branch. From inside out, the AGB star now consists of: a degenerate C-O core, a He burning shell, a H burning shell and the convective envelope. In between the H burning shell and He burning shell is a H deficient zone composed largely of He from the previous H burning and polluted with C, O and Ne from previous dredge ups. This sets the stage for the thermal pulses. He builds up in the H deficient zone between the two shells until the bottom of the zone ignites. This results in a runaway thermonuclear event as the He burning progresses faster than the zone can expand, increasing the temperature of the zone and releasing massive amounts of energy. It also allows for the formation of a convective zone between the H and He burning shells which effectively mixes the H deficient region. The increase in temperature also increases the opacity which lowers the bottom of the outer convective envelope to below the H burning shell. This then allows mixing of the H deficient region and the envelope, bringing products of AGB nucleosynthesis (e.g. C, N and s-process elements) towards the surface of the star. This mixing of the outer envelope and H deficient zone is known as a third dredge up. Eventually the H deficient zone expands enough that the temperature decrease limits He burning to the He burning shell. The process of He build up may begin again and the thermal pulse (and third

dredge up event) can repeat. In this way the envelope may become more polluted over time with nucleosynthesis products from the internal zones of the star.

In particular, the He burning produces large amounts of ^{12}C via the triple alpha process:

$$\alpha + \alpha + \alpha \Rightarrow {}^{12}\text{C} \tag{2.3}$$

which can lead to the production of C stars (C/O > 1) over multiple third dredge up events. In higher mass AGB stars ($\gtrsim 4M_\odot$) this C is largely converted to N by the process of hot bottom burning (HBB), where the bottom of the convective envelope overlaps the top of the H burning region. This provides additional fuel to the H burning region, increasing the luminosity of high mass AGB stars in addition to allowing proton capture on dredged up C to form N. The C enriched stars are often found to contain s-process elements (including the isotope ^{99}Tc, above, suggesting Tc production in AGB stars that do not undergo HBB). In order for the s-process to operate a source of free neutrons is required. AGB stars have two processes that can produce neutrons. The first is the chain of alpha captures and positron emission converting ^{14}N into ^{25}Mg:

$$^{14}\text{N} + \alpha \Rightarrow {}^{18}\text{F} + \gamma \tag{2.4}$$

$$^{18}\text{F} \Rightarrow {}^{18}\text{O} + \beta^+ + \nu \tag{2.5}$$

$$^{18}\text{O} + \alpha \Rightarrow {}^{22}\text{Ne} + \gamma \tag{2.6}$$

$$^{22}\text{Ne} + \alpha \Rightarrow {}^{25}\text{Mg} + n \tag{2.7}$$

This reaction was first noted in Cameron (1960). It has the advantage of the H deficient zone being rich in ^{14}N (via the CNO cycle) and He so it can produce a significant quantity of neutrons during the thermal pulses and the s-process material can be transferred to the envelope during the third dredge up events. It has a high ignition temperature (T $\gtrsim 3 \times 10^8$K), so should only operate in AGB stars with mass $\gtrsim 3M_\odot$ (though these temperatures can be reached in the later thermal pulses of lower mass AGB stars as noted in Karakas 2010). A second process is capable of producing free neutrons at lower temperatures (T $\gtrsim 3 = 9 \times 10^7$K) by conversion of ^{13}C into ^{16}O:

$$^{13}\text{C} + \alpha \Rightarrow {}^{16}\text{O} + n \tag{2.8}$$

The formation of ^{13}C requires proton capture on ^{12}C, i.e.:

$$^{12}\text{C} + p \Rightarrow {}^{13}\text{N} + \gamma \tag{2.9}$$

$$^{13}\text{N} \Rightarrow {}^{13}\text{C} + \beta^+ + \nu \tag{2.10}$$

The protons required for this process are pulled down from the envelope into the H deficient region during the third dredge up events where the envelope can overlap the H shell and the ^{12}C enriched H deficient region below. This leads to the formation of the so called "^{13}C pocket" beneath the base of the H shell during the thermal pulses (Iben and Renzini 1982b,a). However, 1D calculations have been unable to self-consistently reproduce the downflow of protons required to form the "^{13}C pocket"; this naturally is one of the biggest uncertainties in the AGB s-process. Instead these calculations have to "artificially" insert the protons. One of the methods commonly used is to insert and partially mix the protons into the H deficient region during third dredge up events (e.g. Lugaro et al. 2004, Karakas 2010).

The ^{22}Ne and ^{13}C neutron sources have different s-process yields for several reasons. Firstly, the ^{22}Ne s-process channel operates in the H deficient zone between the He and H burning shells during thermal pulses, whereas the ^{13}C s-process channel operates in the quiet He burning phase in between the pulses. Operating during the pulse the ^{22}Ne channel reaches much higher neutron densities which can activate different branches of the s-process. One such example is the stable isotope ^{87}Rb (neutron magic) which can form by neutron capture from the unstable isotope ^{86}Rb if neutron capture occurs prior to β decay into ^{86}Sr (Beer and Macklin, 1989; Karakas et al., 2012). Additionally the interpulse timescale is substantially longer than the thermal pulse timescale and as a result the ^{13}C channel is able to form heavier s-process elements (Gallino et al., 1998). This is consistent with the observations discussed above that suggest a main s-process operating in the thermal pulses of low mass AGB stars.

2.4   r-process

The r-process is somewhat more difficult to model than the s-process for several reasons. The conditions required for the r-process to operate ($\sim 10^{24}$ neutrons cm^{-1}, though this depends on temperature) are more extreme and also appear to be both rare and short-lived processes. Additionally, unlike the s-process, there is no direct observational evidence of the r-process
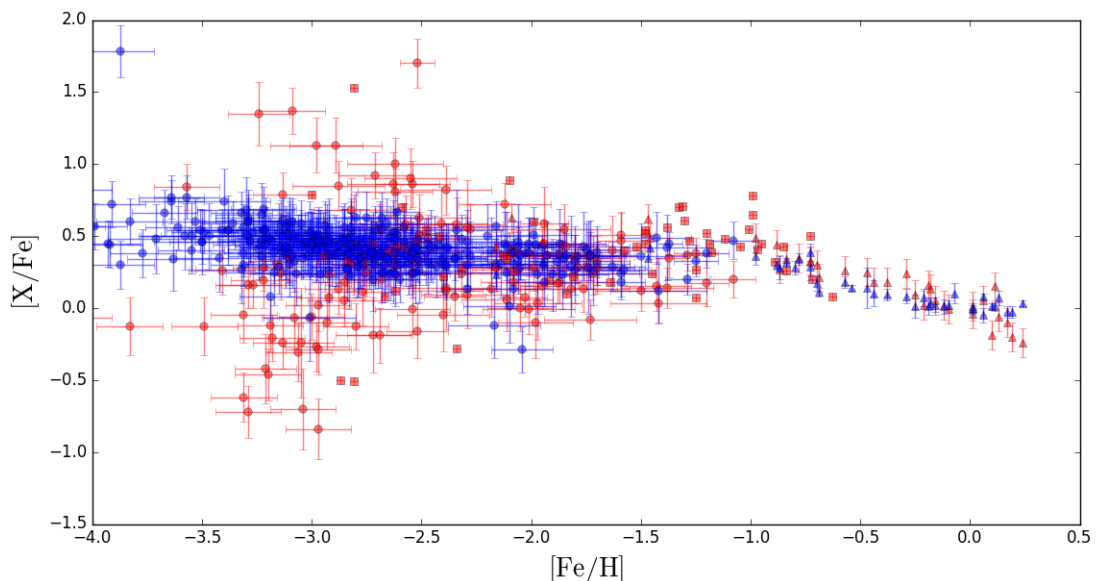
FIGURE 2.3: [Mg/Fe] (blue points) and [Eu/Fe] (red points) against [Fe/H] for low metallicity stars. Data drawn from Hansen et al. (2016, squares), Roederer et al. (2014, circles), Zhao et al. (2016, triangles).

operating. The information we do have must be inferred from observations of elements that are almost exclusively r-process, such as Eu, and theoretical simulations. One such piece of evidence is shown in Figure 2.3 which shows observational data for low metallicity stars taken from Hansen et al. (2016, squares), Roederer et al. (2014, circles), Zhao et al. (2016, triangles). The red points show the [Eu/Fe] – [Fe/H] relation and the blue points show the [Mg/Fe] – [Fe/H] relation. Mg is an α element, primarily produced in massive stars leading to the flat trend observed up until [Fe/H] $\sim$ −1, where Type Ia supernovae (SNe) increase Fe production driving down [α/Fe] ratios. Conversely the [Eu/Fe] trend shows large scatter at low [Fe/H]. This indicates that the r-process must operate in the early universe, while [Fe/H] is still low, and that the events must be both reasonably rare but each individual event must produce large quantities of Eu to reach [Eu/Fe] $\sim$ 1 at low [Fe/H].

Historically the study of r-process enriched stars began with the discovery of r-process enhanced red giants (Sneden and Parthasarathy, 1983; Gilroy et al., 1988). Metal poor stars enriched by r-process elements are of particular interest as they are less far removed from the r-process nucleosynthesis process. Modern observations have found both r-process patterns in good agreement, relative to other r-process elements, with observed solar values (Sneden et al., 1994; Roederer, 2017; Hansen et al., 2018) and r-process patterns with heavier elements missing (Honda et al. 2006 showed a decreasing trend from Sr to Yb, Roederer et al. 2010 found high scatter in [La/Eu] ratios amongst high [Eu/Fe] stars). This suggests that either multiple r-process sites exist (in the same manner as there exists a weak s-process, a weak r-process has been suggested, in addition to an intermediate process discussed later) or that the r-process yields have some dependence

on the surrounding conditions. Observations of Reticulum II, a ultra-faint dwarf galaxy near the Milky Way, found the stars to be very metal poor ([Fe/H] < -2) but containing stars strongly enriched by r-process elements (Ji et al., 2016). Other abundances were similar to stars in other ultra-faint dwarf galaxies, suggesting enrichment by a single r-process event.

Before considering potential r-process sites it is important to highlight the requirements for the r-process to operate. Generally the behaviour of the elemental abundances in an astrophysical plasma can be described by a nuclear reaction network, which describes the nuclear abundances of each nuclide in terms of the reaction cross sections of all possible reactions across temperatures and densities. Naturally this lends itself well to computation. In addition to Equation 2.1, which describes the neutron capture on a nucleus, the inverse equation,

$$\underset{Z}{\overset{A+1}{}}\mathrm{X} + \gamma \Rightarrow \underset{Z}{\overset{A}{}}\mathrm{X} + n, \tag{2.11}$$

is also important, describing the loss of a neutron via photodisintegration. If these two processes rates are high enough then chemical equilibrium may be achieved where the rate of neutron capture is equal to the rate of neutron loss. If this occurs across the whole table of nuclides then nuclear statistical equilibrium (NSE) occurs and the quantities of each nuclide can be fixed. In practice this is not often the case; low reaction rates mean that chemical equilibrium does not occur. In these cases a quasi-equilibrium (QSE) occurs, where only sections of the chart of nuclides are in equilibrium. One such example is the freezing out of charged particle reactions which occurs when the density is too low for sufficient quantities of ^{8}Be to be maintained. ^{8}Be is the intermediate step in the triple alpha process, with a short half-life (6.7×10^{-17} s):

$$^8\mathrm{Be} + \alpha \Rightarrow {}^{12}\mathrm{C} \tag{2.12}$$

Under low densities the inverse of the above (the decay of ^{8}Be) reaction dominates. The result of this freezing out is a lower abundance of nuclei heavier compared to α particles than would otherwise be expected and the corresponding excess of α particles. Additionally it results in the decreased number of heavier nuclei being shifted to even heavier nuclei via α captures. As a consequence the primary interactions a nucleus can undergo in this QSE state are neutron capture, photodisintegration and β decay. With high enough neutron density the neutron capture cross section is high enough that the timescale for neutron capture is significantly shorter than β decay and a large number of neutrons can be captured in a short space of time. As a nucleus becomes more neutron rich the energy required to remove a neutron decreases as the nucleus reaches the neutron drip line (so called because no energy is required to remove a neutron and added neutrons "drip" out). At sufficiently high temperatures neutron captures may be in equilibrium with photodisintegrations; this is the hot r-process. Alternatively a cold r-process

may occur when temperatures are sufficiently low that photodisintegration does not occur at all (Wanajo, 2007).

Following this period of rapid neutron captures the neutron rich isotopes enter a period of β decay back to stability. This begins when the neutron to seed nuclei ratio drops to the point where nuclei can become starved of neutrons, and the timescales for neutron capture become long enough that β decay begins to dominate. Fission may also occur for large enough nuclei - producing both heavy nuclei and neutrons. These additional neutron sources can fuel additional neutron capture during the β decay period and can have an impact on the final abundance pattern.

The following sections will discuss potential astrophysical sites where the conditions required could be found.

2.4.1   Neutron Star Mergers

Somewhat unsurprisingly neutron star (NS) mergers have long been a candidate for the r-process site, since the confirmation that binary neutron star systems lose energy over time and will eventually merge. The merger event is required to remove material from the gravitational fields of the neutron stars so that it can enrich the surrounding ISM, with the r-process occurring in the dynamic ejecta of the NS merger event (originally predicted in Lattimer and Schramm 1974). As the two neutron stars spiral in to merge, neutron-rich material is ejected from both the contact point via shock heating, and in the equatorial plane via tidal forces. Both types of ejecta have low Y_e (the electron fraction of the material, with a lower value corresponding to more neutrons) though this could be affected by neutrino transport from the merger (in particular neutrino heating may increase the value of Y_e, see i.e. Wanajo et al. 2014). The role that neutrino heating plays depends on the fate of the central hyper-massive NS (HMNS) formed after the merger, though it is largely accepted that such an object will collapse into a black hole, the lifetime is still in question and may increase Y_e if the lifetime is longer than the ejecta timescales (Metzger and Fernández, 2014).

Many works have attempted to determine the nucleosynthesis paths and yields of both double neutron star (NS - NS) and neutron star - black hole (NS - BH) mergers. Simulations started to include relativistic effects with Ruffert et al. (1996) and more recent works have been fully relativistic (Shibata and Uryū, 2000) and included the effects of neutrino transport (e.g. Wanajo et al. 2014). This has allowed for predictions to be made for the nucleosynthetic yields from both NS - NS mergers and NS - BH mergers. These yields can be compared to the solar abundance r-process pattern with results suggesting that NS mergers could reproduce the solar r-process pattern (Korobkin et al., 2012), however large uncertainties still exist in how to properly treat the effects of neutrino transport. Another large uncertainty exists in the rate of NS merger events, which is a necessary component in attempting to model the evolution of r-process enrichment.

This rate can be modelled in a number of ways, ranging from an empirical rate and delay time to binary population synthesis (BPS) calculations which predict a distribution of merging delay times. Further to this these rates and delay times can be included in simulations which themselves range in complexity from simple GCE models (e.g. Argast et al. 2004, Cescutti et al. 2015, Wehmeyer et al. 2015, Côté et al. 2018) to full hydrodynamical simulations (e.g. van de Voort et al. 2015).

Although it should be noted that these introduce more uncertainties from the NS merger rate models, most works have drawn broadly similar conclusions; NS mergers likely contribute significantly to the galactic r-process however due to the timescales required for both the formation of binary systems and the subsequent energy loss leading to the merger they are a poor match for the high scatter r-process pattern at low [Fe/H]. In Chapter 4 I present my work using chemodynamical simulations which draws similar conclusions and presents evidence for a combined model of NS mergers and magneto-rotational supernovae (discussed later in this chapter, see also Chapter 5).

The gravitational wave detection GW170817 (Abbott et al., 2017b) provided further support for NS merger contributions to the r-process. It was accompanied by astronomical transient AT2017gfo (Valenti et al., 2017). Simulations of the light curves in Tanaka et al. (2017) suggest that this kilonova is best matched by an ejecta comprised of more than one component (including a least one component with medium to high Y_e) likely resulting from shock heated ejecta and tidal ejecta, with the near-infrared component explained by the decay of reasonably lanthanide rich ejecta.

2.4.2 Neutrino Driven Winds

Some CCSNe produce a neutron star from the core of the star, providing a potentially neutron rich site for the r-process. In particular the neutron star was expected to undergo a short period of intense neutrino emission driving an outflow of neutron rich matter (a neutrino driven wind) into the infalling outer layers of the star. Simulations and models were used to try to predict the r-process yields from these winds, however the initial Y_e and properties of the ejected material were found to be inconsistent. Although it was found that a good match with solar abundances could be obtained (e.g. Freiburghaus et al. 1999a), the entropies required are likely to be too high (Arcones et al., 2007). Additionally it is possible that the neutrino wind may drive up the value of Y_e hampering neutron capture. In addition to the fact that r-process sites need to be relatively rare and provide strong enrichment to explain observed abundance ratios, this suggests that it is unlikely that neutrino driven winds provide a strong r-process site, though there is potential for a weak r-process to occur.

2.4.3   Rapidly Rotating Magnetised Massive Stars

Magneto-rotational supernovae (MRSNe) are a hypothetical class of CCSNe involving highly magnetised and rapidly rotating stars. The rotation provides the neutron rich site; after the core has collapsed to form a neutron star an accretion disc will form, given fast enough rotation. This accretion disc will have high density close to the neutron star resulting in a significant increase in the rate of electron capture and the conversion of protons to neutrons, increasing the number of neutron rich nuclei and, when these nuclei reach the neutron drip line, adding free neutrons to the system (Cameron, 2001). As with neutrino winds models the neutrino flux is expected to drive up the value of Y_e in the disc, however given the short duration of the wind it is expected that the electron capture process will dominate, allowing the r-process to operate. In addition to the rotational requirement it is important that the star has a strong magnetic field. Combined with the rotation, the magnetic field lines will drive jets at the poles of the neutron star. As the field lines are embedded in the accretion disc this provides a mechanism to eject r-processed material from the accretion disc.

MRSNe have increased in popularity recently due to a number of reasons. Firstly, the difficulties mentioned above in fitting observed abundance ratios using only NS mergers suggest that multiple main r-process sites are likely. Secondly the improvement in computational capabilities has allowed 3D magneto-hydrodynamic (MHD) simulations at high resolutions. Winteler et al. (2012) was one of the first 3D MHD studies of MRSNe and was able to successfully produce r-process elements and eject them from the polar jets. Other works have also been successful in producing r-process elements, however uncertainties remain, particularly with regards to magnetic instabilities (Mösta et al. 2018 suggests that potential kink instabilities could significantly reduce r-process ejection). With this progress has come theoretical yields for MRSNe events which can be included in chemical evolution models; in particular in Chapter 4 I present simulations which support the role of MRSNe in the r-process enrichment of the Milky Way. Additionally the number of stars that have the correct conditions for MRSNe to occur is not constrained at all. Increasing metallicity reduces the rotation speed of star (due to angular momentum loss via stronger stellar winds) suggesting that the conditions are more likely to occur in the early universe (this may actually better support observations, see chapter 5).

2.4.4   Electron Capture Supernovae

Electron capture supernovae (ECSNe) are a variant of CCSNe with a neutron source provided by the unique conditions in O-Ne-Mg cores. These cores form in stars with a mass range of roughly 8 - 10 $M_\odot$ (the actual range has a metallicity dependence, see Doherty et al. 2015) and will collapse due to electron capture by ^{20}Ne and ^{24}Mg reducing the electron pressure (Miyaji et al. 1980). This collapse occurs prior to oxygen burning and the electron capture reduces Y_e

which could lead to r-processing in the ejecta. However Wanajo et al. (2011) found that ECSNe are probably only able to produce a weak r-process.

2.5   p, ν, νp and i processes

Stable nuclides positioned on the proton rich side of the valley of nuclear stability are known as p-nuclides (Arnould and Goriely, 2003). Unlike the s-process and r-process there are no elements formed primarily via the p-process; instead p-process elements represent a small fraction ($< 1\%$) of the isotopes for any given element (Anders and Grevesse, 1989). The p-process is typically driven by photodisintegration in explosive astrophysical sites but could also be synthesised due to neutron emission via neutrino excitation (the ν process, see Woosley et al., 1990). The νp process (Fröhlich et al., 2006) provides an alternative formation site for light p-nuclides via proton capture in proton rich SNe ejecta driven by neutrino winds. Given the small contribution the p-nuclides make to elemental abundances I consider them negligible for the remainder of this work.

The i-process was proposed as an intermediate process between the s-process and r-process (Cowan and Rose, 1977) that operates by mixing protons from the H-rich layer into the He-burning layer below. This activates the same ^{13}C to ^{16}O neutron production process described above for AGB stars. However, the neutron density that results is potentially much higher than that for the s-process due to larger quantities of H mixed into the He-burning shell over a shorter timescale. The contribution to overall abundances is not expected to be significant so the effect will not be included for the remainder of this work.

Chapter 3

Code and Models

3.1 Smoothed Particle Hydrodynamics

The code I use for the simulations in the following chapters is based on the code GADGET-3 which uses smoothed particle hydrodynamics (SPH, Lucy 1977, Gingold and Monaghan 1977) to calculate the gas dynamics. SPH codes model material as particles for simplicity but smooth these with a kernel that allows the particles to affect neighbour particles and behave more realistically. Each particle represents a large mass of gas, stars or dark matter. More specifically GADGET-3 is a TreeSPH code (Hernquist and Katz, 1989). This describes the two main processes that govern particle interactions: the hierarchical tree method used to calculate gravitational interactions and the SPH formulation for the fluid elements. A full description of the previous version GADGET-2 can be found in Springel (2005) and the references therein. The simulation code I use also includes

In this chapter I will briefly outline the code I used, including existing physical processes and chemical enrichment models. I will then discuss the modifications I made, the inclusion of r-process chemical enrichment and alternate supernova feedback models.

3.1.1 Gravitation

Gravitational forces are fundamental to galaxy evolution and therefore require accurate treatment within galactic simulations. Fluid elements, stars and dark matter are all treated as particles within GADGET, allowing for ease of computation by N-body physics. The particle dynamics are given by the Hamiltonian,

$$H = \sum_i \frac{p_i^2}{2m_i a^2} + \frac{1}{2} \sum_{ij} \frac{m_i m_j \phi (x_i - x_j)}{a},$$ (3.1)

17

where p_i, m_i, x_i give the momentum, mass and position vector of the ith particle, a is the cosmological scale factor (set to 1 for non-cosmological runs) and $\phi(x_i - x_j)$ gives the potential between the ith and j^{th} particles, given by the solution to

$$\nabla^2 \phi(x) = 4\pi G \left(-\frac{1}{L^3} + \sum_n \delta(x - nL) \right),$$

(3.2)

where G is the gravitational constant, L^3 is the box volume for the periodic boundary conditions and n is summed over all integers. The function δ describes the point mass smoothed by the spline kernel

$$W = \frac{8}{\pi h^3} \begin{cases} 1 - 6(\frac{r}{h})^2 + 6(\frac{r}{h})^3 & \text{for} \quad 0 \leq \frac{r}{h} \leq \frac{1}{2} \\ 2(1 - \frac{r}{h})^3 & \text{for} \quad \frac{1}{2} < \frac{r}{h} \leq 1 \\ 0 & \text{for} \quad \frac{r}{h} > 1 \end{cases}$$

(3.3)

which depends on the given smoothing length, h, and the distance, r (in this case the position vector, x). This gravitational smoothing is required to prevent large angle scattering in short range interactions ($W = 0$ for ranges where r is greater than the smoothing length).

The long range of gravitational forces necessitates a slight loss in accuracy in exchange for efficiency; as each particle will influence every other particle, calculating the full system of forces across all N particles and timesteps is computationally expensive (scaling as N^2 due to sum over i and j). To this end, long range gravitational forces are computed using the tree model.

3.1.2 Tree Method

More accurately called hierarchical multipole expansion (Hernquist and Katz, 1989), the Tree model was named due to the repeated division of space into progressively smaller nodes; in GADGET-3 each node is divided into 8 smaller nodes (i.e. a cube with sides of length L becomes 8 cubes with sides of length L/2). Nodes are progressively subdivided until nodes with only a single particle appear (called leaf nodes). When determining gravitational forces each node is examined in turn to check if the error from using node approximation is small enough, starting with the largest nodes; if it is found to be sufficiently small then no further progress for that node is needed, if greater accuracy is needed then the next set of node subdivisions is considered. This is done recursively until particles are accounted for. Typically this results in larger nodes being used for more distant particles.

3.1.3 Hydrodynamics

SPH is a method of fluid modelling that describes the interaction between fluid particles that have been smoothed out by kernel interpolation. As in Springel and Hernquist (2002), the acceleration of a particle is given by

$$\frac{\mathrm{d}v_i}{\mathrm{d}t} = -\sum_j^N m_j \left(\frac{f_i P_i}{\rho_i^2} \nabla_i W_{r_i - r_j}(h_i) + \frac{f_j P_j}{\rho_j^2} \nabla_i W_{r_i - r_j}(h_j) \right), \tag{3.4}$$

where P is the pressure, the smoothing kernel, $W_{r_i - r_j}$, is as defined in the previous section between the ith and j^{th} particles with the smoothing length, h_i, being adaptive such that the smoothing radius encloses a specified number of "neighbour" particles (and therefore the sum only need iterate over these neighbour particles). f_i is given by

$$f_i = \left(1 + \frac{h_i}{3\rho_i} \frac{\partial \rho_i}{\partial h_i} \right). \tag{3.5}$$

Densities are calculated by considering the contribution from the surrounding neighbour particles (the smoothed part of SPH),

$$\rho_i = \sum_j^N m_j W_{r_i - r_j}(h_i). \tag{3.6}$$

Additionally, the smoothing length is adaptive in that the value of h_i varies such that the sphere bounded by radius h_i contains a constant mass:

$$\frac{4\pi}{3} h_i^3 \rho_i = N_{ngb} m_{gas} \tag{3.7}$$

where N_{ngb} is the number of SPH neighbour particles and m_{gas} is the typical mass of the SPH particles. Rather than thermal energy, an entropy function is used instead:

$$A = \frac{P}{\rho^\gamma}, \tag{3.8}$$

where $\gamma = \frac{5}{3}$. A viscous force is included using

$$\frac{\mathrm{d}v_i}{\mathrm{d}t} = -\sum_j^N m_j \Pi_{ij} \nabla_i \overline{W}_{ij}, \tag{3.9}$$

where Π_{ij} is a viscosity with a value to zero if the particles being considered are not approaching each other and $\overline{W}_{ij}$ is the average of $W_{r_i-r_j}(h_i)$ and $W_{r_i-r_j}(h_j)$. The viscosity adopted is the same formulation as Springel (2005). This will generate entropy:

$$\frac{\mathrm{d}A_i}{\mathrm{d}t} = \frac{\gamma-1}{2\rho_i^{\gamma-1}} \sum_j^N m_j v_{ij} \Pi_{ij} \nabla_i \overline{W}_{ij}. \tag{3.10}$$

3.1.4 Star Formation

In the context of SPH star formation is the conversion of gas particles into star particles. Star particles do not represent single stars but rather a large mass (typically in the range $10^4 < \mathrm{M}_\odot < 10^6$). For star particles, these masses represent an association of stars which are modelled as a simple stellar population (i.e. a group of stars with identical metallicity and age but a range of masses, Kobayashi 2004). Care has to be taken so that this is performed in a realistic manner as the cycle of chemical enrichment and subsequent star formation from enriched gas is fundamental to the composition of modern stars. Here, star formation is based on the conditions set out in Katz (1992) which required a) convergent gas flow, b) rapid cooling and c) Jeans unstable gas. Provided these conditions are met the star formation timescale is given by

$$t_{\mathrm{sf}} = \frac{1}{c} t_{\mathrm{dyn}}, \tag{3.11}$$

where $t_{\mathrm{dyn}} = (4\pi G\rho)^{-0.5}$ is the dynamical timescale and $c = 0.1$ is a parameter set in accordance with Kobayashi (2005); Kobayashi et al. (2011). A random number is generated and compared to the probability that star formation will occur:

$$P = 1 - e^{\frac{\Delta t}{t_{\mathrm{sf}}}}, \tag{3.12}$$

where Δt is the timestep. If this is satisfied, half the initial mass of the gas particle will be converted into a star particle, a simple stellar population (i.e. a group of stars with the same metallicity and birth time but a distribution of masses). The masses are distributed according to the Kroupa initial mass function (IMF), Kroupa (2001).

3.2 Chemical Enrichment

At the end of their lives stars redistribute some of their elements into the surrounding gas in stellar winds and SNe events. The chemical enrichment scheme used is based on Kobayashi
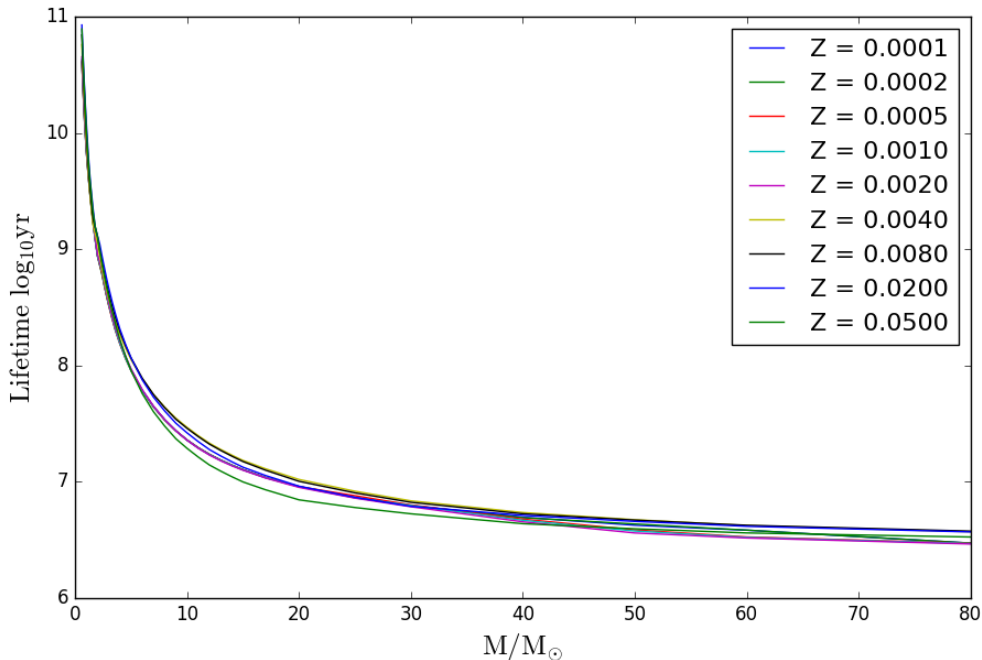
FIGURE 3.1: Metallicity dependent main sequence lifetime for stars. The duration of a timestep is used to determine the mass limits containing the stars within a star particle ending their lives during that timestep.

(2004) with a number of changes which are noted below. The metallicity dependent main sequence lifetime is taken from Kodama and Arimoto (1997) and shown in Figure 3.1. For a given timestep these lifetimes can be applied in reverse to determine the mass limits that contain the stars that are going to die during a given timestep (under the approximation that stars end their lives a short time after leaving the main sequence). Using the IMF these mass limits give the total mass and distribution of stars ending their lives during the timestep.

Before the nucleosynthesis yields for the star particles are calculated, the ratio that each nearby particle will receive is determined. The star particle finds the nearest N_{ngb} neighbour particles and uses this to determine the feedback radius that contains these particles. N_{ngb} is typically chosen as 64 ± 2 for Milky Way simulations and 36 ± 2 for isolated dwarf disc galaxies as values too high or too low give inefficient feedback (see Kobayashi et al. 2007a) and N_{ngb} for chemical enrichment is chosen to match that used for SN feedback (see below). This radius becomes the smoothing distance in the kernel (equation 3.3) which is used to weight the distributed quantities (with closer particles receiving a greater proportion of the ejected material).

Once this is done yields are calculated and distributed according to the kernel weighting. Although the different processes use different models, all use the concept of yield tables. These are essentially three-dimensional tables that give the mass yield for a star with a given mass and metallicity for each element. Naturally, the star mass and metallicites won't line up exactly with the values used in the yield tables so linear interpolation is used:

$$\frac{y - y_a}{y_b - y_a} = \frac{x - x_a}{x_b - x_a}, \tag{3.13}$$

where the quantities x and y represent the two related values (i.e. yield and stellar metallcity or yield and stellar mass) which lie between the tabulated values x_a and x_b and y_a and y_b respectively. The mass yields are interpolated for both mass and metallicity for each element tracked and the masses are then distributed to the ISM using the kernel weighting described above. This process repeats every timestep, integrating along the mass range for each star particle from high mass (shortest lifetimes) to low mass (longest lifetimes).

3.2.1 Type Ia Supernovae

For Type Ia SNe the single degenerate scenario for progenitor systems is adopted where a white dwarf (WD) in a binary star system accretes matter from the companion star, eventually taking it over the Chandrasekhar mass and triggering a Type Ia SNe event. This is in opposition to the double degenerate scenario, where two WDs merge. Type Ia play a fundamental role in the chemical evolution of galaxies as they produce large amounts of Fe resulting in the characteristic "knee" in [α/Fe] relations. The yields used for the single degenerate scenario for Type Ia SNe are taken from Kobayashi and Nomoto (2009). Figure 3.2 shows the C, O, Mg, Fe and Eu fractions of the total ejecta, normalised by solar fraction, as a function of progenitor mass for metallicities $Z = 0.05, 0.02, 0.008, 0.004, 0.001,$ and 0.0. The lifetime of the binary system is calculated based on the lifetime of the companion star giving a delay time distribution (DTD) before the yields are introduced into the ISM. These also take into account several important effects. Firstly, the effect of metallicity dependent WD winds in removing material from the WD is included. Strong winds can lead to both longer and shorter lifetimes for the binary system (depending on the mass of the companion star; higher mass stars result in shorter lifetimes, lower mass stars result in longer lifetimes). Additionally they take into account the models of both red giant and main sequence companion stars where each efficiency is determined to match observations (e.g. [O/Fe] – [Fe/H] relation).

3.2.2 Core Collapse Supernovae

CCSNe cover SNe events that are driven by gravitational collapse: Type II SNe Ib and Ic and hypernovae (HNe, broad-line Ic). Type II SNe are the end result of stars in the mass range $8M_\odot < M < 40M_\odot$. Figure 3.3 shows the C, O, Mg, Fe and Eu fractions of the total ejecta for the same metallicities as in Figure 3.2. At the point of chemical enrichment the yields are calculated by interpolating using the masses in the mass range and the metallicity of the star particle. These yields show the standard single star nucleosynthesis yields, comprised of Type
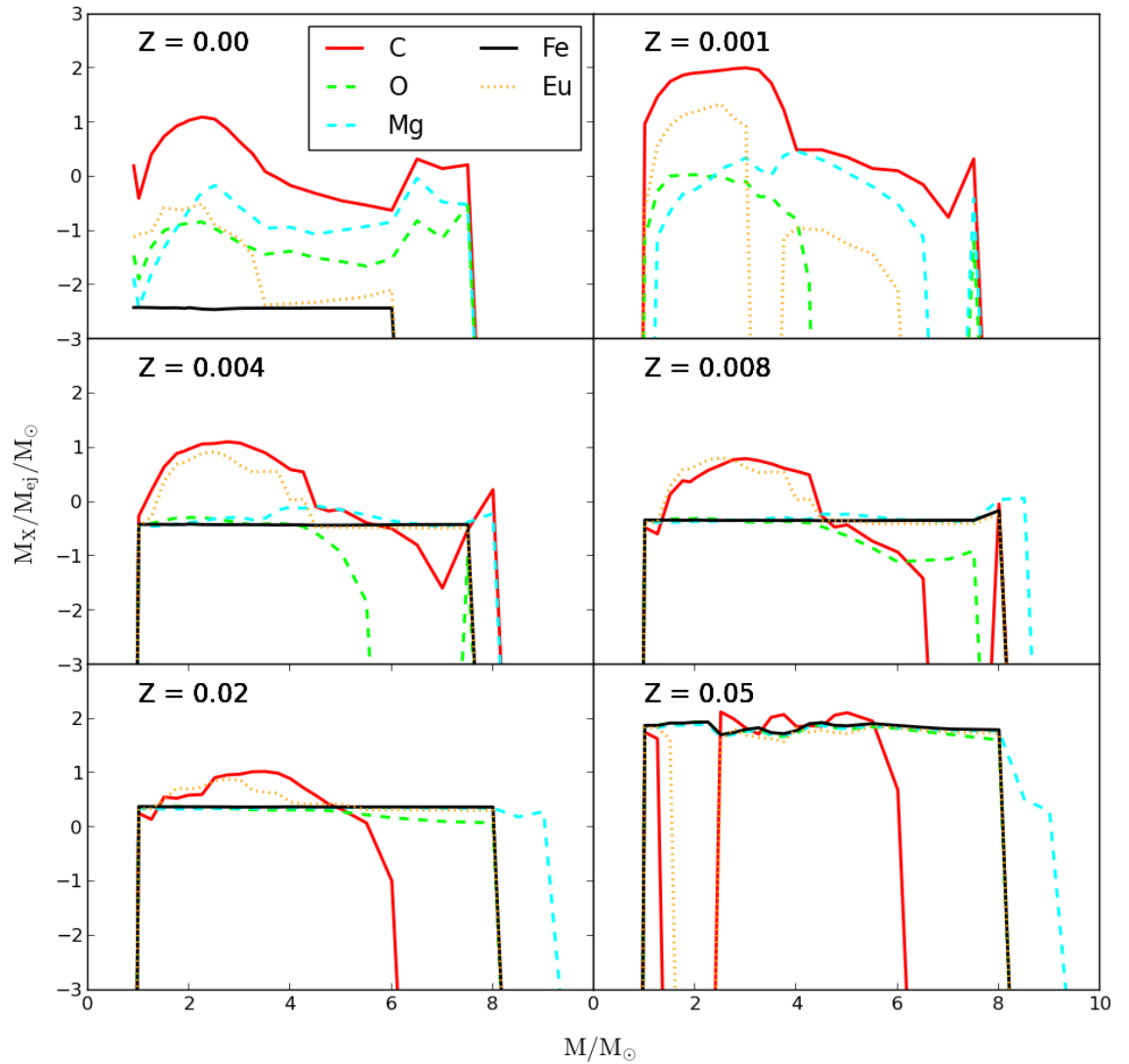
FIGURE 3.2: Ejected mass of element, X, as a fraction of total ejecta mass normalised by solar fraction from Type Ia SNe and AGB stars as a function of progenitor mass for six different metallicity stars.

II SNe (those in the mass range above roughly $10M_\odot$) and AGB stars (those in the lower mass range, see below). HNe are observed CCSNe with an explosion energy increased by a factor of 10. Yields for nucleosynthesis occurring in both of these events are taken from Kobayashi et al. (2011) and given as a function of both stellar mass and metallicity for a range of values.

The fraction of CCSNe that are actually HNe is expected to be metallicity dependent and is defined as $f_{HNe} = 0.01, 0.01, 0.23, 0.4, 0.5,$ and 0.5 for metallicities $Z = 0.05, 0.02, 0.008, 0.004, 0.001,$ and 0.0 (Kobayashi and Nakasato, 2011). At the point of chemical enrichment, yields are calculated by interpolating between the yields models for given mass and metallicity (and HNe fraction) which are then distributed according to the kernel weighting described above.
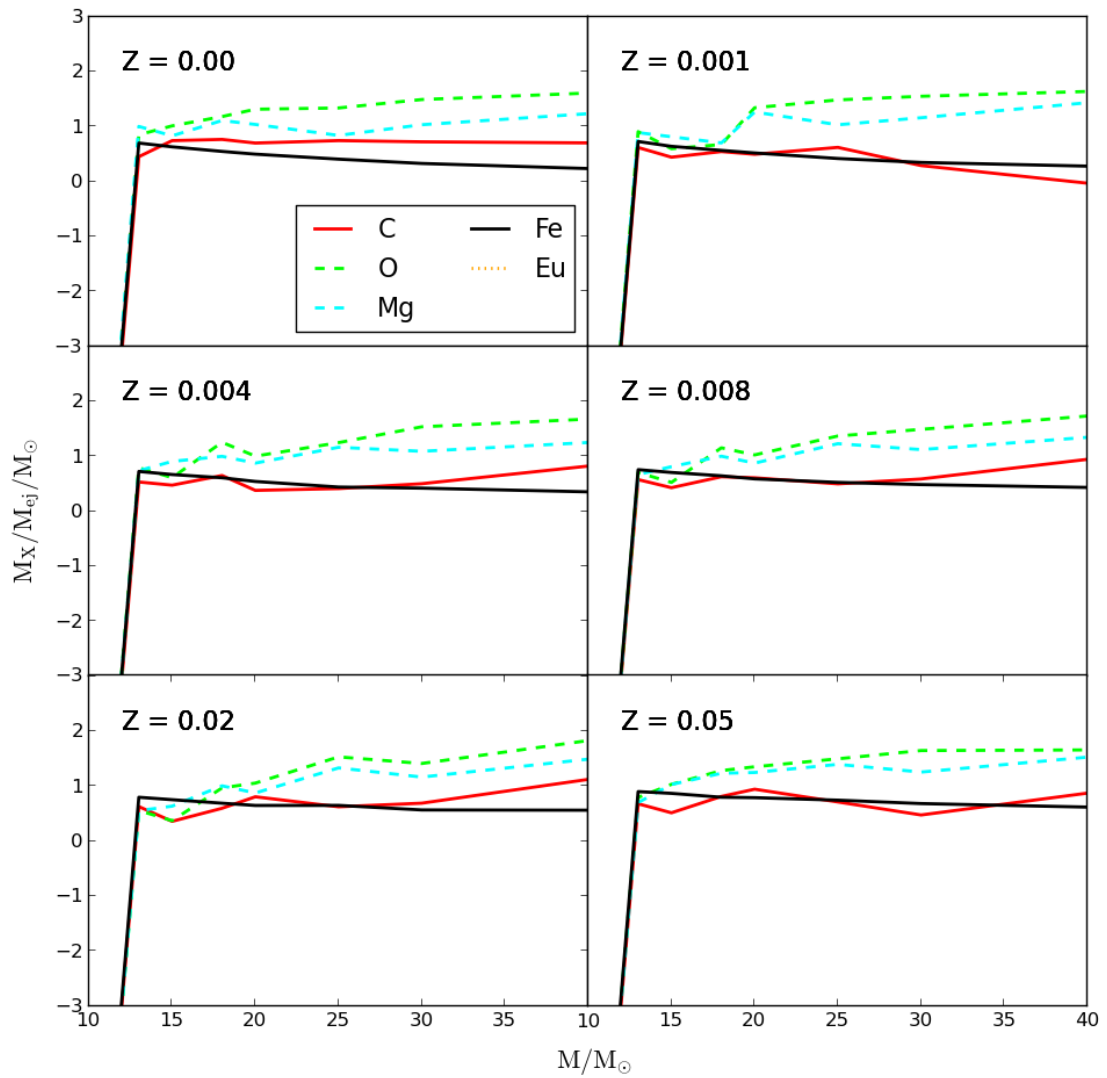
3.2.3 Stellar Winds

The envelopes of stars contain unprocessed metals from the gas the stars were formed from. These are stored and then released at the end of the stars' life.

3.3 Neutron Capture Models

In this section I describe the addition of the various neutron capture models I added into the simulation code described above, their implementation and reasons for selection.
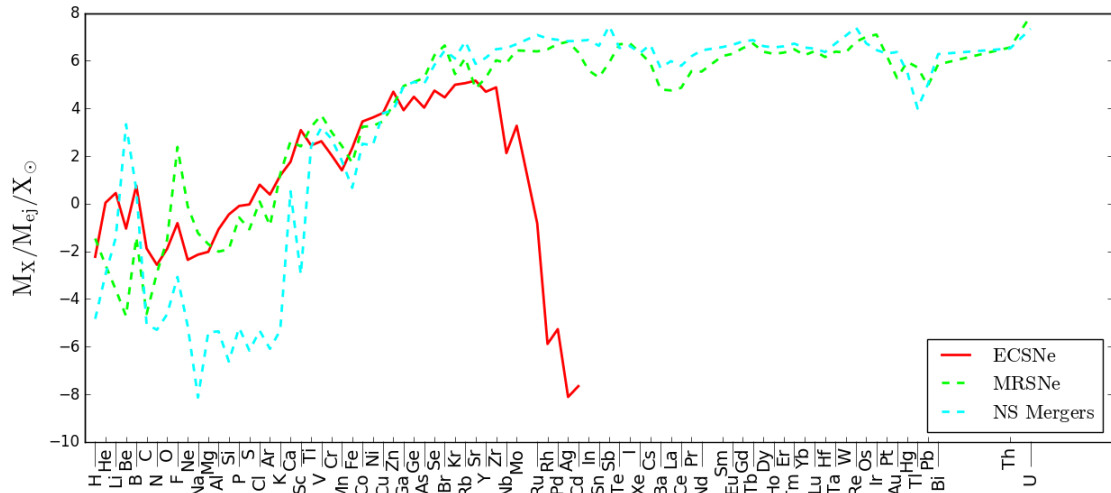
FIGURE 3.4: Mass fraction normalised by solar fraction as a function of element for NS mergers, MRSNe and ECSNe.
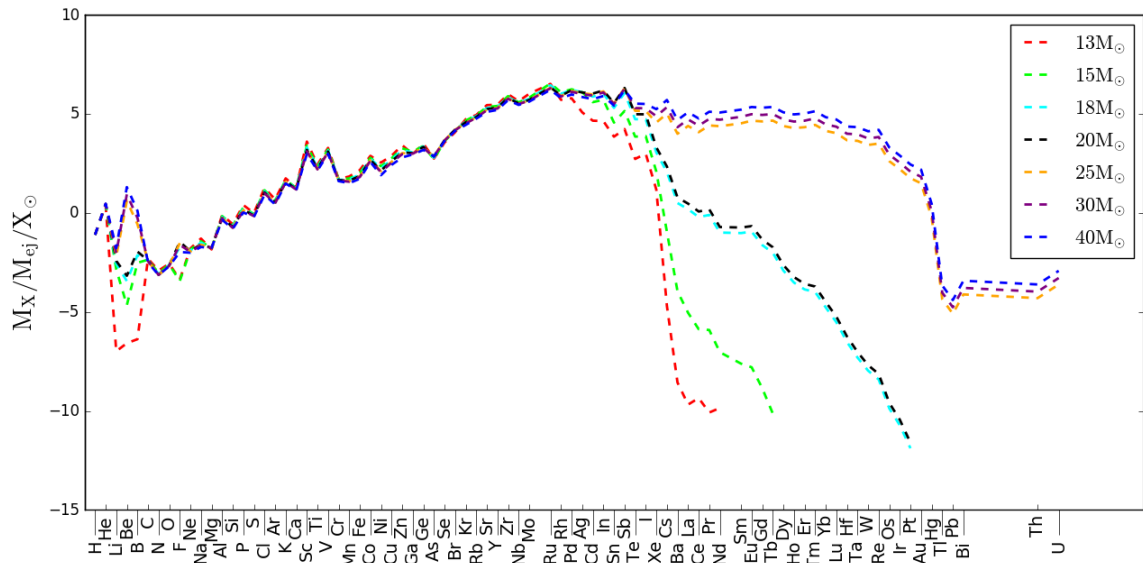
FIGURE 3.5: Mass fraction normalised by solar fraction as a function of element for the neutrino driven winds from stars with progenitor mass $M = 13, 15, 18, 20, 25, 30, 40 M_\odot$.

3.3.1 AGB Stars

I include yields for AGB stars based on the stellar nucleosynthesis calculations of Karakas and Lugaro (2016). These include s-processing as a result of thermal pulses for stars in the mass range $1 M_\odot < M < 8 M_\odot$ (though as noted in Chapter 2, these are not able to form the "^{13}C pocket" naturally and require the protons to be inserted artificially). As these yields are from a single star with progenitor mass $< 8 M_\odot$ they are simply combined with the Type II SNe yield tables (see Figures 3.2 and 3.3 for the mass fractions of C, O, Mg, Fe and Eu as a function of progenitor mass and metallicity; the contribution from AGB stars is in the mass range $M < 8 M_\odot$).
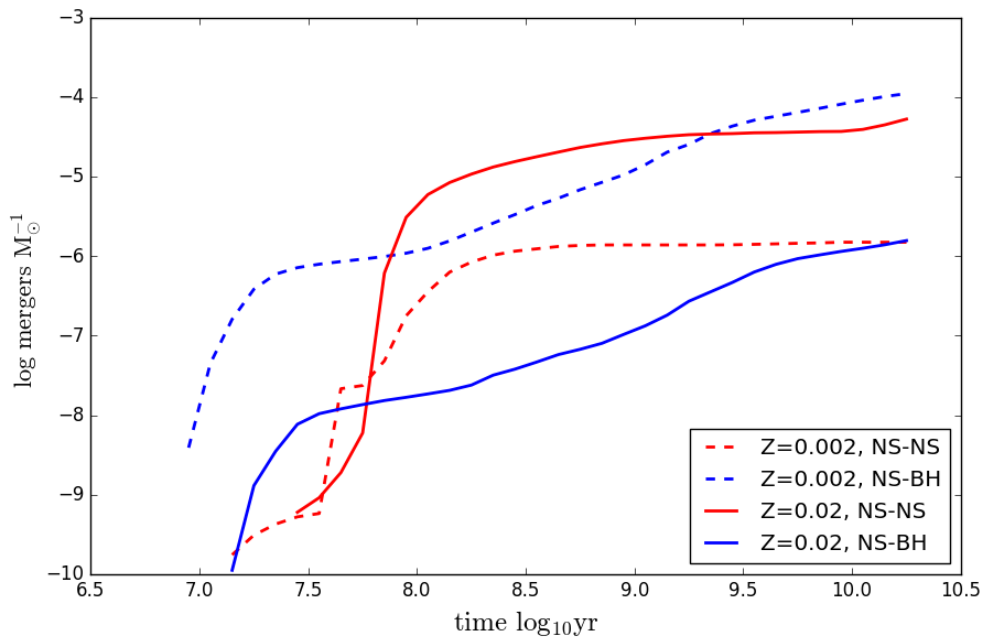
FIGURE 3.6: Delay time distribution (DTD) for NS - NS mergers (red lines) and NS - BH mergers (blue lines) for Z=0.002 (dashed lines) and Z=0.02 (solid lines). Shows the cumulative number of mergers per solar mass as a function of time.

3.3.2 Neutron Star Mergers

The NS merger yields I use are from Wanajo et al. (2014) for both NS-NS mergers and NS-BH mergers. Figure 3.4 shows mass fraction of the ejecta as a function of element for the NS mergers (in addition to MRSNe and ECSNe discussed later). The merger rate of both NS-NS and NS-BH systems is determined from the DTDs from simple stellar populations in Mennekens and Vanbeveren (2014, model 2) for both Z = 0.02 and 0.002 by interpolating between given time steps using the birth time of the star particle. Model 2 is selected as it gave the best match to observations with assumed r-process yields. A DTD is calculated by converting the merger rate as a function of time into a cumulative function. Figure 3.6 shows the cumulative DTD for both NS-NS and NS-BH mergers. For each star particle, at each timestep after stellar birthtime I integrate along these curves to determine the NS-NS and NS-BH rates. The rates of NS-NS and NS-BH events are then added together to give two rates, one for both Z = 0.02 and 0.002. These rates are then interpolated using the metallicity of the star particle (extrapolation is prevented by assuming the relevant upper or lower limit in the cases that Z is outside the range $0.002 < Z < 0.02$) to give a final rate. This rate is then combined with both the yields and a parameter, $f_{\mathrm{NSM}} = 0.5$, representing the binary fraction, to give the total mass of metals produced for a given timestep. These metals are then added to the star particle's ejected metals and distributed to the ISM as normal. Note that in this case I assume that the yields from both NS-NS and NS-BH mergers are identical. Although this is not necessarily the case, no yields for NS-BH mergers currently exist.

3.3.3 Magneto-rotational Supernovae

I use MRSNe yields from Nishimura et al. (2015, 25 $M_\odot$ star, model B11β1.00). These are shown in Figure 3.4. I use model B11β1.00 based on the rationale set out in Nishimura et al. (2015); it is a prompt magnetic jet, which is found to produce r-process elements, and provided the best match to solar r-process abundances in addtion to the r-process enhanced metal poor star CS22892-052. As MRSNe require massive, rapidly rotating stars but the expected number of stars is not observationally constrained I chose to use a free parameter, f_{MRSN}, representing the fraction of stars (with $M > 25M_\odot$) with appropriate conditions for MRSNe. This fraction of the mass of stars with $M > 25M_\odot$ within a star particle use the MRSNe yields, leaving the corresponding fraction of $1 - f_{\mathrm{MRSN}}$ of the stars using the default yields. In addition to the choice of f_{MRSN}, this results in a second choice: which yields have a fraction replaced by MRSNe. I decided to draw this fraction from the fraction of HNe stars rather than from the pool of typical Type II SNe as HNe require similar initial conditions (namely high mass and rapid rotation). Initially I chose $f_{\mathrm{MRSN}} = 0.01$ after a number of parameter tests as it gave solar [Eu/Fe] at [Fe/H] = 0 and agrees reasonably well with estimates for the MRSNe rate (see Chapter 4). Initially this rate was independent of the metallicity of the star particle. Given that increased metallicity drives angular momentum loss via solar winds and that I found [Eu/Fe] to be flat rather than showing a downward trend at [Fe/H] = 0, I also applied metallicity dependence based on the f_{HNe} dependence (see follow up paper in Chapter 5).

3.3.4 Electron Capture Supernovae

For ECSNe I adopted the yields from the 2D explosion model of Wanajo et al. (2013) for an 8.8$M_\odot$ star. The yields are used to supplement Type II SNe in a mass range which is dependent on Z (as in Doherty et al. 2015). The lower limits and upper limits are given by (8.2, 8.25, 8.8, 9.5, 9.75) $M_\odot$ and (8.4, 8.4, 9.0, 9.65 and 9.9) $M_\odot$ respectively for log Z = $-4, -3, -2.4, -2.1, -1.7$. Although the mass range is metallicity dependent, the yields I use are not, and are listed in Figure 3.4. To implement this in the code I interpolate using the metallicity for each individual star particle to calculate each particle's ECSNe mass limits. These limits are used to determine the total mass of stars undergoing ECSNe for each timestep. The mass is multiplied by the ECSNe yields to give the total amount of metals produced which are then added to the ejected metals for that timestep.

3.3.5 Neutrino-driven Winds

Although unlikely to contribute significantly to galactic r-process, I included neutrino-driven winds for completeness. I use the yields from the semi-analytical wind models of Wanajo (2013)

for $M = 13, 15, 18, 20, 25, 30, 40 \mathrm{M}_\odot$. I show the yields in Figure 3.5. The additional yields due to these winds are calculated by interpolating using the mass of the star particle and the additional nucleosynthesis products are added onto the Type II SNe yields.

3.4 Feedback Models

In addition to enriching the ISM, dying stars distribute their energy into the surrounding gas. This energy feedback is very important in the formation of galaxies, potentially heating gas and preventing star formation. As with chemical enrichment, galactic simulation codes must adopt a model to distribute this energy. Classically, this has been done by distributing the energy as thermal energy into the surrounding gas particles, either to a fixed number of particles, in a fixed radius, or using kernel smoothing. Alternatively, the energy can be input with a fraction converted to kinetic energy, roughly simulating shocked gas. The method of feedback is important when discussing chemical enrichment as gas that is enriched by SNe events will also be influenced by SNe feedback. In this section I describe the thermal and kinetic models already implemented in the simulation code and two additional models, one stochastic and one mechanical, that I include based on recent works (see Chapter 6).

3.4.1 Thermal Feedback

Thermal feedback is the "default" supernovae feedback model of the code. It shares many similarities with the chemical enrichment scheme; N_{ngb} nearest neighbour particles are selected to define a feedback radius which is passed to the smoothing kernel to weight the neighbour particles. N_{ngb} is usually chosen as 64 ± 2 for Milky Way type galaxies and 36 ± 2 for isolated dwarf disc galaxies as this gives the most efficient feedback (see Kobayashi et al. 2007a). The total energy emitted by the star particle at this timestep is then divided according to the weighting described in section 3.1 and used to heat each gas particle individually. Typically using this option I found that Milky Way simulations would develop a slightly too high SFR at late times, resulting in a small number of super-solar metallicity stars.

3.4.2 Kinetic Feedback

In addition to thermal feedback, the simulation code contains a simple option to distribute the energy partially as kinetic energy. A parameter, f_{k}, is defined as the fraction of energy to be distributed as kinetic energy (typically between 1 % and 10 %). For each SNe event the thermal energy is reduced by this amount and converted to a kinetic kick with velocity,

$$v = \sqrt{2 f_k E_{SN} W_i / M_i}, \tag{3.14}$$

where $E_{SN} W_i$ is the weighted fraction of the total SNe energy from the star particle received by the ith gas particle and M_i is the mass of the ith gas particle receiving the energy. The kick's direction is directly away from the star particle.

3.4.3 Stochastic Feedback

In an attempt to allow thermal feedback to effectively supress star formation Dalla Vecchia and Schaye (2012) implemented a stochastic feedback model. The basis of their model was the idea that particles heated by classical thermal feedback were allowed to be radiatively cool prior to star formation limiting how effective feedback could be in SFR suppression. Instead of heating all neighbour particles, they randomly selected a smaller number of nearby particles by a larger amount, resulting in lower SFRs. I include a model based on this concept. Like Dalla Vecchia and Schaye (2012) I define an energy increase,

$$\Delta_e = f \frac{E_{SN}}{N_{ngb}}, \tag{3.15}$$

where E_{SN} is the total SNe energy from a star particle during the timestep, N_{ngb} is the number of neighbour particles and f is a constant with a minimum value of 1. This energy increase represents the total amount of energy a single gas particle will receive from the SNe (regardless of distance). In order to determine if a gas particle will receive energy, a random number, r, is drawn and compared to the condition

$$r < \frac{E_{SN} M_*}{\Delta_e \sum_i^{N_{ngb}} M_i}, \tag{3.16}$$

where M_* is the mass of the star particle. If the condition is satisfied the gas particle receives an energy increase of Δ_e. Unlike Dalla Vecchia and Schaye (2012) my code has a variable Δ_e based on the SNe event, rather than a fixed value, due to the more complex SNe energy calculation used in the simulation code.

3.4.4 Mechanical Feedback

Additionally, I implement a mechanical feedback model, similar to those used in both Hopkins et al. (2014) and the mechanical feedback model of Smith et al. (2018). Mechanical feedback takes into account the work done on the gas by the expansion of the shock wave from the SNe.

The Sedov-Taylor phase of the expansion is the time during which the shock wave is energy conserving (i.e. energy lost due to cooling is low). This would modify the momentum the ith particle receives:

$$\Delta P = \Delta P_0 \times \sqrt{1 + \frac{M_{\text{i}}}{M_{\text{ej}} W_{\text{i}}}}, \tag{3.17}$$

where ΔP_0 is the momentum initially input into the gas, M_{i} is the mass of the ith particle and $M_{\text{ej}} W_{\text{i}}$ is mass received by the ith particle. This assumes that the Sedov-Taylor phase is resolved. Determining this is difficult, so instead the calculated enhanced momentum above is compared to the total momentum at the point where the shock wave exits the Sedov-Taylor phase,

$$\Delta P = \Delta P_0 \times 3 \times 10^{10} \left(\frac{Z}{Z_\odot} \right)^{-0.14} \frac{E_{\text{SN}}^{16/17} n_{\text{H}}^{-2/17}}{\sqrt{2 M_{\text{ej}} E_{\text{SN}}} 10^{51}} \text{ ergs cm s}^{-1} M_\odot, \tag{3.18}$$

where E_{SN} is the SNe energy for the timestep, n_{H} is the hydrogen number density of the gas and $\frac{Z}{Z_\odot}$ has a minimum value of 0.01. This is based on the comparison of total momentum and exit momentum used in Smith et al. (2018) and forms a limit for the maximum momentum that can be input into the gas particle (i.e. the case that the Sedov-Taylor phase is unresolved) and is used to modify the momentum instead if it is lower than what is calculated for the resolved shock wave. Practically this involves calculating both forms of momentum in the code for each star particle during each timestep and applying the lowest of the two modes.

3.5 Observations

Alongside theoretical models and simulations, observational data is crucial to the field of galactic archaeology. Quantities in simulated galaxies and stars provide the most benefit when they can be compared to the observed quantities and comparisons drawn. In this section I will provide a brief overview of the observational data I use in the following chapters and the limitations that it has.

3.5.1 The GALAH Survey

The GALactic Archaeology with HERMES (GALAH) survey is a spectroscopic survey of the Milky Way (Buder et al., 2018). Observations are made using the fibre-fed HERMES spectrograph on the Anglo-Australian Telescope. Fibre-fed spectrographs make use of moving fibre optics to take the spectra of multiple stars from a field, swapping out fibres during observations

to minimise observing time. HERMES uses four spectral bands: 471.8 – 490.3 nm, 564.9 – 587.3, 648.1 nm – 673.9 nm and 759.0 – 789.0 nm, in order to gather abundances from many nucleosynthetic processes. The spectra are converted to relative abundances, presented in the form [X/Fe], by comparing spectral lines. Parameters such as surface temperature are also calculated (via temperature dependent spectral lines such as Hα and Hβ). THe GALAH survey uses a broad selection process for stars and doesn't select targets based on metallicity. As a result the abundances give a good measure of the distribution of abundances in the solar neighbourhood. However, this is largely dominated by stars with $-1 \lesssim$ [Fe/H] $\lesssim 0$ and brighter stars, obscuring trends in both low metallicity and faint stars. This can be improved by using a more powerful telescope to observe a greater number of faint stars, and using targetted surveys of metal-poor stars, discussed in the next section.

3.5.2   Surveys of Metal-Poor Stars

Metal-poor stars play an important role in galactic archaeology; they contain the yields of fewer nucleosynthesis events making it easier to disentangle the process or processes that enriched them. I make use of three observational data sets to supplement the GALAH survey:

- 313 metal-poor stars from the work Roederer et al. (2014). Spectra were taken using the Magellan Inamori Kyocera Echelle spectrograph on the Magellan Telescopes, the Robert G. Tull Coude Spectrograph on the Harlan J. Smith Telescope and the High Resolution Spectrograph on the Hobby-Eberly Telescope.

- 27 faint metal-poor stars from Hansen et al. (2016). Spectra taken using the X-Shooter spectrograph on the VLT. This study aimed to determine abundances of carbon-enriched metal-poor (CEMP) stars.

- 51 stars in the metallicity range $-2.62 \lesssim$ [Fe/H] $\lesssim 0.24$ from Zhao et al. (2016). Spectra taken using Hamilton Echelle Spectrograph on the Shane 3m telescope.

These metal-poor stellar abundances are critical in testing trends in abundance patterns at low [Fe/H] which are poorly displayed in larger volume limited samples (the importance of these trends is discussed further in Chapters 4 and 5). However, because of the selection criteria, the relative amount of stars in particular [Fe/H] ranges is not accurate and can't be compared with theory.

Chapter 4

Simulations of r-process Chemical Enrichment

This chapter has previously been accepted as a paper for publication in Monthly Notices of the Royal Astronomical Society (Haynes and Kobayashi, 2019). The idea behind the paper was to introduce nucleosynthesis yields for NS mergers and MRSNe (as these are the two most likely r-process sites) into inhomogeneous chemodynamical simulations, compare these to observations and try to constrain the r-process site. I also included yields for neutrino winds and ECSNe. The paper is largely unchanged with the exception of section numbering and the expansion of the bimodality and initial conditions in the appendicies.

4.1 Introduction

Elements heavier than iron are produced by neutron-capture processes. There are two processes, slow and rapid (s-process and r-process), which differ in both site and nucleosynthesis yields but share the same basic mechanism: seed nuclei absorb neutrons which subsequently decay into protons via beta minus decay to increase the atomic number. For the s-process to occur the timescale for neutron absorption must be much longer than the timescale for beta minus decay. The steady neutron flux required for this is thought to result from He-burning, both in the centres of massive stars (producing the weak s-process elements up to roughly $A \lesssim 90$, see Prantzos et al. 1990, Frischknecht et al. 2016) and in the He-burning shells of low mass AGB stars (comprising the main s-process elements at $A \gtrsim 90$, see Smith and Lambert 1990 and Bisterzo et al. 2011).

In this paper we focus instead on the r-process, where a short neutron capture timescale allows for multiple neutron capture events to occur prior to beta minus decay. This particular method of
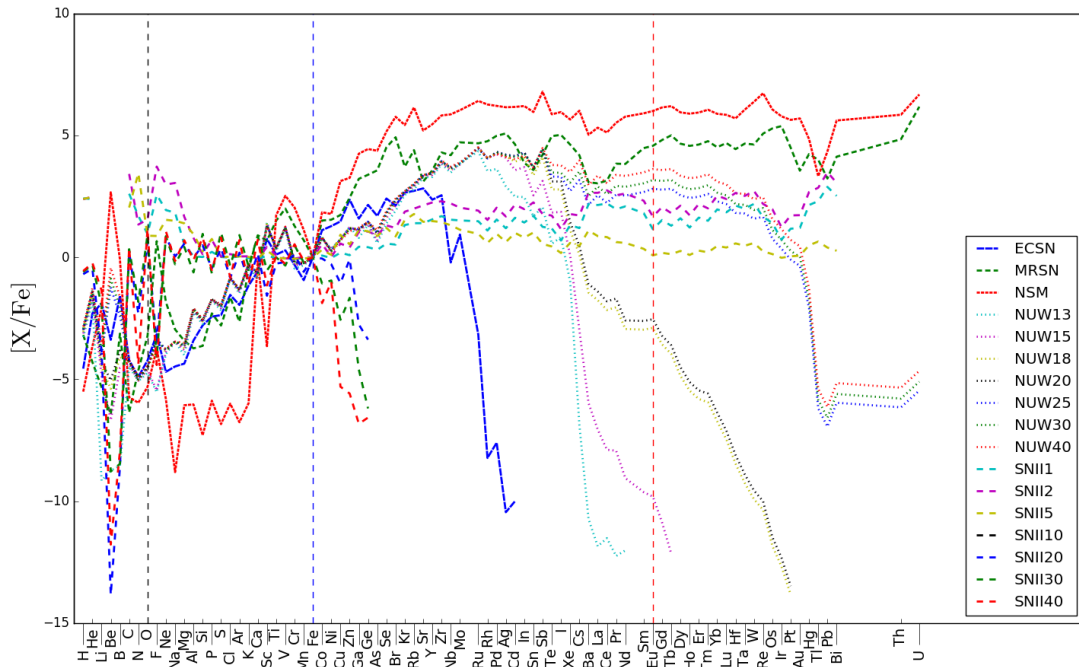
FIGURE 4.1: The nucleosynthesis yields relative to iron that we use in our simulations. SNII and AGB contribution for stars of 1 to 40 $M_\odot$ (SNII1 - SNII40) are shown as dashed lines. The yields for neutrino driven winds from stars of 13 to 40 $M_\odot$ are shown as dotted lines (NUW13 - NUW40). ECSNe, MRSNe and NS mergers are shown with the blue, green and red dashed lines respectively. Vertical dashed lines are shown at oxygen, iron and europium for ease of comparison.

nucleosynthesis is thought to be responsible for the assembly of the heaviest and most neutron-rich elements. The r-process requires extremely high neutron densities to operate and despite the limit this places on potential astrophysical sites the origin of the process remains a key unanswered question in galactic archaeology. Historically, there have been four theoretical sites: the dynamic ejecta of neutron star (NS) mergers (e.g., Lattimer and Schramm, 1974; Freiburghaus et al., 1999b), magneto-rotational supernovae (MRSNe, e.g., Cameron, 2003), Electron capture supernovae (ECSNe, e.g., Wanajo et al., 2011), and neutrino driven winds (NUW, e.g., Wanajo et al., 2001).

Because these events are intrinsically rare, it is necessary to consider inhomogeneous enrichment in modelling of the evolution of r-process elements. In previous works, stochastic chemical evolutions have been used (Cescutti et al. 2015, Wehmeyer et al. 2015, Ojima et al. 2017). The disadvantage of these models is that the star formation history has to be assumed for predicting the elemental abundances. In this paper, we use chemodynamical, hydrodynamical simulations, including relevant baryon physical processes (such as star formation and supernova feedback), to simulate the formation and evolution of Milky Way-type galaxies from cosmological initial conditions. These processes can play an important role in helping to determine which, if any, of these sites are dominant as they allow us to compare theoretical stars governed by these processes with what we observe in the solar neighbourhood and then make further predictions.

There have been several studies that have used hydrodynamical simulations to explore r-process enrichment; however they exclusively focus on NS mergers as the primary r-process site (Shen et al. 2015, van de Voort et al. 2015). NS mergers have long been a theoretical candidate, and their existence was strongly supported by the recent gravitational wave detection GW170817 (Abbott et al., 2017b), which is associated with an astronomical transient AT2017gfo (Valenti et al., 2017) and a short γ-ray burst GRB170817A (Abbott et al., 2017a). Analysis of the kilonova suggests that it is powered by the decay of a range of r-process elements including lanthanides (Tanaka et al., 2017) lending credit to the notion that NS mergers are a primary site for r-process production. However, it has been suggested that the timescale of NS mergers may not be short enough to explain the observations of r-process elements in extremely metal-poor stars, and thus nucleosynthesis at other sites (such as MRSNe) has also been studied (e.g., Argast et al., 2004).

In this paper, we incorporate the most recent theoretical yields for various r-process sites into our chemodynamical simulations in an attempt to constrain the dominant site. In Section 4.2, we briefly summarize the code and yield tables we use. Section 4.3 shows our results for isolated dwarf disc galaxies which we use to help determine parameters. In Section 4.4, we show our results for a Milky Way-type galaxy, compare with observational data from the literature and include relevant discussion. Finally, in Section 4.5 we present our conclusions.

4.2 Code and Yields

4.2.1 Hydrodynamical code

Our code is based on the smooth particle hydrodynamics (SPH) code GADGET-3 (see Springel 2005 for the previous version GADGET-2). The gravity for all particles is computed with tree method gravitational N-body dynamics and the gas elements are modelled using the entropy-conserving SPH formulation from Springel and Hernquist (2003). A grid method is employed to govern the outermost dark matter particles that occur as a result of the initial conditions we use. We also include the relevant physical baryonic processes from Kobayashi et al. (2007a), which can be summarized as follows:

UVB Heating: Heating from UV background radiation is included to reproduce the observed metallicity distribution function in the solar neighbourhood (Fig 14 of Kobayashi and Nakasato 2011).

Radiative Cooling: The radiative cooling we use includes a metallicity dependency in the cooling functions calculated using the MAPPINGS III code from Sutherland and Dopita (1993). [Fe/H] is used as the metallicity for the calculations, and the observed [α/Fe]-[Fe/H] relation

in the solar neighbourhood is assumed. In addition, kernel weighted smoothing for cooling (Wiersma et al. 2009) is included. The impact depends on the resolution of the simulations: Kobayashi (private. comm.) found that it gives a better SFR for Milky Way simulations as in this paper, but not for cosmological simulations as in Taylor and Kobayashi (2014).

Star Formation: We use the star formation conditions from Katz (1992), namely that there be convergent gas flow, rapid cooling and the gas is Jeans unstable. Star formation rate is related to the dynamical timescale by $\tau_{sf} = \frac{1}{c}\tau_{dyn}$ where we use a value of c = 0.1. The value is initially taken from Kobayashi (2005) and shown in Kobayashi and Nakasato (2011) to better match abundance ratios in the Milky Way.

Provided that a gas particle meets the above conditions, it will spawn a star particle of roughly half the mass of the initial mass of the gas particle. Star particles are a collection of stars rather than a single stellar object; we model this as a simple stellar population with a mass distribution in the newly spawned particle following the Kroupa initial mass function (Kroupa, 2008) between 0.07 and 120 $M_\odot$.

Feedback: Supernovae (SNe) and stellar winds eject energy, mass and elements from the star particles back into the surrounding gas particles. These quantities are distributed to the 64 $\pm$ 2 nearest neighbour gas particles within a dynamic feedback radius and are weighted by the smoothing kernel used for the SPH. In this paper we model the energy feedback as entirely thermal, i.e., all energy from supernovae and stellar winds is distributed to the surrounding gas particles as thermal energy weighted by the kernel. The modelling of feedback is debated and we have tested kinetic feedback as in Dalla Vecchia and Schaye (2008) and a stochastic thermal model as in Dalla Vecchia and Schaye (2012) with our chemical enrichment method. With our code and resolution, we find that thermal feedback gives a better match with the elemental abundance distribution of the Milky Way than the other feedback methods (Haynes & Kobayashi, in prep.) and thus we elected to use our default feedback model in this paper.

It should be noted that no explicit sub-grid diffusion scheme for metals between gas particles (Shen et al. 2010) is included in our model. This could change [Fe/H] but the effect on [X/Fe] for elements produced from the same sources should be less pronounced. Kobayashi (private. comm.) found that the simple diffusion equation gives too low scatter in [Fe/H] compared to observations, although it depends on the resolution and the details of the feedback modelling. The effect of additional mixing can be tested with kernel weighting (Crain et al., 2013) and we find that this effect should be small (see Appendix C).

4.2.2   Chemical Enrichment

The chemical enrichment included in our simulations is based on the model from Kobayashi (2004). We detail this below with the modifications made to accommodate the additional processes from r-process nucleosynthesis.

Core-Collapse (CC) SNe: CCSNe includes all SNe events driven by gravitational core collapse (Type II and Ibc) SNe (SNII). We also include hypernovae (HNe), which correspond to broadline SNe Ibc. Both yields are taken from Kobayashi et al. (2011) and govern stars between masses of 10 - 50 $M_\odot$; stars with $M > 50 M_\odot$ are assumed to collapse directly to a black hole and not to return newly synthesized metals. The HNe occurrence fraction is metallicity dependent: f_{HNe} = 0.01, 0.01, 0.23, 0.4, 0.5, and 0.5 for Z = 0.05, 0.02, 0.008, 0.004, 0.001, and 0.0, respectively, and linearly interpolated for values in between (Kobayashi and Nakasato, 2011).

Asymptotic Giant Branch (AGB) Stars: Stars with $\sim$ 1-8 $M_\odot$ are also able to produce some metals during the AGB phase, including the heavy s-process elements. This occurs as the He shell surrounding the core pulses and allows a downflow of protons to form a ^{13}C-rich "pocket" which can drive neutron production via α absorption (and hence s-processing). We adopt the latest nucleosynthesis yields of the AGB stars from Karakas and Lugaro (2016).

Stellar Winds (SW): All stars return their envelopes containing unprocessed metals to their surroundings at the end of their lives. These metals are those that existed in the gas from which the star was formed and have their own chemical composition.

Type Ia SNe (SNIa): We adopt the SNIa yields of the standard W7 model from Nomoto et al. (1997). Our progenitor model is based on single-degenerate scenario with white dwarf winds (Kobayashi and Nomoto, 2009), where the rate depends both on the lifetime of the secondary stars and the metallicity of the progenitor systems, and gives good agreement with observed [α/Fe] and [Mn/Fe] ratios. This model also gives a power-law lifetime distribution (Fig 2 of Kobayashi and Nomoto 2009) at $Z \geq Z_\odot$, very similar to the observed delay-time distribution (Maoz et al., 2014).

NS Mergers: NS mergers provide a site for the r-process in the neutron rich dynamic ejecta created as the binary system merges. We include yield tables for NS-NS mergers (both 1.3 $M_\odot$) from Wanajo et al. (2014) and for NS-BH mergers. The NS-NS merger and NS-BH merger delay time distributions (DTD) of simple stellar populations are taken from the binary population synthesis calculations in Mennekens and Vanbeveren (2014) (model 2 for $Z = 0.02$ and 0.002). The resulting yields are added to the metals released from each star particle at every time step. We also introduce a free parameter, f_{NSM}, representing the fraction of stars in binary systems in our simulations. We choose an initial value of $f_{NSM} = 0.5$, independent of metallicity.

MRSNe: Rapidly rotating massive stars with strong magnetic fields may provide a potential site for r-process nucleosynthesis at the inner boundary of the accretion disc formed around the central collapsed object (Cameron, 2003). We use the yield tables presented in Nishimura et al. (2015) for a 25 $M_\odot$ star (B11β1.00 model). This event could be related to HNe events, which also require rotation and magnetic fields; recent simulations of supernova explosions have not succeeded in exploding very massive stars (M $\gtrsim$ 25 $M_\odot$) (Janka, 2012). Therefore, we replace a fraction of HNe events with MRSNe. The number of stars with suitable conditions for MRSNe is poorly constrained so we introduce a free parameter, f_{MRSN}, representing the fraction of stars with the correct conditions. Our initial value is $f_{MRSN} = 0.01$, independent of mass and metallicity, as it gives solar values at [Fe/H]$= 0$ and reasonable agreement with observations.

ECSNe: We adopt yields from Wanajo et al. (2013) for a 8.8 $M_\odot$ star and metallicity dependent ($\log Z = -4, -3, -2.4, -2.1, -1.7$) limits of the progenitor mass with the upper (8.4, 8.4, 9.0, 9.65, 9.9 $M_\odot$) and lower (8.2, 8.25, 8.8, 9.5, 9.75 $M_\odot$) bounds (Doherty et al., 2015). For metallicities above or below the limits, we assume the rates derived from the upper and lower limits, respectively. These yields are added directly onto the ejected material from each star particle with the corresponding age.

NUW: Ejecta heated by neutrinos from proto-neutron stars can provide a site from r-process enrichment. The yields are taken from Wanajo (2013) for stars between 13 and 40 $M_\odot$ with a conversion between the stellar masses (13, 15, 20, 40) $M_\odot$ and the respective NS masses (1.4, 1.6, 1.8, 2.0) $M_\odot$ based on Kobayashi, Karakas, Lugaro (in prep). These yields are added to the SNII yields.

Figure 4.1 shows a comparison of the yields we use. From this we show that SNII and AGB only contribute significantly to elements up to the iron peak elements, whilst heavier elements are dominated by NS mergers and MRSNe. ECSNe produce a relatively large amount of low mass heavy elements but drop off entirely after cadmium. NUW produce elements up to and including uranium but in very low amounts compared to NS mergers and MRSNe.

4.3   Isolated Dwarf Disc Galaxies

In this section we present the results of our first simulations using isolated rotating gas clouds in static dark matter potentials as a test for our code and to choose parameters. The combined mass of the dark matter halo and gas is 10^{10} h^{-1} $M_\odot$ with a 0.1 baryonic fraction and spin parameter, $\lambda = 0.1$, divided into 160 000 gas particles (see Kobayashi et al. 2007b). As the simulation begins and star formation and SNe begin to take place, the cloud radiatively cools and collapses into a disc with a stellar mass of $\sim 10^7$ $M_\odot$.
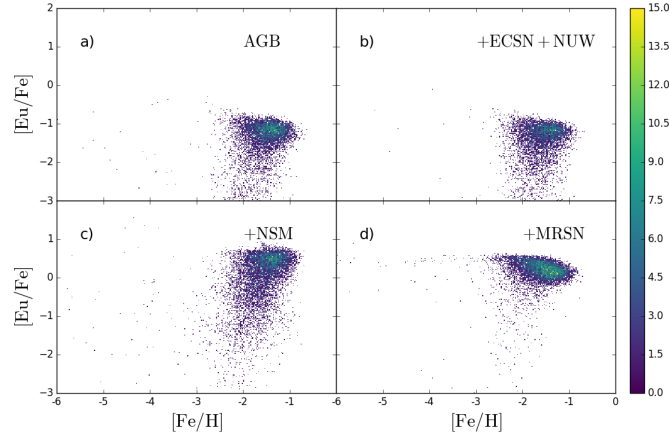
FIGURE 4.2: [Eu/Fe] plotted against [Fe/H] for the star particles in four simulations of an isolated dwarf disc galaxy: SNII + SNIa + AGB only control, NUW, NS mergers and MRSNe. The colour gradient shows the linear number of star particles per bin.
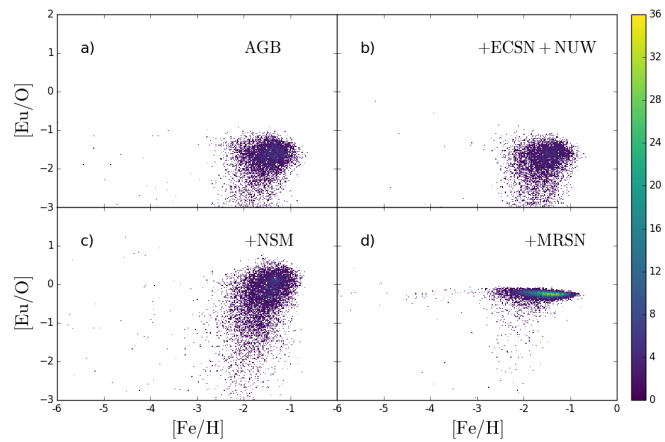
FIGURE 4.3: The same as Figure 4.2 but showing [Eu/O] plotted against [Fe/H].

We show four different simulations. The first is effectively a control simulation with chemical enrichment just from SNII and SNIa plus the AGB yields. The remaining three simulations include the same chemical enrichment as the control but also include one of the additional r-process sites: ECSNe + NUW, MRSNe and NS mergers, respectively. We group the NUW and ECSNe into one simulation because of their relatively low yields (see Figure 4.1). We ran many low resolution (10000 particles) simulations, changing parameters, and found that $f_{\mathrm{MRSN}} = 0.01$ for MRSNe and $f_{\mathrm{NSM}} = 0.5$ for NS mergers gave a good match to the solar abundance ratios (see Figure 4.4 below).

Figure 4.2 shows the [Eu/Fe] abundance ratios for the star particles in the isolated dwarf disc galaxies resulting from these simulations. Panel (a) shows the SNII + SNIa + AGB simulation (hereafter referred to as the control simulation), which depicts the base level of europium provided by the contribution from AGB stars, with no additional r-process included. As expected, given the low [Eu/Fe] in from Figure 4.1, the NUW and ECSNe model shown in the panel
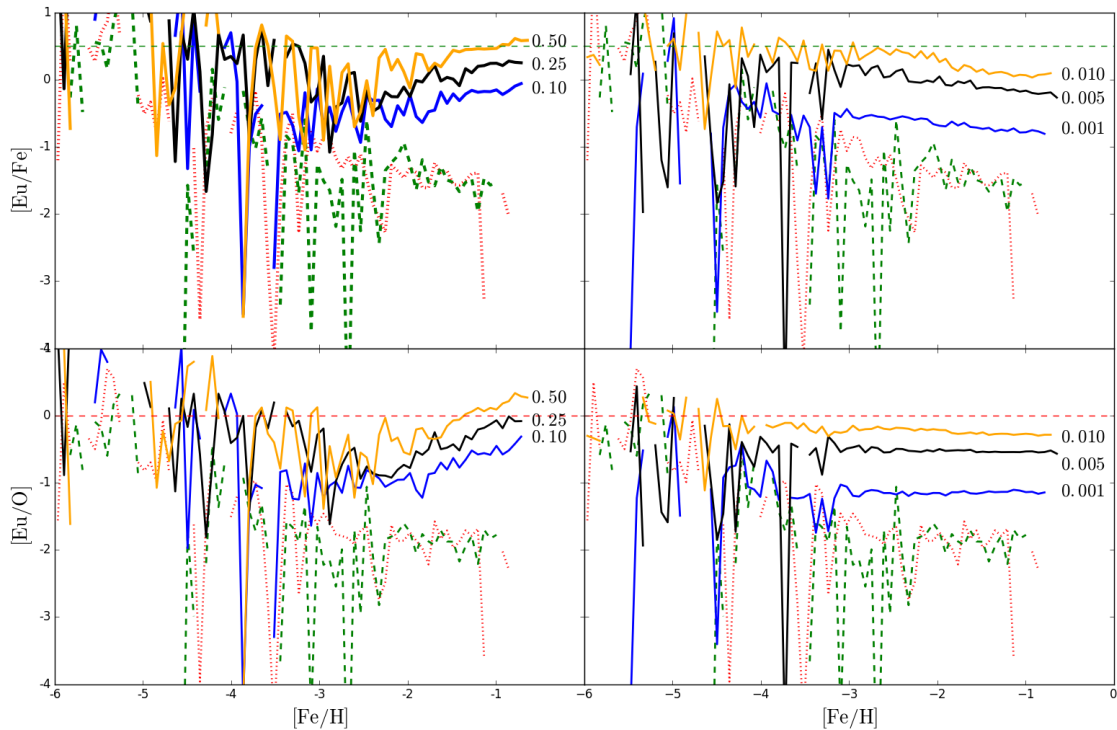
FIGURE 4.4: Median [Eu/Fe] and [Eu/O] ratios as a function of [Fe/H] for star particles in our low resolution isolated dwarf disc galaxy simulations with NS mergers (left panels) and MRSNe (right panels). Red dotted and green dashed lines show the control and ECSNe + NUW respectively. The blue, black and orange labelled lines show differing values of f_{NSM} (0.1, 0.25 and 0.5) and f_{MRSN} (0.001. 0.005, 0.01) respectively. Horizontal dashed lines show [Eu/Fe] = 0.5 and [Eu/O] = 0.

(b) provides only a small boost to [Eu/Fe] at [Fe/H] ~ -2. Panels (c) and (d) show the NS merger and MRSNe models, respectively. Both increase the level of [Eu/Fe] substantially and to roughly the same level, with NS mergers having a much larger range in scatter between [Fe/H] ~ -2.5 and [Fe/H] ~ -1. For both models, we obtain [Eu/Fe] ~ 0.5 at [Fe/H] ~ -2, which is consistent with observations in nearby dwarf spheroidal galaxies (Tolstoy et al., 2009). We note that across all models we are able to reproduce the scatter in [Eu/Fe] at low [Fe/H] that has been observed. This is due to the sporadic production of iron at low [Fe/H] prior to SNIa occurring so even relatively weak europium production can result in high [Eu/Fe].

In Figure 4.3 we plot [Eu/O] against [Fe/H]. We choose this particular combination as oxygen is one of the α elements (O, Mg, Si, S, and Ca) and primarily produced in CCSNe. MRSNe are a subset of CCSNe, so oxygen should be produced at the same time, while NS mergers are independent of the occurrence of CCSNe. Additionally, by removing the Fe contribution from SNIa, we can see the relative contribution to Eu from CCSNe and neutron capture processes more directly. The panels have the same layout as Figure 4.2, and the panels (a) and (b) again show only a very minor increase in [Eu/O] with the addition of NUW and ECSNe. Panels (c) and (d) show a significant difference in [Eu/O] between the NS merger and MRSNe models. NS mergers keep the large scatter at [Fe/H] $\gtrsim -3$ seen in Figure 4.2. However, with MRSNe the

scatter is greatly reduced to form a narrow elongated peak for [Fe/H] $\gtrsim -4$. This is due to the fact that under the MRSNe model the primary source of europium and the primary source of α elements are both CCSNe and will therefore have similar timescales. In both models [Eu/O] approaches ~ 0 at [Fe/H] $\sim$ -1.

As mentioned earlier, in Figure 4.4 we summarize our parameter study result, showing the median [Eu/Fe] and [Eu/O] ratios of star particles in low resolution (10000 particles) isolated dwarf disc galaxies with different parameter choices. We note here that although these low resolution simulations display slightly decreased [X/Fe] at high [Fe/H] due to lowered SFR (see Appendix A), this is not of concern as our primary diagnostic is the [Eu/Fe] value at [Fe/H] ~ 2. Our choices of $f_{\mathrm{MRSN}} = 0.01$ for MRSNe and $f_{\mathrm{NSM}} = 0.5$ roughly give [Eu/Fe] ~ 0.5 and [Eu/O] ~ 0, therefore we use these values in the following section. With [Eu/O] ratios, we can remove the contribution from SNIa, which may be different in low-metallicity galaxies (Kobayashi et al., 2015).

4.4 Milky Way Galaxies

In this section, we utilise cosmological zoom-in initial conditions for a Milky Way-type galaxy from the Aquila comparison project (Scannapieco et al., 2012) with cosmological parameters as follows: $\mathrm{H_0} = 100h = 73$ km s^{-1} Mpc^{-1}, $\Omega_0 = 0.25$, $\Omega_\Lambda = 0.75$, $\Omega_B = 0.04$. The initial mass of each gas particle is $3.5 \times 10^6 \mathrm{M_\odot}$ and the gravitational softening length is 1 kpc h^{-1}. We choose these conditions because they give a galaxy with morphology, size and merger history reasonably similar to the Milky Way (see the G3-CK model in Scannapieco et al. 2012). The elemental abundance pattern, such as [α/Fe]-[Fe/H] and [Eu/Fe]-[Fe/H] relations, depends on the accretion history of galaxies (Mackereth et al., 2018) which could potentially be a source of systematic uncertainty. We should note, however, that our simulated galaxy displays the observed [O/Fe] bi-modality (Haynes & Kobayashi, in prep, see Appendix B). With the same initial conditions, we run the simulation set shown in the previous section: a control galaxy (SNII + SNIa + AGB) and adding ECSNe + NUW, NSM or MRSNe. We again assume parameters of $f_{\mathrm{MRSN}} = 0.01$ and $f_{\mathrm{NSM}} = 0.5$ for MRSNe and NS mergers, respectively.

Unlike the isolated dwarf disc galaxies from Section 4.3, N-body dynamics is used to govern dark matter behaviour to allow a central galaxy to form hierarchically in a series of mergers from cosmological initial conditions. This is easily seen in Figure 4.5 which shows the edge-on views of the evolution of the stellar mass in 100 kpc boxes (first five panels) and a 30 kpc box (final panel) for the control simulation. The disc inclination is corrected to horizontal using the cross product vectors of the angular momentum and position vectors for each star particle. Table 4.1 shows galactic properties in our simulations for the two regions: the central disc, defined as a 10 kpc radius disc with a height of ± 2 kpc, and the solar neighbourhood, defined as the
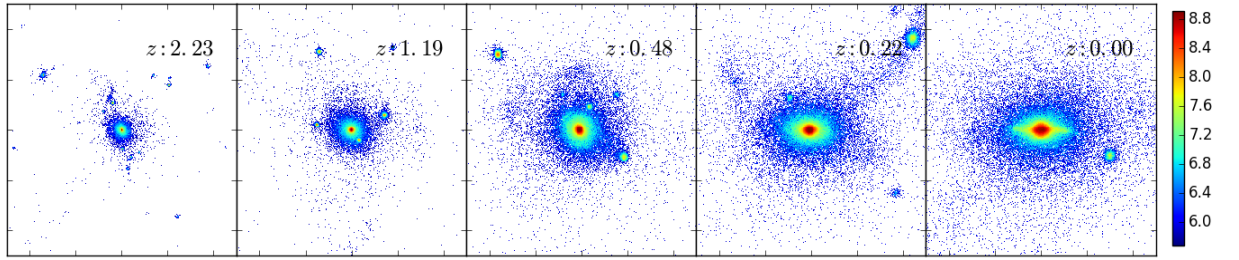
FIGURE 4.5: Projected maps of stellar mass from a comoving 100kpc box around the central galactic disc (first 5 panels) using the control simulation at a variety of redshifts (listed on each individual panel). The colour bar shows the logarithmic projected mass in $M_\odot (\frac{1}{3}\text{kpc})^{-2}$.
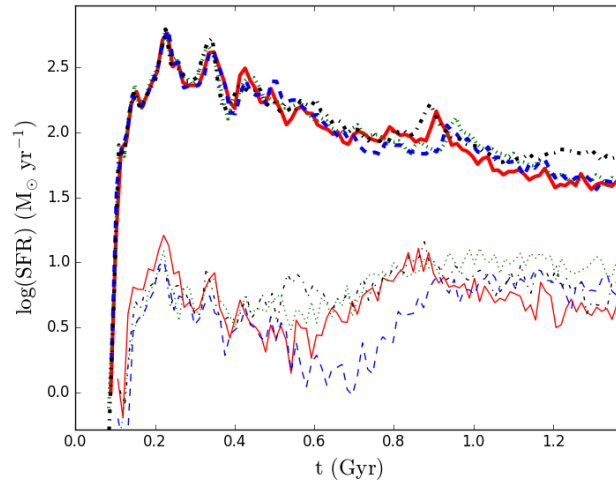
FIGURE 4.6: Star formation histories for the central 10 kpc (with height $\pm$ 2) of the galaxy (bold lines) and solar neighbourhood (thin lines). We show the star formation history for the control simulation, NUW + ECSNe, NSM and MRSNe with the red solid, green dotted, blue dashed and black dashed-dotted lines respectively.

	10 kpc disc					Solar Neighbourhood			
Simulation	M_{gas}	M_*	f_*	SFR	Effective SN	M_{gas}	M_*	f_*	SFR
	10^9 $M_\odot$			$M_\odot$ y^{-1}	kpc	10^9 $M_\odot$			$M_\odot$ y^{-1}
Control	10.57	97.19	0.90	40.12	5.688 - 7.438	1.54	4.13	0.73	4.7808
ECSN + NUW	11.64	100.32	0.90	44.35	5.883 - 7.693	2.91	5.64	0.66	11.64
NSM	10.60	96.02	0.90	43.03	6.500 - 8.500	2.23	3.55	0.61	8.44
MRSN	11.31	100.84	0.90	63.63	6.812 - 8.908	1.75	4.91	0.74	7.72

TABLE 4.1: The properties for the simulated galaxies at $z = 0$. All masses are given in terms of 10^9 $M_\odot$ and SFR is given in $M_\odot$ y^{-1}. Values in the first half of the table are given for a central 10 kpc disc with height $\pm$ 2 kpc. Values in the second half correspond to the particles within the effective solar neighbourhood as given.
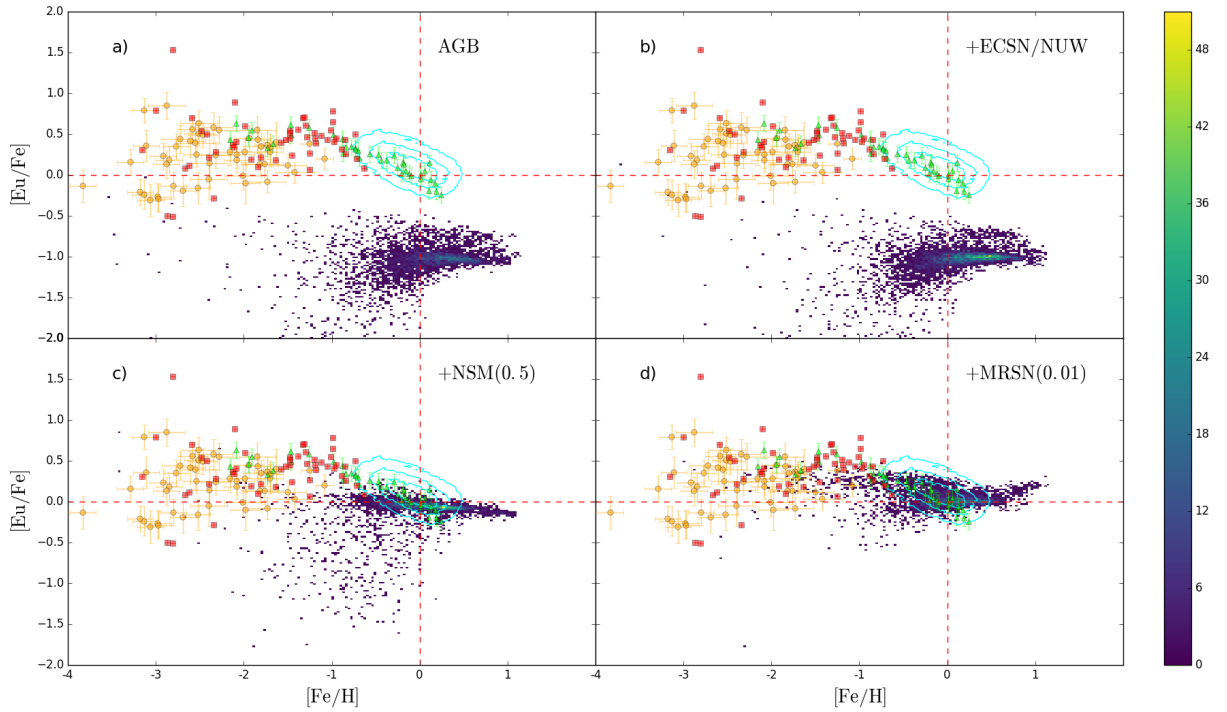
FIGURE 4.7: [Eu/Fe] plotted against [Fe/H] for the star particles in the solar neighbourhood in our Milky Way simulations at $z = 0$. The panels in order show: control, ECSNe + NUW, NS mergers and MRSNe. We compare against four data sets: Hansen et al. (2016, red squares), Roederer et al. (2014, orange circles), Zhao et al. (2016, green triangles) and Buder et al. (2018, HERMES-GALAH, cyan contours). The contours show 10, 50 and 100 stars per bin. The red dashed lines denote 0 for both [Eu/Fe] and [Fe/H] which we expect to lie within our data. The colour bar shows the linear number of points per bin.
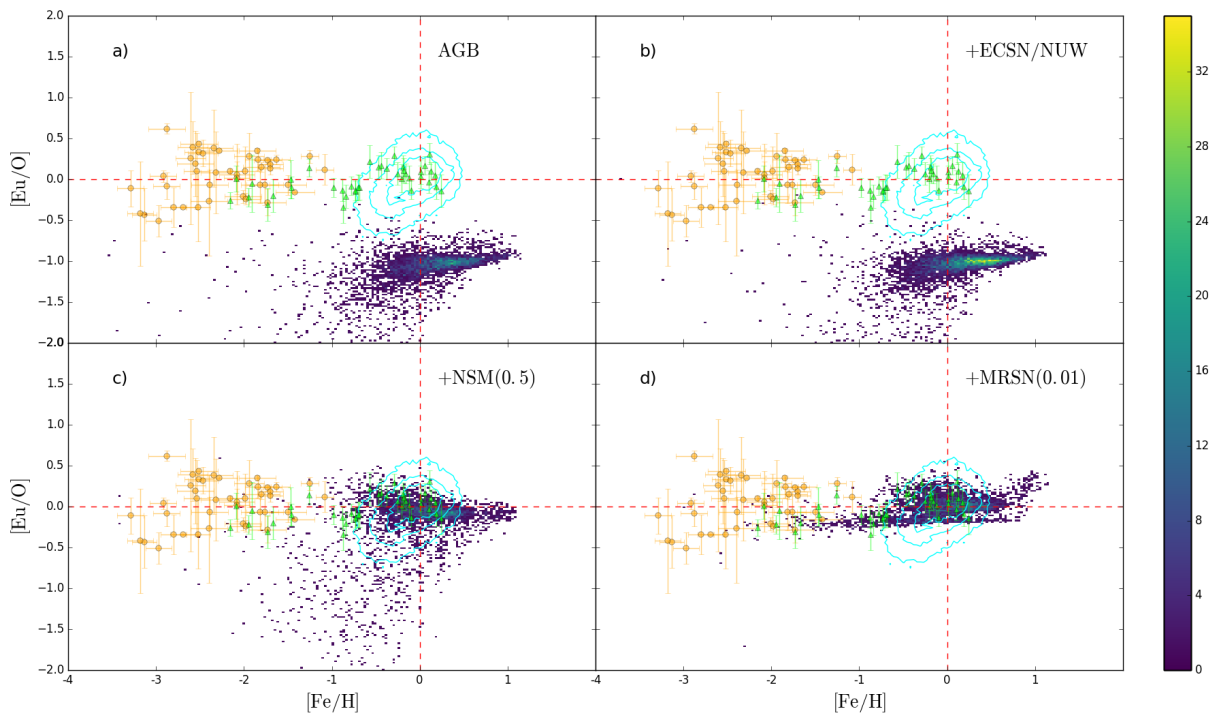
FIGURE 4.8: The same as Figure 4.7 but with [Eu/O] plotted against [Fe/H].
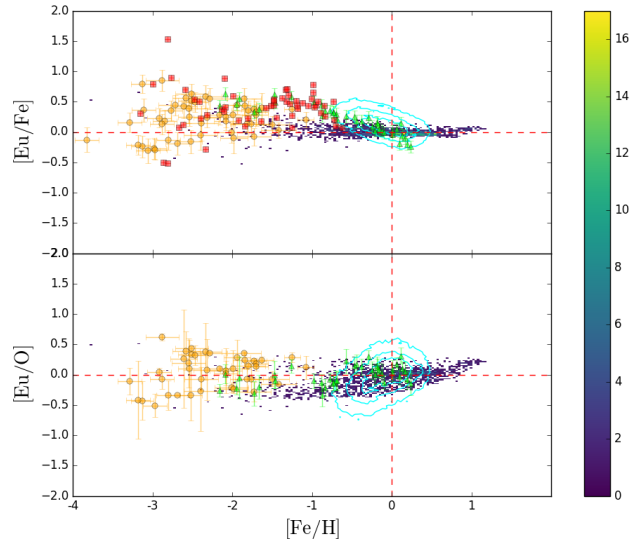
FIGURE 4.9: As Figure 4.7 but showing [Eu/Fe] and [Eu/O] plotted against [Fe/H] for the combined NSM and MRSN simulation.
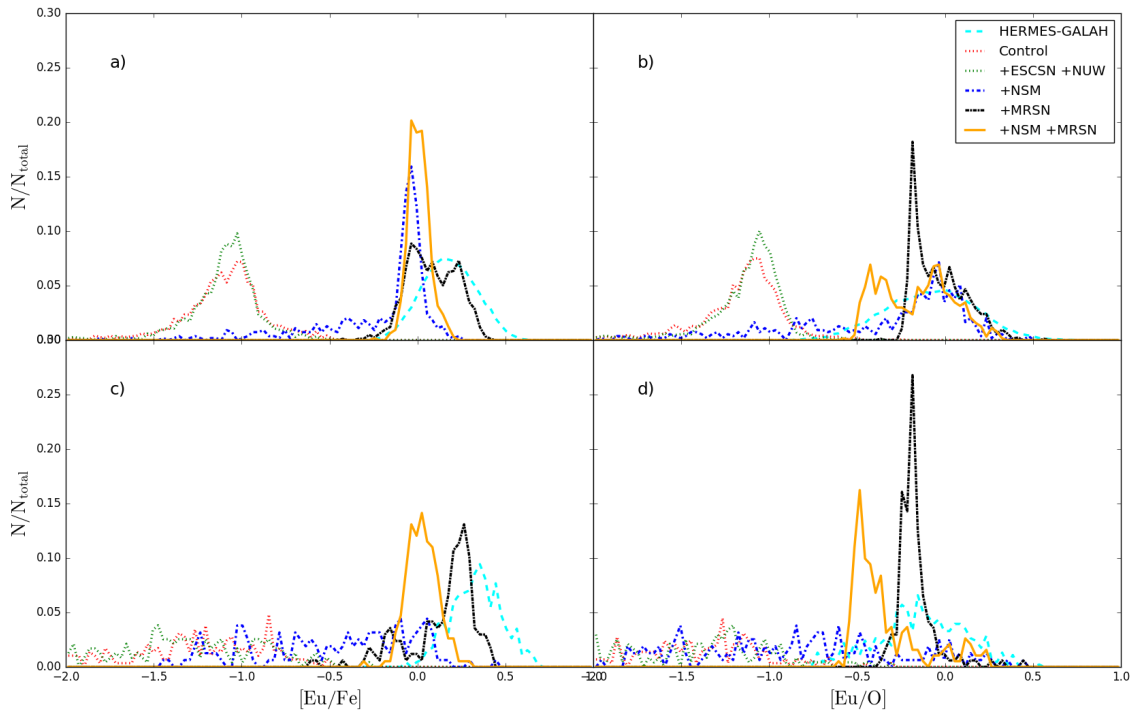
FIGURE 4.10: [Eu/Fe] distribution of star particles in the solar neighbourhood of our Milky Way simulations at $z = 0$, for selected [Fe/H] ranges and normalised by the total number of points. Panels (a) and (b) show the distribution of points for $-0.75 \lesssim$ [Fe/H] $\lesssim 0$ for [Eu/Fe] and [Eu/O] respectively. Panels (c) and (d) show the same distributions for the range $-1.5 \lesssim$ [Fe/H] $\lesssim -0.75$. The red, green, blue, and black lines show the control, ECSNe + NUW, NS mergers, and MRSNe, respectively. The orange lines show the combined model of NS mergers and MRSNe, and the cyan dashed line shows the HERMES-GALAH data in the same [Fe/H] ranges.

"hollow cylinder" with inner boundary at 6.5 kpc, outer boundary at 8.5 kpc and extending $\pm$ 1 kpc above and below the plane of the disc. Due to the nature of hydrodynamical simulations, the total stellar mass and morphology of the galaxy differs slightly between each simulation. To account for this we instead define an effective solar neighbourhood by comparing the scale widths of the simulated galaxies with the Milky Way scale width (using a figure of 2.1 ± 0.3), and adjusting the inner and outer boundaries by using the ratio between values as a simple multiplier. Finally, Figure 4.6 shows the star formation rates (SFRs) for the previously defined central disc (dashed lines) and the solar neighbourhood (dotted lines) for each model. The star formation rate for the galaxy is in reasonable agreement with that from the G3-CK model in Scannapieco et al. (2012).

Figure 4.7 plots [Eu/Fe] abundances against [Fe/H] for each simulations effective solar neighbourhood. In addition we plot four observational data sets comprising derived abundances from Hansen et al. (2016), Roederer et al. (2014), Zhao et al. (2016) and the HERMES-GALAH data set from Buder et al. (2018). Given the large number of observations in the HERMES-GALAH data, we condense the data into contours showing 10, 50 and 100 data points per bin (0.038 width by 0.02 height) for legibility. This results in some outlying data points not being shown towards the left hand side [Fe/H] ~ -1 though has little effect on the high [Fe/H] edge of the data set. We also note here that the density of observed points is unrelated to the density of simulated points outside of the HERMES-GALAH data set, as the other sets are exclusively surveying low metallicity stars.

Panel (a) shows the control simulation with the AGB contributions but no additional r-process sites. The spread of [Eu/Fe] sits well below observational values; [Eu/Fe] is at ~ -1 for [Fe/H] $\gtrapprox -1.5$. Panel (b) shows the addition of both NUW and ECSNe to the AGB model. As with the isolated clouds (Section 4.3), the addition is insufficient to boost [Eu/Fe] to the observed levels and the overall trend remains at [Eu/Fe] ~ -1. This is in line with what we would expect to see from Figure 4.1: no Eu enrichment from ECSNe and only a small contribution from NUW.

Panels (c) and (d) show simulations using NS mergers and MRSNe, respectively. As with the addition of the NUW and ECSNe models, we have included these yields in tandem with the AGB model. Both NS mergers and MRSNe increase [Eu/Fe] to ~ 0 at [Fe/H] $= 0$, though with the caveat that both make use of a free parameter that allows the level to be adjusted reasonably freely in our simulations.

At [Fe/H] $\lessapprox -1.5$ the simulated level and scatter of [Eu/Fe] in the MRSNe model matches the observational data much better than the NS mergers model. This is a result of delay times before NS merger events can occur, as NS binaries need to both form and coalesce. MRSNe events, on the other hand, are assumed to be a subset of 25 - 40 $M_\odot$ HNe in our simulations and able to start producing r-process elements almost immediately after the formation of stars. Additionally, the NS merger model displays a large amount of scatter below the main trend of at

[Fe/H] $\lesssim$ 0. We already see a similar scatter at the same [Fe/H] range in the control simulation; the scatter we see in NS mergers is likely produced by AGB stars. However, this same pattern of scatter is not present in the MRSNe simulation. In this case it appears that the production of Eu from NS mergers is too slow to raise [Eu/Fe] to observed levels at [Fe/H] < -1 and instead slowly increases [Eu/Fe] between $-2 \lesssim$ [Fe/H] $\lesssim$ 0. However, MRSNe events are able to enrich the ISM prior to AGB contributions so no such scatter is seen. Although MRSNe replicate the trend in this region substantially better, it presents a flat trend above [Fe/H] ~ -1 where the observational data suggests a downward trend. NS mergers have a slight downward trend in this region, though not as steep as the observed data.

Both the scatter and average [Eu/Fe] are important for constraining the r-process. SNIa produce substantial amounts of Fe which contributes to the scatter in Figure 4.7, so we show the [Eu/O] comparison in Figure 4.8 in order to remove the SNIa contribution. As with Figure 4.7 the control and the ECSNe + NUW model and sit well below observations with the latter providing only a small peak at [Eu/O] ~ -1. The MRSNe model shows higher [Eu/O] at [Fe/H] $\lesssim -1$ and provides a better match to the observational data than the NS merger model in this region. The large scatter at [Fe/H] $\lesssim$ 0 in the NS merger model is still present as in Figure 4.7, again suggesting a slow increase in [Eu/O] due to the contribution from NS mergers. Conversely, the MRSNe overpredicts the level of [Eu/O] at [Fe/H] ~ -0.5, where the observational data might suggest more scatter should exist in [Eu/O]. In the region of [Fe/H] $\gtrsim -0.5$, both models predict a reasonably flat overall trend, however neither matches the scatter particularly well; NS mergers predict a large scatter below [Eu/O] $\sim$ 0 and MRSNe predicts a trend that is too narrow.

At [Fe/H] $\gtrsim$ 0, panels (d) of Figures 4.7 and 4.8 show predicted [Eu/Fe] and [Eu/O] ratios that increase from [Fe/H] $\sim$ 0. This upturn is the result of decreased O and Fe production as a result of MRSNe totally replacing HNe contribution. As described in Section 4.2, we have a metallicity dependent fraction of CCSNe that are HNe, with a constant f_{MRSN}. At $Z = Z_\odot$, both fractions have a value of 0.01, which gives much larger Eu relative to O and Fe (Figure 4.1). Although there are no stars at [Fe/H] $\gtrsim$ 0.5 in the observational data, [Eu/O] seems to increase while [Eu/Fe] seems to decrease from [Fe/H] $\sim$ 0 to higher [Fe/H]. This may suggest some metallicity dependence of f_{MRSN}, similar to that which is applied for HNe in our model.

The observed data points in Figure 4.8 give us some insight into the timescales involved in europium production in the two models. By comparing europium to an α element (in this case oxygen, though all α elements provide similar results) we compare europium production with an element produced primarily in SNII/HNe. The observed data shows a largely flat [Eu/O] trend as a function of [Fe/H]. This suggests that europium is produced primarily at the same rate (normalised to solar) as oxygen is. We assume that MRSNe events are a subset of CCSNe with conditions (e.g., rotation and magnetic fields) sufficient to produce r-process elements. Given that SNII and HNe are the primary production sites of α elements, if MRSNe are a primary site

for the r-process then most europium production would also be accompanied by α elements, leading to the observed flat [Eu/O] over a wide range of [Fe/H].

We also consider the possibility that the poor match between NS mergers and observational data could be rectified by the inclusion of MRSNe. In order to examine this, we ran a simulation that incorporated both NS mergers and MRSNe. We opted to use the same parameters for NS mergers but halved the MRSNe efficiency to $f_{MRSN} = 0.005$ in an effort to prevent the overproduction of Eu at high [Fe/H]. The results of these simulations are shown in Figure 4.9. The upper panel shows [Eu/Fe] for the combined processes and the lower panel shows [Eu/O]. The [Eu/Fe] fit with the data is slightly worse than our MRSNe model at [Fe/H] $\lesssim -1.5$ as the smaller MRSNe contribution pulls down the overall values. The scatter seen below the observed data in the NS merger models has disappeared completely in both [Eu/Fe] and [Eu/O]. The overall trend in [Eu/Fe] is very flat and below [Fe/H] ~ 0 the model underpredicts [Eu/Fe] resulting in the MRSNe model providing a better fit.

Figure 4.10 shows the [Eu/Fe] (panels a and c) and [Eu/O] (panels b and d) distributions for the ranges $-0.75 \lesssim$ [Fe/H] $\lesssim 0$ (panels a and b) and $-1.5 \lesssim$ [Fe/H] $\lesssim -0.75$ (panels c and d). The dotted lines show our four initial simulations shown in Figures 4.7 and 4.8, and the orange solid lines are for the combined NS merger and MRSNe simulation in Figure 4.9. The cyan dashed lines show the HERMES-GALAH observational data set. The control simulation (red) and the combined ECSNe and NUW model (green) show low peaks at [Eu/Fe] ~ -1 in the panels (a) and (b) and diffuse scatter for [Eu/Fe] $\lesssim -0.5$ in the panels (c) and (d). They are both poor matches for the HERMES-GALAH data. In the panel (a) NS mergers show a narrow peak with [Eu/Fe] ~ 0 as opposed to the broader peak at [Eu/Fe] ~ 0.2 for the HERMES-GALAH data and in the panel (b) they do not account for the observed high values of [Eu/O] $\gtrsim 0.5$. Although NS mergers (blue) seem to give the best match in panel (c), they show a scatter in the range $-0.5 \lesssim$ [Eu/Fe] $\lesssim -0.2$ where the HERMES-GALAH data shows no stars in panels (c) and (d). The MRSNe model (black) provides a better match in terms of peak position of [Eu/Fe] (panels a and c), and shows no scatter in the $-0.5 \lesssim$ [Eu/Fe] $\lesssim -0.2$ range in the panel (a). Additionally, the MRSNe model gives fairly good fit in the panels (c) and (d). Finally, the combined NS merger and MRSNe model (orange) provides a worse fit with the data than the MRSNe model in panels (a) and (c). However, it does provide a better fit than MRSNe in panel (b).

It is of great interest whether our conclusions depend on our numerical resolution. Although we have not explored the impact of varying resolution on [Eu/Fe] and [Eu/O], we do not think that this changes our conclusions for the following reasons. van de Voort et al. (2015) found that increasing the resolution of their simulations increased the scatter in the [r-process/Fe] ratios at $-2.5 <$ [Fe/H] < 0 and decreased the median value at [Fe/H] < -2. We predict that increasing our resolution would make NS mergers less consistent with observations.

In summary, the better [Eu/Fe] agreement is seen in the MRSNe model when compared to the NS merger model at [Fe/H] $\lesssim -1.5$ in Figure 4.7. This suggests that at such low [Fe/H], MRSNe are the dominant r-process site. Figure 4.10 provides further support for this by highlighting the increased scatter in the NS merger model. This is in agreement with the galactic chemical evolution models (GCE) with binaries from Mennekens and Vanbeveren (2014) which found that NS mergers could contribute strongly to the galactic r-process but could not account for the first ~ 100 Myr. It is also supported by the GCE models of Côté et al. (2018) which suggest that an extra r-process site could provide r-process enrichment in the early universe. Similarly large scatter in NS mergers was found in van de Voort et al. (2015) while also providing high [r-process/Fe] at low [Fe/H] which we do not find in our simulations. This difference is likely to be caused by their adoption of an empirical r-process yield and a simple power-law DTD, which gives higher rates than our chosen DTD (derived theoretically from binary population synthesis calculations), especially at low metallicity. In our simulations the MRSN model gives much better agreement with observations, but is not a perfect match. There is good agreement in both [Eu/Fe] and [Eu/O] at [Fe/H] $\lesssim 0$, however above this limit it appears to slightly overpredict the amount of Eu produced. The simple combination of these two channels as in Figure 8 did not improve the matching with the observational data. Some metallicity dependence on the rates and/or yields are necessary. The NS merger delay-time we use depends on the metallicity of binary systems. The metallicity dependence on the progenitors of MRSNe has not been investigated in the simulations of the explosions in MRSNe, and is found to be very important in our chemodynamical simulations.

4.5 Conclusions

In this paper, we have presented the results of our chemodynamical simulations including the following r-process chemical enrichment processes: ECSNe, NUW, NS mergers and MRSNe. We present results from both dwarf disc galaxies formed from rotating gas clouds and more complex cosmological zoom-in simulations that form Milky Way-type galaxies. We found that not only [Eu/Fe] but also [Eu/O] ratios are important to constrain the r-process sites. We then predict [Eu/Fe] and [Eu/O] trends as a function of [Fe/H] and compare them to observational data. Our findings can be summarised as follows:

- Neither ECSNe or NUW are able to adequately explain the observed europium levels. This is what we expect based on the yield tables (Fig. 4.1) and is shown in both our dwarf disc galaxies cloud and Milky Way simulations.

- Both NS mergers and MRSNe are able to produce europium in sufficient quantities (i.e. [Eu/Fe] ~ 0 at [Fe/H] ~ 0) when a reasonable parameter is chosen (binary fraction or

MRSNe rate, respectively). Determining which, if either, is dominant requires comparing the predicted trends with observed data.

- Early r-process enrichment is likely a result of MRSNe events. This is suggested by the better match with observational data at low [Fe/H] and also physically motivated: NS events have a delay as they require both the formation of a binary system and for that system to spiral in before europium can be produced in the ejecta. This delay-time depends on the binary population synthesis calculation we used, namely, gravitational kicks at NS formation potentially forcing early mergers and nucleosynthesis. The inclusion of these kicks will be studied in our future works.

- The [Eu/O] ratios can provide more stringent constraints on the r-process sites. As MRSNe are a subset of CCSNe, α elements will be produced with a similar timescale to Eu, resulting in a flatter trend of [Eu/O] ratios. This is not the case for NS mergers. The observational data for [Eu/O] further suggests that MRSNe is the dominant mechanism at [Fe/H] $\lessapprox -1.0$.

- We present a combined model using both NS mergers and MRSNe for chemical enrichment. Even though the contribution from MRSNe was half that used in the solely MRSNe model it sufficient to remove the low [Eu/Fe] and [Eu/O] scatter seen in the NS merger model. However, this combined model overall did not give better fit to observational data than the MRSNe-only model. This suggests that the metallicity dependence of the rates/yields of MRSNe and NS mergers are very important.

We should note that, as discussed in Section 4.4, [X/Fe]–[Fe/H] relations depend on the accretion history of the Milky Way Galaxy. However, it would be difficult to obtain dramatically different [Eu/(O,Fe)]–[Fe/H] relations whilst keeping the [O/Fe] distributions consistent with observations; we find a similar distribution of [O/Fe] ratios in our simulated galaxy to those observed (see Appendix B). We also note that our results depend, to some extent, on the numerical resolutions (see Appendix A) and additional mixing (see Appendix C) in chemodynamical simulations. However, neither of these effects alter our conclusion that NS mergers alone are unable to reproduce the observed [Eu/(O,Fe)]–[Fe/H] relations.

4.6 Appendix

4.6.1 Convergence of Isolated Dwarf Galaxies

We show here the convergence of our simulations for our isolated dwarf disc galaxies. Figure 4.11 shows the mean [Eu/Fe] (upper panel) and standard deviation $\sigma_{[Eu/Fe]}$ (lower panel) for
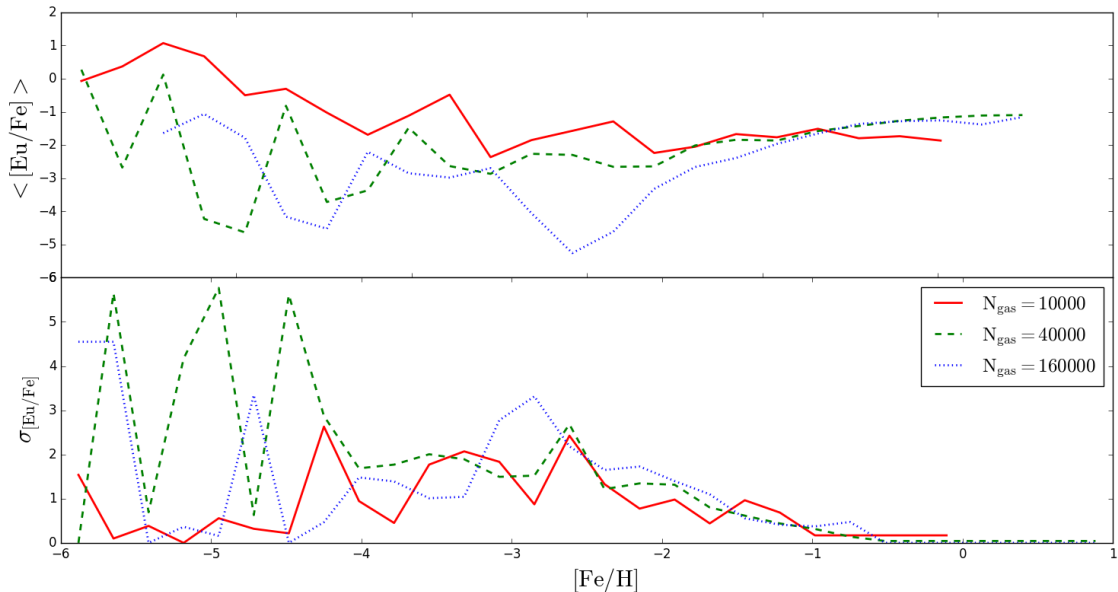
FIGURE 4.11: The upper panel shows the mean [Eu/Fe] as a function of [Fe/H] for three different resolutions: low resolution (10000 particles), medium resolution (40000) and high resolution (160000). The lower panel shows the corresponding standard deviation.

three resolutions: low, medium and high, corresponding to N_{gas} = 10000, 40000 and 160000 gas particles in the initial conditions respectively, with the high resolution being what we use in Section 4.3. All three resolutions are very similar at [Fe/H] ~ -2 and the medium and high resolutions give a very good match at higher metallicity. In the low resolution run there are no very metal rich stars because most of the gas particles have been ejected from the system due to small particle numbers and strong feedback. We note that this effect is not seen in larger galaxies (such as Milky Way type galaxies) due to the substantially greater number of particles and weaker feedback. At [Fe/H] $\lesssim -3$ there is a difference in the mean [Eu/Fe] and $\sigma_{[Eu/Fe]}$ depending on the resolution. This is likely caused by the small number of star particles at low metallicity. We note that these resolution dependencies may be different for the Milky Way simulations shown in Section 4.4 since they have a lower resolution and different initial conditions.

4.6.2 [O/Fe] Bi-modality

The simultaneous agreement both with the observed [Eu/Fe] and [Eu/O] ratios means that we also have good agreement with the observed [O/Fe] ratios. Figure 4.12 shows the [O/Fe]–[Fe/H] relation for the models from Section 4.4. Our prediction is in excellent agreement with the recent non-local thermal equilibrium (NLTE) abundance observations from Zhao et al. (2016) (green triangles) and in very good agreement with the HERMES-GALAH survey (blue contours). The [O/Fe] distribution is similar across all these models and they present a bi-modality at [Fe/H] ~ -1 as in the chemodynamical simulation by Kobayashi and Nakasato (2011, Figure 10) and
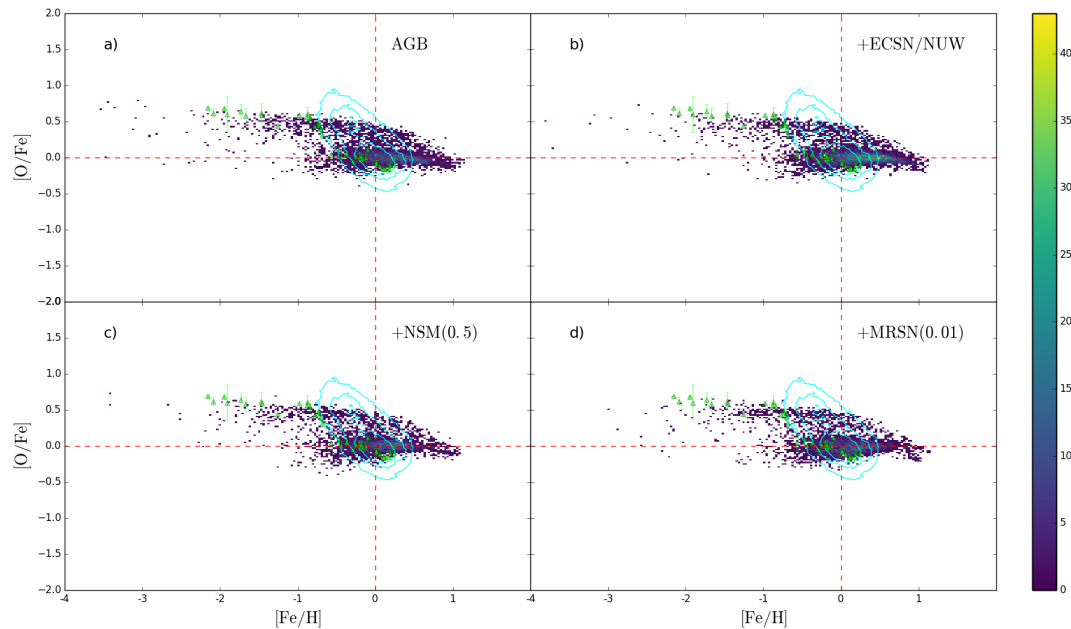
FIGURE 4.12: The same as Figure 4.7 but with [O/Fe] plotted against [Fe/H].

similar to the Ref-L100N1504 simulation galaxies from Mackereth et al. (2018). In particular, Mackereth et al. (2018) suggests that the bi-modality observed in the Milky Way is the result of a gas accretion event early in the galaxies history (and hence that the two trends in the bimodality have different origins). The authors also found that the bi-modality seen in the Milky Way was relatively rare (seen in approximately 5 percent of their galaxy samples). Given that we were able to produce a bimodal [O/Fe] distribution in all of our simulations, this lends support to the Scannapieco et al. (2012) initial conditions used in this paper as a good approximation of the Milky Way. In future work it would be interesting to examine the spatial origin of the stars in each part of our [O/Fe] distribution to determine if they result from a particular merger event. The details including the macroscopic mixing discussed in Mackereth et al. (2018) will be included in future work (Haynes & Kobayashi, in prep.).

4.6.3 Kernel-based mixing

Although we include no explicit sub-grid diffusion (Section 4.2), it is possible to examine an approximation of the effects of diffusion by using the kernel weighting to average the metallicities of nearby particles (Crain et al. 2013). Mackereth et al. (2018) found no difference for their [α/Fe]–[Fe/H] relation with the addition of kernel smoothing. Figure 4.13 shows the [Eu/Fe]–[Fe/H] relation in the NS merger simulation with kernel smoothing (smoothing length of 0.2 kpc, lower panel) and the unsmoothed simulation (upper panel, the same as Figure 7c). We see no significant changes to the [Eu/Fe]–[Fe/H] relation after the kernel smoothing. We also find that this kernel smoothing does not significantly alter the [O/Fe]–[Fe/H] relations, which is in
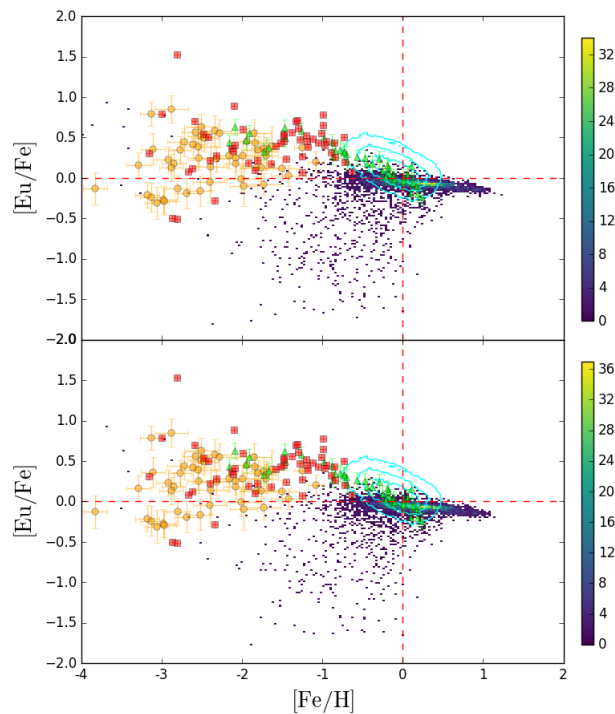
FIGURE 4.13: The same as Figure 7c (upper panel) but compared to the simulation with kernel smoothing (lower panel).

good agreement with observation, and maintains the bi-modality (see Appendix B). It should be noted however that using an increased smoothing length ($\sim$ 1 kpc) can decrease the number of low [Fe/H] stars substantially and the [O/Fe]–[Fe/H] relations become inconsistent with observations.

4.6.4 Initial Conditions

The simulated galaxies in this paper are only able to be compared with Milky Way observational data if the cosmological zoom-in initial conditions used (Scannapieco et al. 2012) form galaxies similar to the Milky Way. The inital conditions are a zoomed in simulation of a halo from the Aquarius Project, chosen due to being an isolated halo with mass similar to the Milky Way. However, Scannapieco et al. (2012) found that simulations based on these conditions varied significantly based on the adopted star formation and feedback models, so the question of the validity of these initial conditions with our code still remains. The behaviour seen here is similar to the model G3-CK in Scannapieco et al. (2012), which uses the same base code (the inclusion of neutron capture processes and updated yields should not make huge differences to the galaxy morphology). The simulated galaxy shows a reasonably similar size and morphology to the Milky Way, with a similar stellar half mass radius, but a greater stellar mass. This holds true with our simulated galaxies which are also overly massive compared to the Milky Way. This is likely a result of inefficient supernova feedback allowing too efficient star formation (though

there is also potential to alter this by changing the star formation efficiency parameter). Although an improved feedback model is likely required, the initial conditions do result in a galaxy similar enough to the Milky Way for comparison. The merger history of the initial conditions is also supported by bi-modality discussion in Section 4.6.2.

Chapter 5

Simulations with Z-dependent Rates of Magneto-rotational Supernovae

This chapter is the latest version of a paper currently being prepared for submission. It builds on what I found in Haynes and Kobayashi (2019); namely that MRSNe likely play an important role in r-process evolution, particularly at early times, and that a combined model of NS mergers and MRSNe should best explain the observed distribution of [Eu/Fe]. To this end, I model the MRSNe rate as metallicity dependent so that it better models the decreasing [Eu/Fe] trend at high [Fe/H] and allows for the addition of NS mergers at the same time.

5.1 Introduction

The production of elements beyond iron is driven by the neutron-capture processes: the s-process and r-process. The s-process requires a slow neutron absorption rate with a timescale significantly longer than that of β decay whereas the r-process is the result of neutron absorption rates that far outstrip the rate of β decay. This results in the different "paths" for s-process and r-process production; as the s-process increases its atomic number along the most stable path, the r-process forms heavy elements by decaying from extremely neutron rich isotopes. As a result of this both the sites and elements produced differ between the two processes.

The primary sites for the s-process are likely in the He-burning shells of low mass AGB stars (main s-process, A>90, see Smith and Lambert 1990 and Bisterzo et al. 2011) and in the cores of massive stars (weak s-process, A$\lesssim$90, see Prantzos et al. 1990, Frischknecht et al. 2016). The primary sites for the r-process are still a matter of active research. They require large neutron fluxes; suggested sites are in the ejecta of neutron star - neutron star (NS-NS) and neutron star - black hole (NS-BH) mergers (e.g., Lattimer and Schramm, 1974; Freiburghaus

et al., 1999b), in the inner layers of rapidly rotating highly magnetised massive stars (magneto-rotational supernovae, MRSNe, e.g., Cameron, 2003), in the O-Ne-Mg cores of electron capture supernovae (ECSNe, e.g., Wanajo et al., 2011) and in neutrino driven winds of NS forming core-collapse supernovae (NUW, e.g., Wanajo et al., 2001).

Previous works have looked at these sources for r-process production using a variety of methods; neutron star mergers in particular have been studied using both stochastic chemical evolutions (Cescutti et al. 2015, Wehmeyer et al. 2015, Ojima et al. 2017) and inhomogeneous hydrody-namic simulations, Shen et al. (2015), van de Voort et al. (2015), Haynes and Kobayashi (2019), hereafter HK19. Given the analysis of the kilonova (Tanaka et al., 2017) resulting from the grav-itational wave detection GW170817 (Abbott et al., 2017b) it is highly likely that NS mergers contribute in some way to the galactic r-process. However, NS mergers have been found to be a poor match with observations at low [Fe/H] as the r-process enrichment starts too late due to the delay for binary formation and coalescence (Mennekens and Vanbeveren, 2014; Wehmeyer et al., 2015). Observations of low metallicity stars have found that the [r-process/Fe] displays a large scatter compared to [α/Fe] at low [Fe/H] suggesting that an early r-process site must be both rare and able to produce significant quantities of r-process material. In order to rectify these problems we need to either modify the models of how NS mergers behave to allow for enrichment at low [Fe/H] or look for this enrichment with alternative or additional r-process sites.

Several solutions have been proposed to explain the NS merger discrepancy: low star formation subhalos may evolve with lower metallicity resulting in a r-process enrichment from NS mergers at lower effective [Fe/H] prior to galaxy assembly (Ojima et al., 2018); Beniamini et al. (2016) suggests that kicks due to supernovae during NS formation, typically assumed to increase the merging timescale of a binary system or otherwise disrupt the binary, may on occasion decrease the time to merge allowing for earlier enrichment.

Alternative r-process sites that can operate at early times are invariably related to core collapse supernovae (CCSNe) as the only site where the energies and neutron densities can be found. Neutrino driven winds and ECSNe, while both classes of CCSNe both contribute weakly to the r-process so are unable to provide a solution. MRSNe represent a potential solution with recent 3D magneto-hydrodynamics simulations suggesting that a full range of r-process elements can be produced and ejected. Being a special case of CCSNe they can also contribute at early times; in particular given that increasing metallicity drives angular momentum and mass loss via solar winds thereby decreasing rotation, MRSNe may play an important role at low [Fe/H] but contribute less with increasing metallicity.

In a previous paper, Haynes and Kobayashi (2019, hereafter HK19), we included the four above processes in chemodynamical simulations and discussed their [Eu/Fe] production in Milky Way-type galaxies. We found that NS-NS / NS-BH mergers and MRSNe were both able to reproduce

[Eu/Fe] levels for high [Fe/H], but that MRSNe were better able to reproduce low [Fe/H] observations. NS mergers were found to be a poor match at low [Fe/H] as r-process enrichment started too late due to the delay for binary formation and coalescence. This is in agreement with chemical evolution models (e.g., Mennekens and Vanbeveren, 2014; Wehmeyer et al., 2015). We also examined a combined model of NS merger and MRSNe; we found that MRSNe could replicate the observed [Eu/Fe] at low [Fe/H] but would overpredict [Eu/Fe] at [Fe/H] > -1.

In this paper we expand upon HK19 by presenting a model for metallicity dependent MRSNe implemented in a chemodynamical hydrodynamics framework including supernova feedback. As we expect hypernovae (HNe) to decrease in frequency with increasing metallicity (Kobayashi and Nakasato 2011) to match expected rates we propose that MRSNe should have some similar metallicity dependence. We combine the yields from this model with those from NS mergers and ECSNe and compare the results with observational data of metal poor stars and from the HERMES-GALAH survey (Buder et al., 2018). In section 2 we discuss our code and models. In section 3 we present the results of Milky Way-type galaxies with r-process chemical enrichment and compare the abundance ratios for a variety of elements. We discuss these results in section 4 and briefly summarise in section 5.

5.2   Code and Yields

Our code is based on the smooth particle hydrodynamics (SPH) code GADGET-3 (see Springel 2005 for the previous version GADGET-2) with the inclusion of relevant baryon physics (e.g. UBV heating, metallicity dependent radiative cooling, star formation and thermal supernova feedback, see Kobayashi 2004, Kobayashi et al. 2007a). Chemical enrichment is accounted for using calculated yields for type II (SNII) and HNe, type Ia (SNIa) SNe, AGB stars, NS mergers and ECSNe (see HK19 and the references therein for a fuller description). Note that we do not include an explicit sub-grid diffusion model for metals between gas particles. Although this could have an effect on [X/Fe] we do not think the effects should be significant. We approximate this effect by kernel weighting (Crain et al., 2013) in section 4.6.3.

We use the yield tables presented in Nishimura et al. (2015) for a 25 $M_\odot$ star (B11β1.00 model) for our MRSNe. The expected number of MRSNe is poorly constrained and in HK19 we found that while MRSNe were a good alternative to explain [Eu/Fe] at low [Fe/H] it resulted in a poor fit at high [Fe/H]. Given that we also expect NS mergers to contribute to some extent to the galactic r-process we suggest that MRSNe have some form of metallicity dependence. Given that increased metallicity drives mass loss (and hence angular momentum loss) via solar winds it is more likely for low metallicity stars to meet the conditions required for MRSNe. This is similar to what we expect from our HNe yields, so we assume the same metallicity dependence by converting a fraction of the HNe fraction, f_{HNe}, into MRSNe. We choose a value of 3%

	10 kpc disc					Solar Neighbourhood			
Simulation	M_{gas}	M_*	f_*	SFR	Effective SN	M_{gas}	M_*	f_*	SFR
	10^9 $M_\odot$			$M_\odot$ y^{-1}	kpc	10^9 $M_\odot$			$M_\odot$ y^{-1}
Control	10.57	97.19	0.90	40.12	5.688 - 7.438	1.54	4.13	0.73	4.78
NSM(0.5)	10.78	97.20	0.90	43.03	6.500 - 8.500	2.23	3.55	0.61	7.70
MRSN(0.03)	10.61	102.18	0.91	37.62	5.454 - 7.132	2.05	5.94	0.74	7.07
N + M + E	10.73	99.64	0.90	47.19	6.760 - 8.840	1.73	2.97	0.63	4.00

TABLE 5.1: The properties for the simulated galaxies at $z = 0$. All masses are given in terms of 10^9 $M_\odot$ and SFR is given in $M_\odot$ y^{-1}. Values in the first half of the table are given for a central 10 kpc disc with height $\pm$ 2 kpc. Values in the second half correspond to the particles within the effective solar neighbourhood as given.

across all metallicities based on Kobayashi (2019, in prep). This gives the MRSNe fraction, f_{MRSN} = 0.0003, 0.0003, 0.0069, 0.012, 0.015, and 0.015 for Z = 0.05, 0.02, 0.008, 0.004, 0.001, and 0.0 respectively. As before we assume that the MRSNe fraction reduces the available HNe fraction, so we reduce f_{HNe} accordingly (to f_{HNe} = 0.0097, 0.0097, 0.2231, 0.388, 0.485, and 0.485 for the above Z). These values are interpolated as Z lies in between the stated values but is not extrapolated and instead adopts the appropriate upper or lower limit.

We use cosmological zoom-in initial conditions to form a galaxy with similar morphology and size to the Milky Way. The conditions we choose for this are from the Aquila comparison project (see Scannapieco et al., 2012) and have the cosmological parameters H_0 = 100h = 73 km s^{-1} Mpc^{-1}, $\Omega_0 = 0.25$, $\Omega_\Lambda = 0.75$, $\Omega_B = 0.04$.

5.3   Milky Way Abundance Patterns

In this section we present the abundance patterns for a number of elements, including europium, neodymium, zirconium, barium for four simulation models. We run a control model that includes no additional r-process beyond what can be produced in CCSNe and low mass AGB stars. We show two models that include a single additional r-process, NS mergers (with f_{NSM} = 0.5 as in HK19) and Z-dependent MRSNe (as described in section 2). Both of these process are added in addition to type II SNe and AGB yields. Finally we show a model including NS mergers, Z-dependent MRSNe (ZMRSN) and ECSNe (as well as type II SNe and AGB yields) as our best fit to observed abundance patterns. As simulations do not produce galaxies identical to the Milky Way, in order for us to compare these galaxies to observations we define an "effective solar neighbourhood" within them by scaling the solar neighbourhood range (a 6.5 - 8.5 kpc ring) to the size of the galaxy as in HK19. This region extends to a height of 1 kpc above and below the plane of the disc. Basic galactic properties are listed in table 1 for a central 10 kpc radius ($\pm$2 kpc height) and for the calculated effective solar neighbourhood.
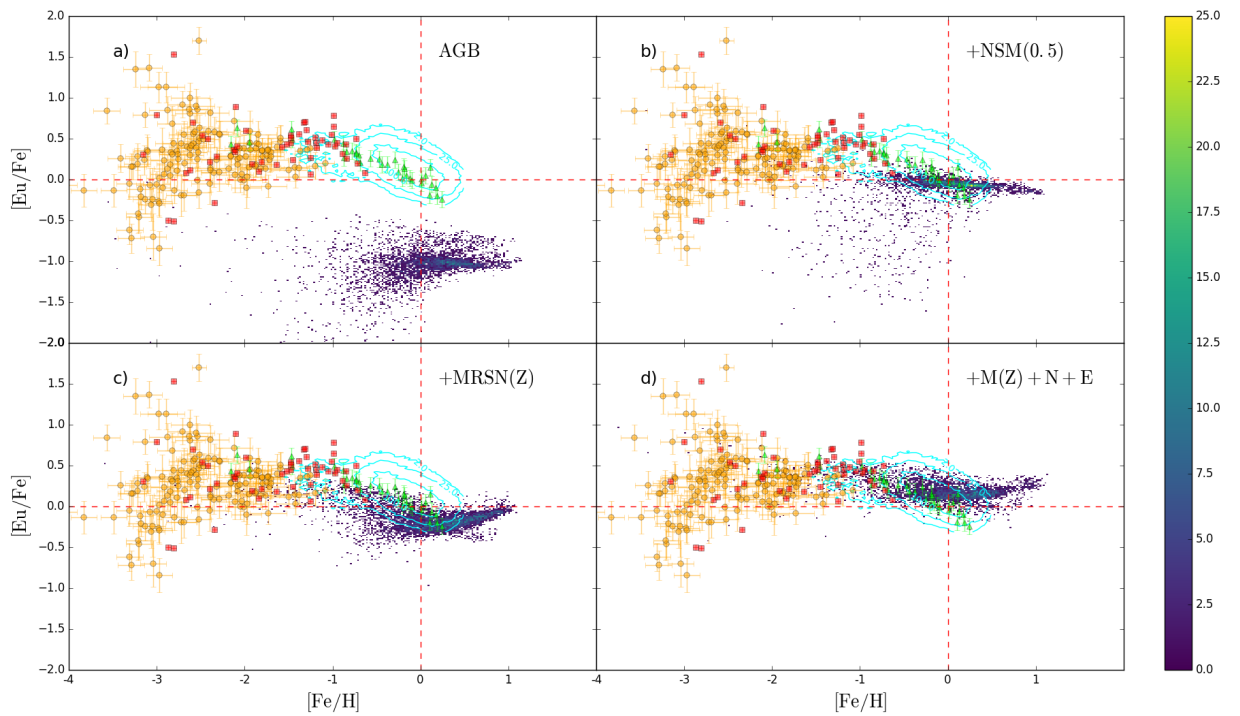
FIGURE 5.1: Figure showing the [Eu/Fe] - [Fe/H] relation for the effective solar neighbourhood stars. Panel a) shows our control simulation. Panels b) and c) show the NS merger and MRSNe models respectively. Panel d) shows the combined model of NS mergers, MRSNe and ECSNe. Observational data is taken from Hansen et al. (2016) (red squares), Roederer et al. (2014) (orange circles), Zhao et al. (2016) (green triangles) and the HERMES-GALAH data set from Buder et al. (2018) (blue contours).
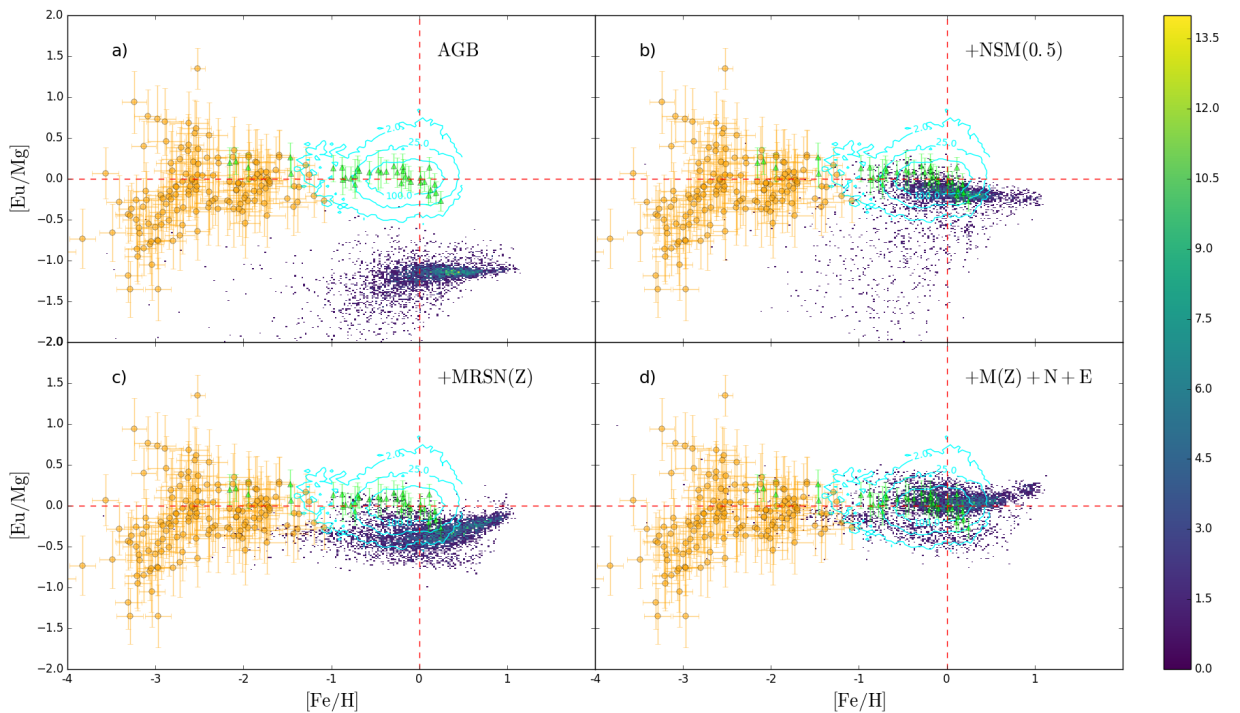
FIGURE 5.2: As figure 5.1 but showing the [Eu/Mg] - [Fe/H] relation.
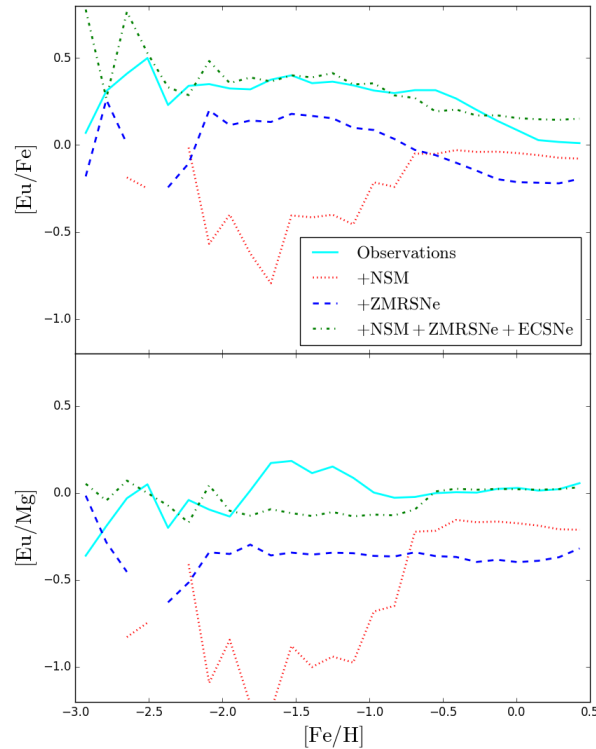
FIGURE 5.3: Median [Eu/Fe] (upper panel) and [Eu/Mg] lower panel for the NS merger, ZMRSN and combined models. The solid cyan line shows the median of all combined data sets.

The observational data we use comes from four different sources: Hansen et al. (2016) (red squares), Roederer et al. (2014) (orange circles), Zhao et al. (2016) (green triangles) and the HERMES-GALAH data set from Buder et al. (2018) (blue contours). The HERMES-GALAH data is shown as contours so as to not obscure the data beneath. Contours are for 2, 25 and 100 points per 0.038 width, 0.02 height bin with spline interpolation of order 1 between the initial points for ease of plotting.

5.3.1   r-process - Eu, Nd, Dy, Yb

Figure 5.1 shows the [Eu/Fe] - [Fe/H] relation for our four galaxy models. Panel a) shows the control model. Panels b) and c) show the addition of NS mergers and ZMRSN respectively. Panel d) shows the combined model with the inclusion of NS mergers, ZMRSN and ECSNe. As we demonstrated in HK19, AGB stars and NS mergers are a poor fit for the galactic [Eu/Fe] trend, particularly at [Fe/H] < -1, where the NS merger delay time for both formation and coalescence leads to lower [Eu/Fe]. The control model has [Eu/Fe] -1 and [Fe/H] = 0 and NS merger model has a significant scatter in [Eu/Fe] in the range $-2 <$ [Fe/H] < 0. ZMRSN provide a better fit than the MRSNe model with a flat parameter at [Fe/H] < -1. The [Eu/Fe] pattern sits below the observed values at [Fe/H] ~ 0, this is to be expected as the fraction for ZMRSN
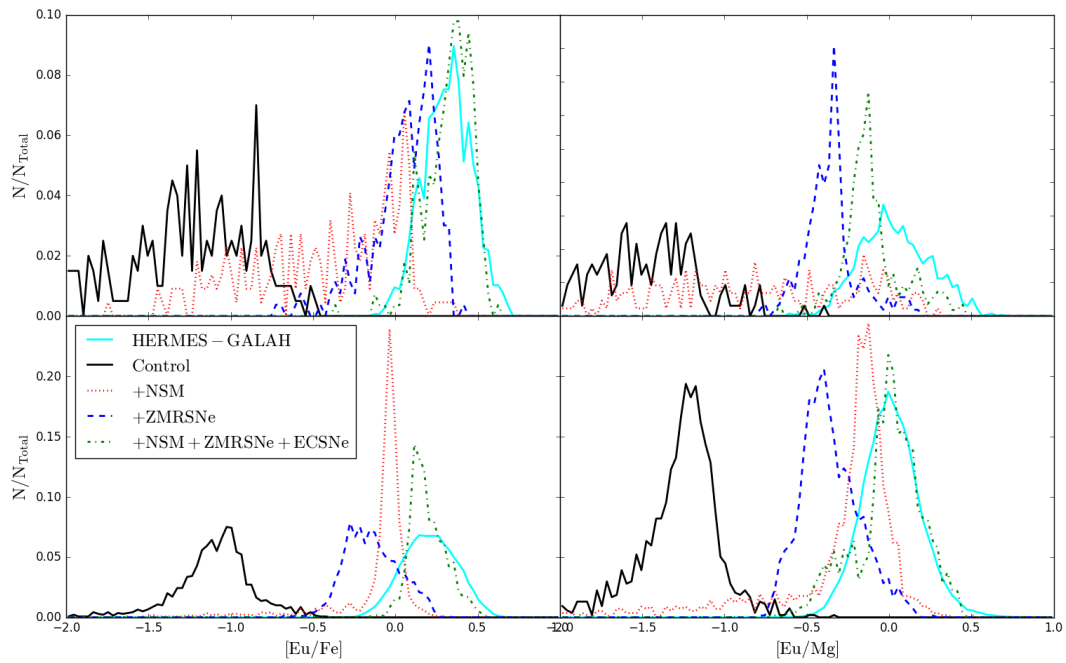
FIGURE 5.4: [Eu/Fe] and [Eu/Mg] distributions in the range −1.5 < [Fe/H] < −0.75 (upper panels) and −0.75 < [Fe/H] < 0.5 (lower panels) for the control, NS merger, ZMRSN and combined models. For each range, the left hand panel shows the [Eu/Fe] distribution and the right hand panel shows [Eu/Mg]. The solid cyan line shows the distribution for the HERMES-GALAH data in the same ranges.
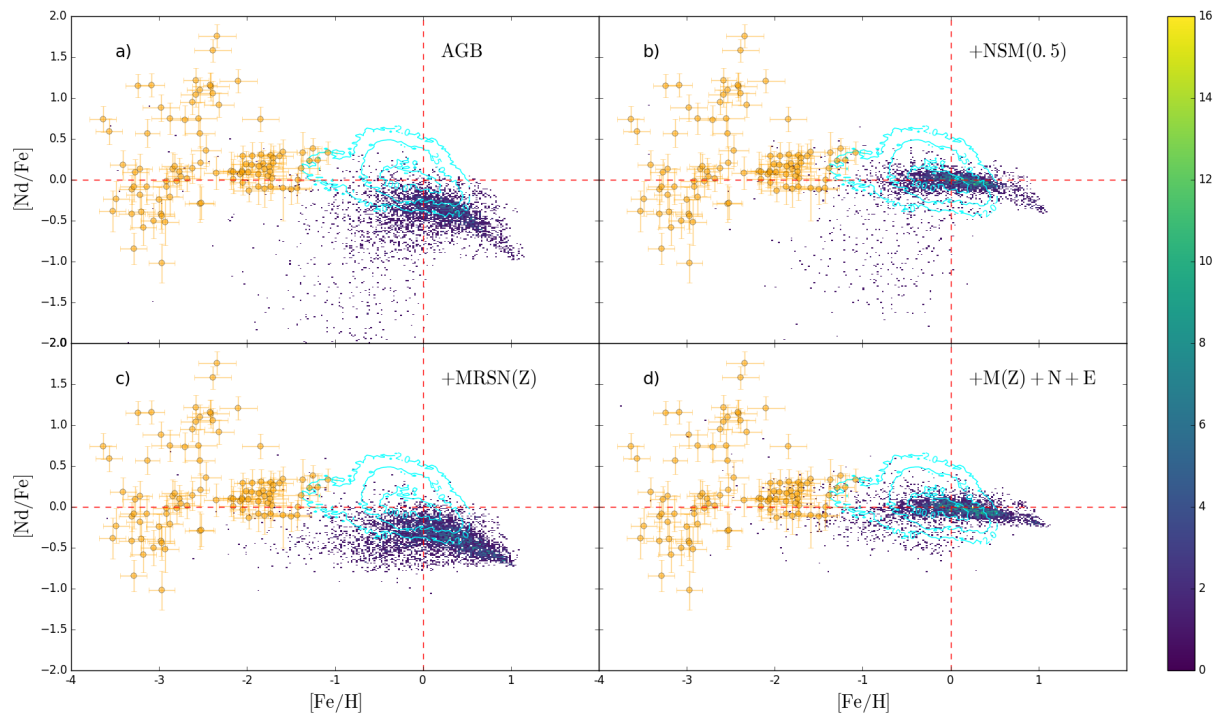
FIGURE 5.5: As figure 5.1 but showing the [Nd/Fe] - [Fe/H] relation.

drops to 0.0003 at high metallicity. This does allow for additional processes to be included however; by combining this model with NS mergers we have an excellent fit with observation for [Fe/H] < –1 and a reasonable fit for –1 < [Fe/H] < 0.5. We are unable to replicate entirely the slight downward trend observed at [Fe/H] > –1, though we do see a shallow downward trend in the NS merger model. Observational data for the evolution of [Eu/α] typically shows a flat trend with increasing [Fe/H]. This can be seen in Figure 5.2 which shows the [Eu/Mg] – [Fe/H] relation. Comparisons to alpha elements rather than Fe provide insight into the formation sites. Whereas [X/Fe] is driven at high [Fe/H] by large Fe production from Type Ia SNe, Mg is primarily produced in CCSNe so [Eu/Mg] should be driven down by CCSNe. Clearly this is not the case for the observed flat [Eu/Mg] trend (although it still displays high scatter at [Fe/H] < –1.5, consistent with a strong, rare Eu production site), suggesting that the Mg production occurs at similar rates as Eu production, relative to solar [Eu/Mg]. This matches with MRSNe as a rare subset of HNe, explaining both the flatness and scatter at low metallicity. In Figure 5.2 our ZMRSN model shows a relatively flat trend at [Fe/H] < –1 but underpredicts [Eu/Mg] at solar [Fe/H]. This is improved by the inclusion of NS mergers and ECSNe which provide excellent agreement with observations for –4 < [Fe/H] < 0.5. Figure 5.3 shows the median [Eu/Fe] and [Eu/Mg] (upper and lower panels respectively) binned in 0.14 [Fe/H] intervals. The cyan observational data takes the median for each bin across all data sources (as such HERMES-GALAH will dominate in the range [Fe/H] > –1.5 due to volume of data). The observed [Eu/Fe] and [Eu/Mg] trends are closely matched by the combined ZMRSN, NS merger and ECSNe model in both cases. The ZMRSN model alone arguably provides a better fit to the trend but offset by $\sim$ –0.5, and could possibly be a good fit with increased f_{MRSN}. However, as f_{MRSN} depends directly on [Fe/H] for the ZMRSN model, the evolution of the [Eu/Fe] trend is not so simple and more constraints on the fraction of stars with appropriate rotation and magnetic fields is probably required. In Figure 5.4 we compare the [Eu/Fe] and [Eu/Mg] abundance distributions for narrow [Fe/H] slices within the HERMES-GALAH range. The upper panels show the [Eu/Fe] and [Eu/Mg] (left and right respectively) distributions in the range –1.5 < [Fe/H] < –0.75 and the lower panels show the [Eu/Fe] and [Eu/Mg] distributions in the range –0.75 < [Fe/H] < 0.5. In the range –1.5 < [Fe/H] < -0.75 both the [Eu/Fe] and [Eu/Mg] distributions match the observations best with the combined model. The [Eu/Mg] peak is positioned at slightly lower [Fe/H] and is rather less spread out than observed, however this spread may be increased in reality by metal mixing. Similarly, both [Eu/Fe] and [Eu/Mg] are good matches in the –0.75 < [Fe/H] < 0.5 range with the [Eu/Fe] peak showing slightly less scatter than expected.

Figure 5.5 shows the [Nd/Fe] – [Fe/H] relation, with panel layout as in Figure 5.1. Nd is expected to be produced in both s-process and r-process sites; this can be seen in panel a) which shows a closer match to observations with the inclusion of AGB yields as the main s-process site. The inclusion of NS mergers gives a good match to observational data at solar [Nd/Fe] and [Fe/H], however a large scatter still exists at –2 < [Fe/H] < 0 as NS mergers are unable to
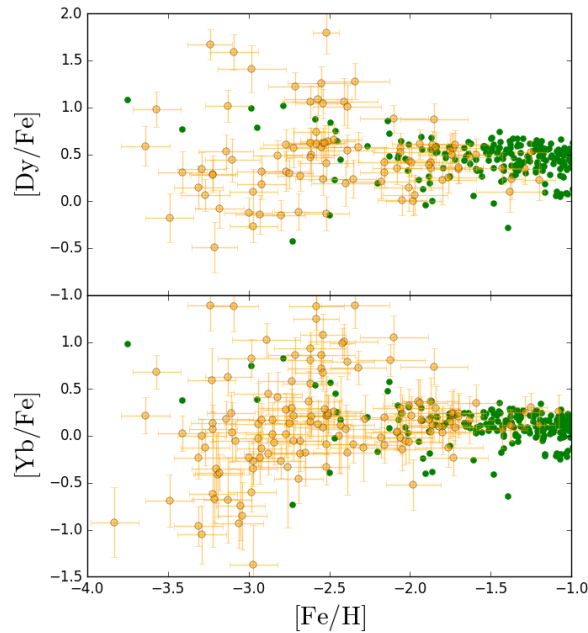
FIGURE 5.6: Abundance relation for [Dy/Fe] (upper panel) and [Yb/Fe] (lower panel) for –4
< [Fe/H] < –1. The orange data points are from Roederer et al. (2014), which was the only of
our four data sets with measurements for Dy and Yb. The green points show our simulated star
particles.

produce Nd quickly enough to raise [Nd/Fe]. The ZMRSN model matches the trend quite well
but [Nd/Fe] is consistently offset below observations by ~ 0.5. The combined model provides
the best fit at [Fe/H] > –2. It also reproduces the large scatter at [Fe/H] < –2 for [Nd/Fe] > 0,
however it does not match the observed scatter as well at [Nd/Fe] < 0. Additionally in Figure
5.6 we show low metallicity end of the abundance patterns for both [Dy/Fe] and [Yb/Fe]. Dy
is an almost entirely r-process element and Yb can be formed by both the s-process and the
r-process, similar to Nd. The upper panel shows [Dy/Fe] for the combined model and the low
panel shows [Yb/Fe] both in range –4 < [Fe/H] < –1. Both show a good match in trend and
scatter with the observational data.

5.3.2   s-process - Zr, Ba

Zr is a light s-process element and so expected to be produced by both the main and weak s-
processes in AGB stars and in the He burning shells of massive stars, with a small contribution
from the r-process. We show the [Zr/Fe] - [Fe/H] relation in Figure 5.7. Compared to the heavier
elements Zr has a higher [Zr/Fe] values ($\sim$ –0.25) at solar [Fe/H] in the control model due to
Zr production in AGB stars. As with the previous abundances we have examined this model
results in a high scatter in the range –2 < [Fe/H] < 0 which is inconsistent with observations.
The inclusion of NS mergers increases the values of [Zr/Fe] slightly to solar values at [Fe/H]
~ 0 but does not remove the large scatter. Conversely, the inclusion of ZMRSN removes the
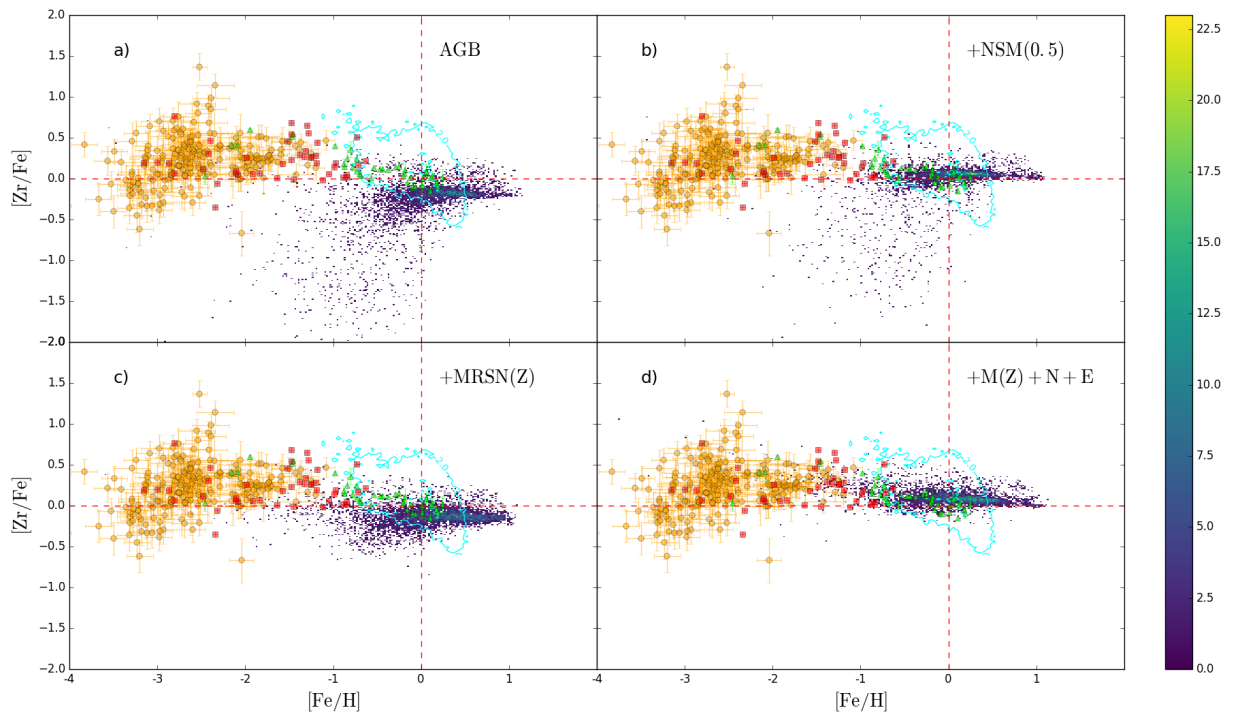
FIGURE 5.7: As figure 5.1 but showing the [Zr/Fe] - [Fe/H] relation.
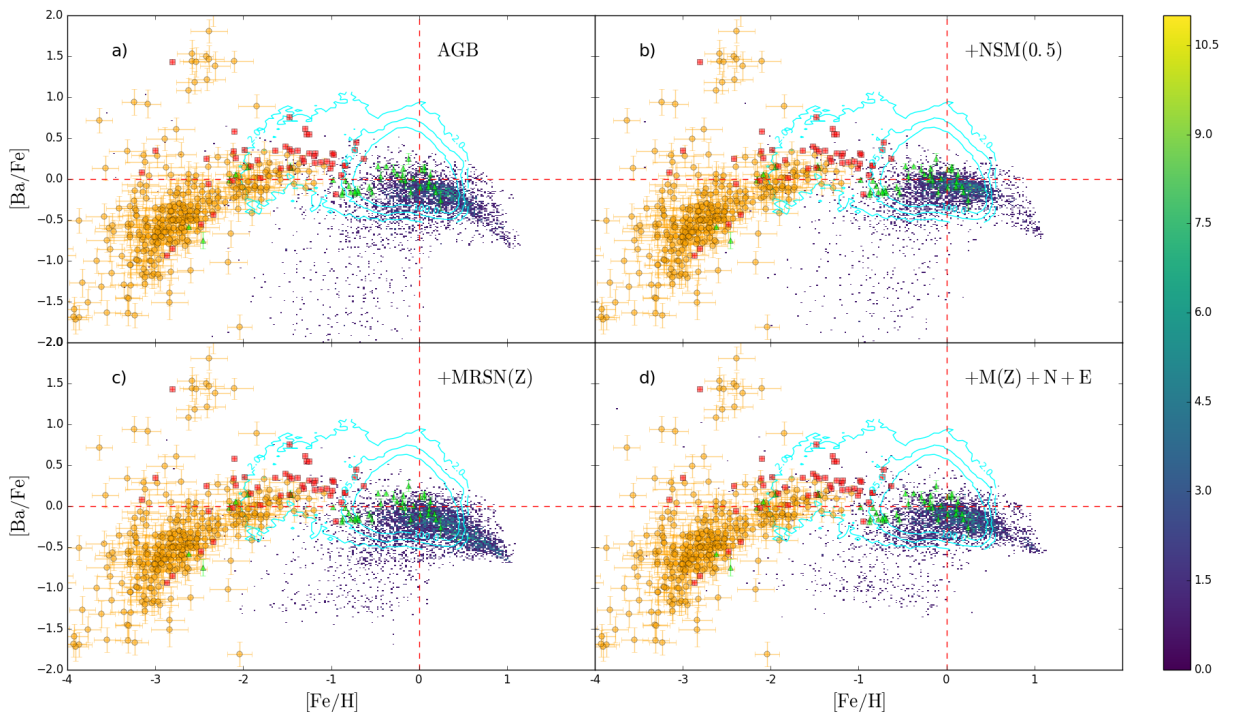
FIGURE 5.8: As figure 5.1 but showing the [Ba/Fe] - [Fe/H] relation.

scatter but leaves [Zr/Fe] < 0, suggesting that the scatter is built up from relatively early AGB enrichment. The combined model with both additions (also ECSNe which we expect to make reasonable contributions up to the second s-process peak) matches observations very well for [Fe/H] < 0, but overpredicts [Zr/Fe] at higher [Fe/H] where we should see a downward rather than flat trend.

Finally in Figure 5.8 we show the [Ba/Fe] – [Fe/H] relation. As a heavy s-process element we expect Ba to be produced largely by AGB stars. The control model shows [Ba/Fe] levels of ∼ –0.25 at [Fe/H] = 0, slightly below observed levels. It also shows a large scatter below [Ba/Fe] = –0.5 in the –2 < [Fe/H] < 0 range which is inconsistent with observations; neither does it reproduce the observed trend at [Fe/H] < –2. Unsurprisingly, the addition of NS mergers or ZMRSN does not change the simulated data significantly, either independently or together with ECSNe. The addition of ZMRSN does have a small effect on the anomalous scatter at –2 < [Fe/H] < 0; as ZMRSN are primarily operating at low [Fe/H] this suggests that altering this feature requires changes at low [Fe/H]. Overall, our [Ba/Fe] abundance patterns are a poor match with observations.

5.4 Discussion

In the previous section we showed two results which we discuss further here. We show that our ZMRSN model is able to reproduce excellently abundance patterns for Eu, Nd, Dy and Yb for [Fe/H] < 0. The fit is better when NS mergers are also included, contributing at higher [Fe/H], but the overall fit with just NS mergers is poor. However, there is no direct observational evidence for MRSNe, a fact which is compounded by the notion that they are less likely to occur in present day galaxies with higher [Fe/H]. The question that therefore remains: is it possible to reproduce the observed trends by modifying NS merger models? Part of this question hinges on the uncertainty in the NS merger rate - better constraints on this will help to determine if additional processes are required and how much they should contribute to the galactic r-process. Nonetheless DTD models can be used to estimate NS merger rates and combined with nucleosynthesis yields can constrain required rates to explain abundance patterns. A common problem is the difficulty in explaining the decreasing [r-process/Fe] trend at high metallicity using the expected t^{-1} DTD, which gives a trend much flatter than expected. Beniamini and Piran (2019) showed that in one zone calculations, assuming no delay between formation and merging of binary systems could reproduce this downward trend in [Eu/Fe], however it did not appear to explain the scatter at [Fe/H] < –1. The minimum delay time adopted for the DTD model seems to have a large impact on the [Eu/Fe] trend even at [Fe/H] > –1.5 (see Appendix A of Côté et al. 2018), with shorter delay times resulting in greater [Eu/Fe] enrichment at low [Fe/H]. The DTD we use (Mennekens and Vanbeveren, 2014) has a low minimum delay (∼

10 Myr) and a further reduction is unlikely to reproduce the solar [Fe/H] downward trend or increase [Eu/Fe] at [Fe/H] < -1. In order to reproduce the downward trend either a) a steeper DTD must be adopted or b) strong Eu production must take place at low [Fe/H] with a stronger downward trend than NS mergers across the same [Fe/H] range. Given that our choice for f_{MRSN} drops to almost zero for $Z > 0.02$ and gives a good match to observations across a range of r-process elements for low Z stars it seems likely that a steeper DTD is required.

Additionally, we find that our SFR is too high at late times. This may contribute slightly to the excess of metal produced however as noted in HK19 we find that our [α/Fe] - [Fe/H] relation is a good match with observations and that the overly high SFR late at late times likely only results in the formation of some very super-solar metallicity stars. Nonetheless, in a future work we intend to examine the effect of using various SNe feedback models to supress SFR on chemical enrichment.

In Figure 5.8 we showed the [Ba/Fe] – [Fe/H] relation. The observed increasing trend of [Ba/Fe] from [Fe/H] ~ -3 suggests that Ba production needs to start post Fe enrichment from early CCSNe. AGB stars fit this model, but the increase is shifted to higher [Fe/H], so the AGB contribution comes too late. Given the long lived nature of the low mass stars (M < 3 $M_\odot$) required, it is difficult to shift the onset of Ba production to earlier times. One possible solution is in the cores of massive stars which typically can only produce a weak s-process. However, recently it has been suggested that mixing induced by sufficiently rapid rotation in these stars can provide additional neutron sources, particularly at low metallicity, resulting in an increase in s-process production and shift to heavier s-process elements (Chiappini et al., 2011; Cescutti et al., 2015; Frischknecht et al., 2016). Inclusion of yields from these spin stars could provide additional Ba at low [Fe/H] and could better reproduce observations.

5.5 Conclusions

In section 5.3 we presented the abundance relations for Eu, Nd, Dy, Yb, Zr and Ba for four model galaxies including a number of r-process sites. In particular we present a combined model of NS mergers, Z-dependent MRSNe and ECSNe as our best match to observational data. In section 5.4 we provided some additional discussion. Figures 5.1, 5.5 and 5.6 showed that [Eu/Fe], [Nd/Fe], [Dy/Fe] and [Yb/Fe] are an excellent match in both average abundance and scatter in the $-3 <$ [Fe/H] < -1 range. Between $-1 <$ [Fe/H] < 0 the observational data suggests a downward trend for [Eu/Fe] (HERMES-GALAH and Zhao et al. 2016) and to a lesser extent [Nd/Fe]. The combined model shows a slightly flatter trend than this suggesting that our model is overproducing europium in high [Fe/H] stars. We suggest that this could be remedied by the choice of DTD for NS mergers, something which requires further study. We propose that only a combined model of Z-dependent MRSNe and NS mergers is able to explain both the low

[Fe/H], high scatter [r-process/Fe] trend and the decreasing trend at solar [Fe/H]. We also found that the [Ba/Fe] increase occurred at too high [Fe/H]. We suggest that this points to the inclusion of an additional s-process in rapidly rotating massive stars in the early universe.

Chapter 6

The Effects of Feedback Model on Chemical Enrichment

In this chapter I will discuss the effects of feedback model choice on chemical enrichment. This forms the basis for a third paper, although more work is needed before it is ready for submission.

6.1 Introduction

Supernova feedback is a crucial mechanism in the evolution of galaxies. The deaths of stars release large quantities of metals and energy into their surroundings influencing the formation of the next stars. In particular energy feedback from supernovae (SNe) is an important mechanism in preventing excessive star formation by injecting heat and momentum into the surrounding gas. Additionally SNe feedback can drive outflows of metal enriched gas into the intergalactic medium (IGM).

Historically cosmological and numerical simulations have resulted in star formation rates (SFRs) somewhat in excess of observations and have had difficulty in suppressing this. This difficulty arises due to the fact that simulations often have mass resolutions in excess of thousands of solar masses and as such are unable to resolve supernova remnants. The simple case of distributing the energy from a SN event into the ISM as heat proves ineffective as the energy is free to be radiated away with little effect on star formation.

Various models have tried to rectify this issue. Some models simply turn off cooling in the affected gas particles for a short time (see Stinson et al. 2006, Teyssier et al. 2013) to maintain the heating effect, thereby preventing star formation and driving thermal outflow. Dalla Vecchia and Schaye (2012) used a stochastic approach where larger amounts of energy are assigned to fewer gas particle (see Crain et al. 2015 for application in the EAGLE simulations). The stronger

heating of particles allows SFR suppression prior to cooling occuring. Kinetic models (such as Dalla Vecchia and Schaye 2008, Navarro and White 1993) assign a fraction of the SN energy to be distributed as a velocity kick instead of as thermal energy in order to reduce gas density required for star formation. It should be noted here that Kobayashi (2005) found that a similar model of kinetic feedback gave metallicity gradients that too shallow to match observations as a result of metal rich gases being driven from the core. Similar mechanical models distribute some energy as momentum and additionally try to account for any unresolved Sedov-Taylor phase of SNe expansion (Hopkins et al., 2014).

In this paper we examine the effect of four different feedback models: the standard thermal model, a kinetic fraction model, a version of the stochastic model as in Dalla Vecchia and Schaye (2012) and a version of the mechanical model as in Hopkins et al. (2014).

6.2   Models and Parameters

The code used is the same as in the previous works Kobayashi et al. (2007a) and chapters 4 and 5 and includes the same physical processes (radiative cooling, UVB heating, star formation, etc.). The hydrodynamics is based on the SPH code GADGET-3 (see Springel 2005 for the similar GADGET-2). The chemical enrichment for type Ia and type II SNe, HNe, SW and the contribution from AGB stars is the same as in Haynes and Kobayashi (2019) (note yields from the r-process sites, NS mergers, MRSNe, ECSNe and neutrino winds, are not included). In order to examine the effect on galactic wind we compare four feedback models. The thermal model is the default feedback method and the same as used in the works above. The kinetic, stochastic and mechanical models all introduce free parameters which will be discussed below in the context of isolated dwarf galaxies. These simulations are much faster than Milky Way simulations so provide good testing environments for both code and parameters.

6.2.1   Kinetic Feedback

Kinetic feedback uses a parameter f_k that represents the fraction of energy from a SNe event that is distributed as kinetic energy. It therefore sits somewhere between 0 and 1, with 0 being indistinguishable from the thermal model and 1 having zero thermal energy distributed. The kinetic energy fraction is converted to a velocity which is applied as a kick to the gas particle directly away from the SNe event. The conversion of thermal energy takes place after the energy weighting due to the smoothing kernel is calculated. As one of the primary drivers of non thermal feedback is to prevent excessive star formation, Figure 6.1 shows the SFR for three different kinetic parameters: 0.01, 0.05 and 0.1 (dashed lines), in addition to the default thermal model (solid black line). For $f_k = 0.01$, the model closely matches the thermal model. Beyond
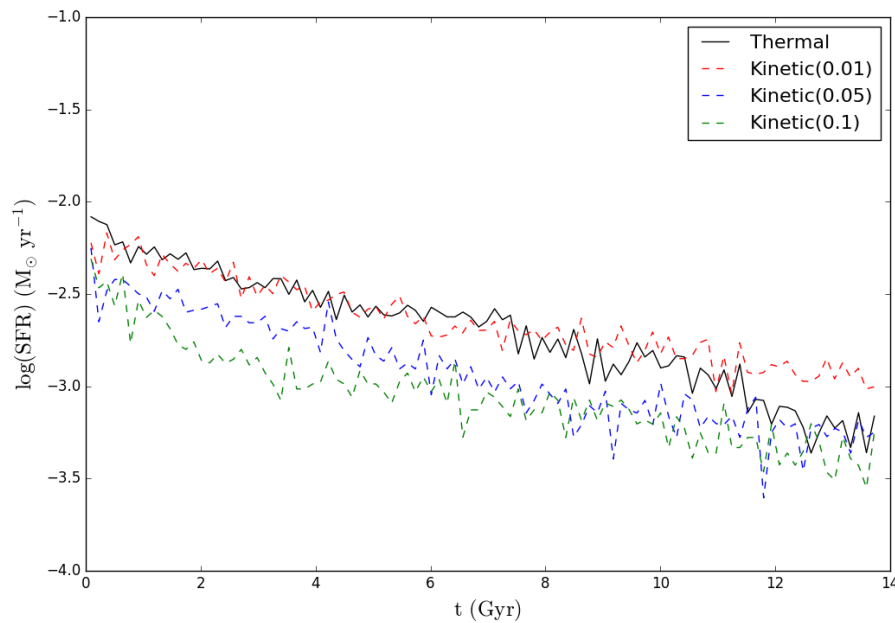
FIGURE 6.1: The SFR in isolated dwarf galaxies for the thermal model (solid black line) and three kinetic parameters (dashed lines).

that a clear trend is visible; increasing f_k decreases SFR. Note that increasing it beyond ~ 0.25 causes some problems with simulation runs not completing. This has been a recurring problem with kinetic feedback when using high values for f_k and may be related to gas particles becomes spread over too large an area. Prior to this value it is possible for kinetic feedback to dismantle the gas disc entirely. We found $f_k = 0.1$ to be optimal for isolated dwarf galaxies.

6.2.2 Stochastic Feedback

The stochastic feedback model is based on the feedback model presented in Dalla Vecchia and Schaye (2012). As in Dalla Vecchia and Schaye (2012) we define an energy increase, Δ_e, which is used to heat the neighbour particles around the SNe event. We choose

$$\Delta_e = f \frac{E_{SN}}{N_{ngb}}, \tag{6.1}$$

where E_{SN} is the SNe energy from the star particle during a given timestep and N_{ngb} is the number of feedback neighbour particles. At the point of feedback, a random number is generated for each of the neighbour particles and compared to

$$r < \frac{E_{SN} M_*}{\Delta_e \sum_i^{N_{ngb}} M_i}, \tag{6.2}$$
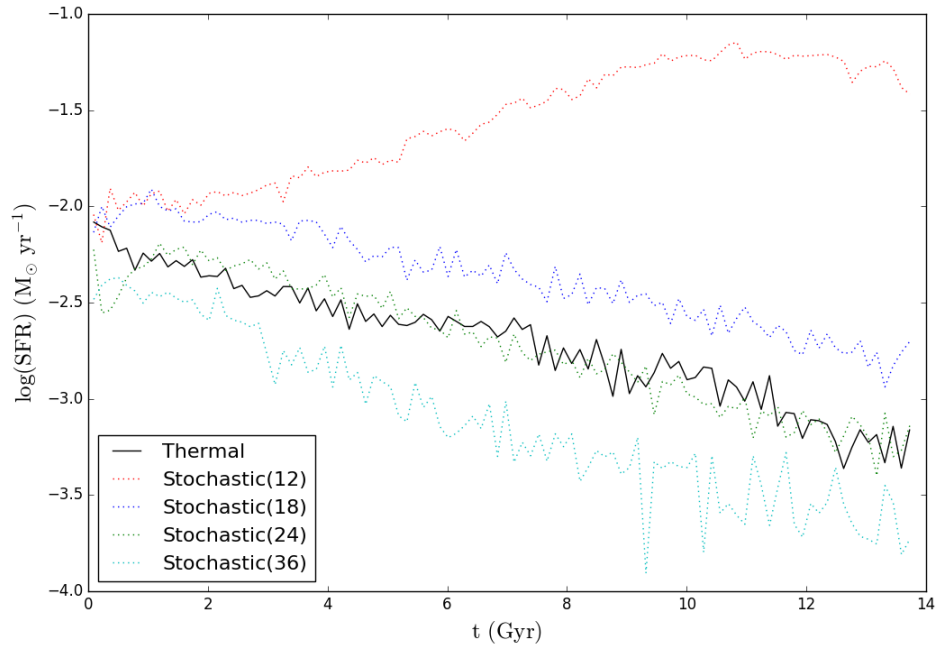
FIGURE 6.2: The SFR in isolated dwarf galaxies for the thermal model (solid black line) and five stochastic parameters (dashed lines).

where M_* is the mass of the star particle. We note that our value of Δ_e scales with the available SNe energy for a given timestep. The parameter we introduce, f, is simply a scaling factor for the approximate minimum energy for the probability function to hold,

$$\Delta_e > \frac{E_{SN}}{N_{ngb}}, \tag{6.3}$$

which gives a probability of 1 (i.e. each particle will receive an energy increase of Δ_e). Substituting $f = E_{SN} / N_{ngb}$ into the probability function gives the probability of any given particle receiving an energy increase, which will scale as the reciprocal of f and give the expected number of particles that receive the energy

$$N_{FB} = \frac{N_{ngb}}{f}. \tag{6.4}$$

Given the choice of $N_{ngb} = 36 \pm 2$, we choose values of $f = 12, 18, 24,$ and 36. The results of these simulations are shown in Figure 6.2 as dotted lines and again compared with thermal (solid black line). Using $f = 24$ gave a SFR very similar to the thermal model. The lower parameter choices (12 and 18) resulted in higher SFRs. Using $f = 36$ results in each SNe event heating on average one gas particle and gave a suppressed SFR. We want to avoid using $f > N_{NGB}$ as it resulted in an expectation value of less than 1 (although it is still possible that no particles are heated even with lower values of f) and additionally represents a greater increase in energy than the SNe event can produce (although this is again possible for any given SNe event and choice
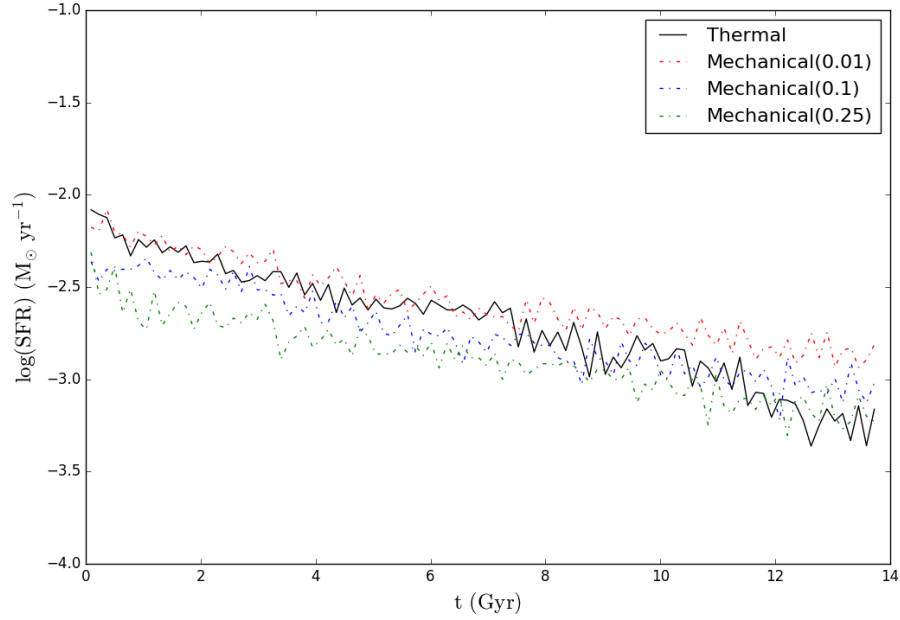
FIGURE 6.3: The SFR in isolated dwarf galaxies for the thermal model (solid black line) and three mechanical parameters (dot-dashed lines).

of f, if $f > N_{\text{NGB}}$ then any energy feedback that occurs will violate this). Additionally, feedback to a single particle corresponds to the fiducial energy increase used in Dalla Vecchia and Schaye (2012).

6.2.3 Mechanical Feedback

Mechanical feedback is based on the work in Hopkins et al. (2014) and Smith et al. (2018) and attempts to take into account the work done by the SNe shock wave during the Sedov-Taylor phase of expansion. Similar to the kinetic model a fraction of SNe energy, f_{k}, is converted to a momentum kick. As in Smith et al. (2018) the momentum is boosted by

$$\Delta P = \Delta P_0 \times \sqrt{1 + \frac{M_{\text{i}}}{M_{\text{ej}} W_{\text{i}}}}, \tag{6.5}$$

where ΔP_0 is the momentum initially input into the gas, M_{i} is the mass of the ith particle and $M_{\text{ej}} W_{\text{i}}$ is mass received by the ith particle. This is limited by the total momentum at the point where the shock wave exits the Sedov-Taylor phase,

$$\Delta P = \Delta P_0 \times 3 \times 10^{10} \left(\frac{Z}{Z_{\odot}} \right)^{-0.14} \frac{E_{\text{SN}}^{16/17} n_{\text{H}}^{-2/17}}{\sqrt{2 M_{\text{ej}} E_{\text{SN}}} 10^{51}} \text{ ergs cm s}^{-1} M_{\odot}, \tag{6.6}$$

Simulation	M_{gas}	M_*	f_*	$\log Z_{gas}/Z_\odot$	$\log Z_*/Z_\odot$
	$10^6 M_\odot$				
Thermal	411.70	17.22	0.042	−1.39	−1.09
Kinetic	315.57	7.44	0.024	−1.57	−1.25
Stochastic	248.06	8.21	0.033	−1.52	−1.05
Mechanical	219.71	10.09	0.046	−1.25	−1.12

TABLE 6.1: Table showing the gas mass (M_{gas}), stellar mass (M_*), stellar fraction (f_*), gas metallicity ($\log Z_{gas}/Z_\odot$) and stellar metallicity ($\log Z_*/Z_\odot$) for the thermal, kinetic, stochastic and mechanical feedback simulations. Masses are shown in units of 10^6 $M_\odot$ and metallicities are normalized to solar.

where E_{SN} is the SNe energy for the timestep, n_H is the hydrogen number density and $\frac{Z}{Z_\odot}$ has a minimum value of 0.01.

Figure 6.3 compares the SFRs resulting from three parameters, f_k = 0.01, 0.1 0.25, and the thermal feedback model. As with the kinetic models, increasing f_k leads to decreasing SFR. In contrast to the thermal, kinetic and stochastic models mechanical feedback shows stronger SFR suppression at early times and gets progressively weaker, ultimately enhancing SFR at late times (t > 11 Gyr). This suggests that the boosted momentum provides a level of star formation suppression during the collapse of the gas cloud (possibly slowing the formation of the central gas disc) but is ineffective at suppressing star formation at late times (the additional momentum is not sufficient to overcome the lower thermal energy increase).

6.2.4 Selected Parameters

Based on the isolated gas disc SFR calculations we selected the parameters f_k = 0.1 for both the kinetic and mechanical models and f = 36 for the stochastic model. The properties for the simulated isolated dwarf galaxies at present time are shown in Table 6.1 for these parameters. The three enhanced feedback models successfully reduced the stellar mass formed, although this results in a slight decrease in metallicities. The stellar fraction was also reduced in the kinetic and stochastic models, however it increased slightly in the mechanical model due to the lower amount of gas left. This highlights the different mechanisms by which stellar feedback can suppress the SFR: by heating the gas to prevent collapse, by spreading out the gas out spatially and reducing the density, and by ejecting the gas from the galaxy entirely.

In Figure 6.4 we show the evolution of the central 10 kpc box for each chosen parameter. Each box shows the side on positions of the gas particles at a given time, coloured according to the projected metallicity of the gas. The models all show a bi-polar outflow of gas with the thermal model showing the most metal-rich ejected gas.
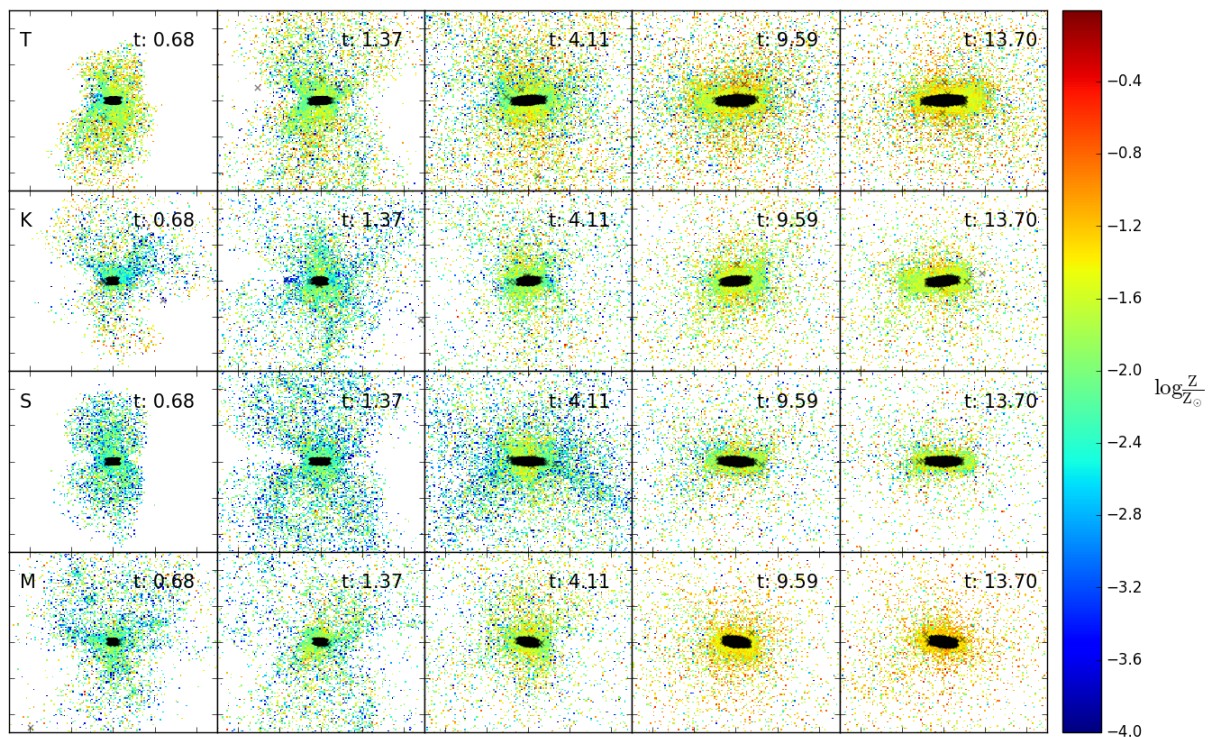
FIGURE 6.4: Positions of gas particles at time t (given in Gyr) in a 10 kpc box for thermal, kinetic, stochastic and mechanical models (by row in descending order) for the selected parameters. Bins (0.05 kpc) show the projected metallicity of metal enriched gas particles, provided $\log_{10}(Z/Z_\odot) > -4$. Black points show star particle positions.

Figure 6.5 shows the rate and composition of the galactic wind. We define wind particles as gas particles ejected over a spherical boundary with a radius of 500 kpc. Panel a) shows the rate of wind particles as a function of time. The thermal model shows the smallest amount of wind at all times. Both the kinetic and mechanical models start ejecting material approximately 1 Gyr earlier than the stochastic and thermal models, with the mechanical model ejecting a slightly larger amount of material. The stochastic model begins ejecting material later than the kinetic and mechanical models but ejects more material overall than the other three models. Panel b) shows the metallicity of the wind particles at a given time. The kinetic, stochastic and mechanical models result in similar metallicities but the thermal model is higher. Panel c) shows the rate of wind particle ejection, normalised by the total stellar mass contained within the 500 kpc ejection radius at that time. This acts as a measure of efficiency for each model (in the context of isolated dwarf disc galaxies). The thermal model is the least efficient, with the kinetic stochastic and mechanical models all ending with similar efficiencies. The stochastic model shows a peak in gas ejection just after 4 Gyr where it is significantly more efficient. The drop is due to the lower SFR as a result of the SNe feedback and gas ejection. Panel d) shows the rate of metal ejection normalised by the total metals in the simulation. Unlike panel b), this measure of metal ejection is independent of SFR, where higher metal ejection could be the result of greater metal production owing to greater SFR. This appears to be the case of the high
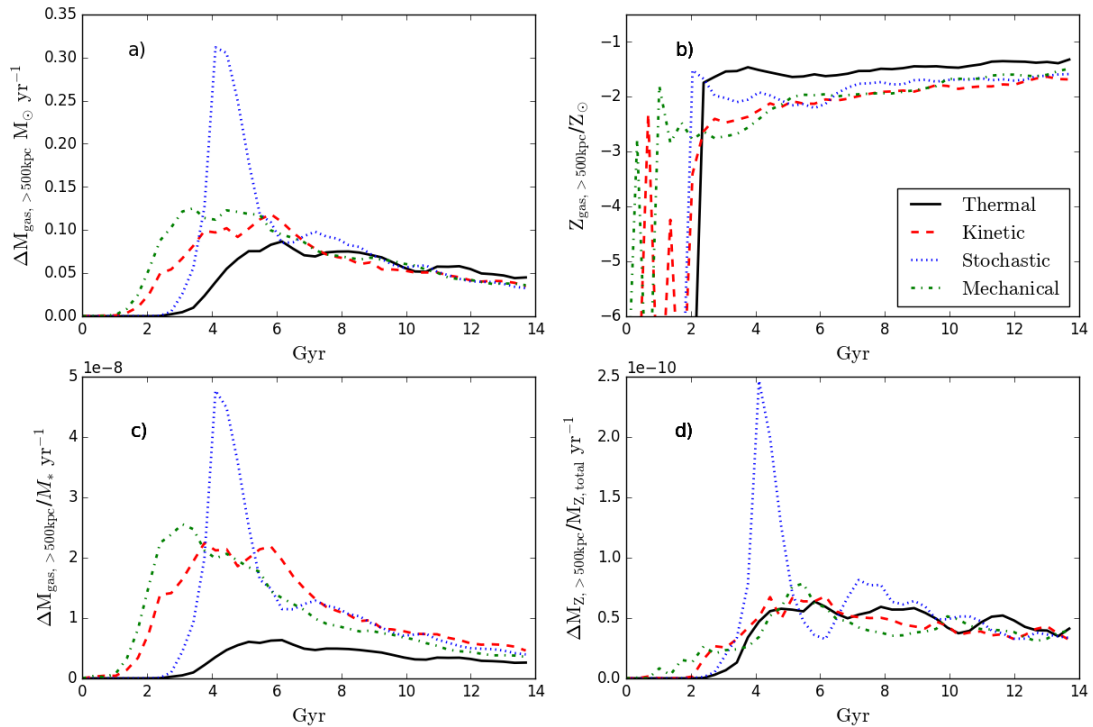
FIGURE 6.5: Plots showing the effect of feedback model on galactic wind for the thermal, kinetic, stochastic and mechanical models with selected parameters. Ejected particles are those that move over a 500 kpc spherical boundary. Panel a) shows the rate of ejected gas particles. Panel b) shows the metallicity of the newly ejected gas at each timestep normalised to solar metallicity. Panel c) shows the rate of ejected gas normalised by the stellar mass contained within the ejection radius. Panel d) shows the rate of ejected metals normalised by the total mass of metals.

metallicity of ejected gas seen in the thermal model; in this panel all models consistently eject a similar fraction of the total metals, with the exception of the stochastic ejection peak at 4 Gyr.

Additionally in Figure 6.6 we show the same panels as in Figure 6.5 but for the parameter tests for the stochastic model (using f = 12, 18, 24, and 36, along with the thermal model). Interestingly we found that using f = 18 resulted in a reasonable match with the thermal model in all four panels. Increasing f resulted in stronger wind (corresponding with decreased SFR), greater ejection efficiency and a larger fraction of metals ejected. This suggests that it is possible to have similar metal ejection as in the thermal model, though without the decreased SFR from the f = 36 model.

6.3 Milky Way Galaxies

In this section we use the selected parameters from the isolated dwarf disc galaxies to simulate Milky Way-type galaxies. We use initial conditions from Scannapieco et al. (2012) with cosmological parameters: $H_0 = 100h = 73$ km s^{-1} Mpc^{-1}, $\Omega_0 = 0.25$, $\Omega_\Lambda = 0.75$, $\Omega_B = 0.04$ with
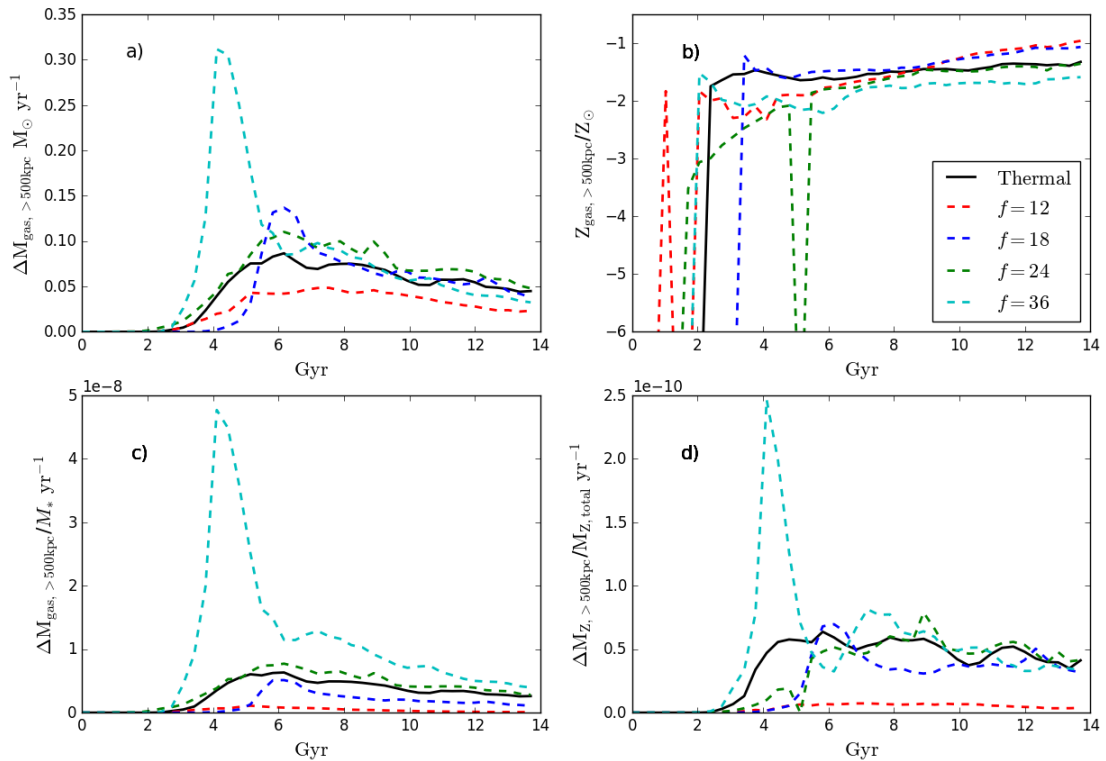
FIGURE 6.6: As Figure 6.5 but comparing stochastic feedback models with differing values of
f.

a gravitational softening length of 1 kpc h^{-1} and initial gas particle mass of $3.5 \times 10^6 M_\odot$. Two problems occurred with these simulations. The first was partially computational; the chosen parameter for the kinetic model proved far too strong and would entirely dismantle the gas disc by z=1. This in turn led to extremely long computational times, likely as a result of the unexpected number of particles at large distances. Reducing the parameter, eventually down to f_k, we found that the feedback was still far too strong and the runtime far too time consuming. Additionally, we found that the selected parameters for both the stochastic and mechanical models did not suppress the SFR as they had done in the isolated dwarf disc galaxies. Unfortunately, this suggests that the optimal parameters for isolated dwarf disc galaxies do not translate to the optimal parameters for Milky Way-type galaxies. In order to determine these we would require a parameter study using Milky Way-type galaxies. Nonetheless, we present the simulations completed thus far in this section, using the chosen parameters.

Table 6.2 shows the galactic properties for the simulated galaxies. We adopt the selected parameters from the previous section for the stochastic and mechanical models ($f = 36$ and $f_k = 0.1$ respectively). An effective solar neighbourhood is defined as in Chapter 4 and values are given for both the central 10 kpc disc with height ± 2 kpc and the solar neighbourhood. Unexpectedly, the thermal model shows the lowest stellar mass and stellar fraction in both cases. This can also be seen in Figure 6.8, where we show the SFRs for both the central disc (dashed lines) and the

	10 kpc disc					Solar Neighbourhood			
Simulation	M_{gas}	M_*	f_*	SFR	Effective SN	M_{gas}	M_*	f_*	SFR
	$10^9 \, M_\odot$			$M_\odot \, y^{-1}$	kpc	$10^9 \, M_\odot$			$M_\odot \, y^{-1}$
Thermal	10.54	97.17	0.90	40.12	5.571 - 7.285	1.60	4.00	0.71	4.30
Stochastic	10.04	113.37	0.92	85.41	5.850 - 7.650	1.22	4.72	0.79	2.43
Mechanical	10.26	104.31	0.91	37.17	5.083 - 6.647	1.46	6.38	0.81	4.78

TABLE 6.2: Properties for the simulated galaxies at $z = 0$ for the central 10 kpc disc with height ± 2 kpc and the effective solar neighbourhood. All masses are given in terms of $10^9 \, M_\odot$ and SFR is given in $M_\odot \, y^{-1}$.
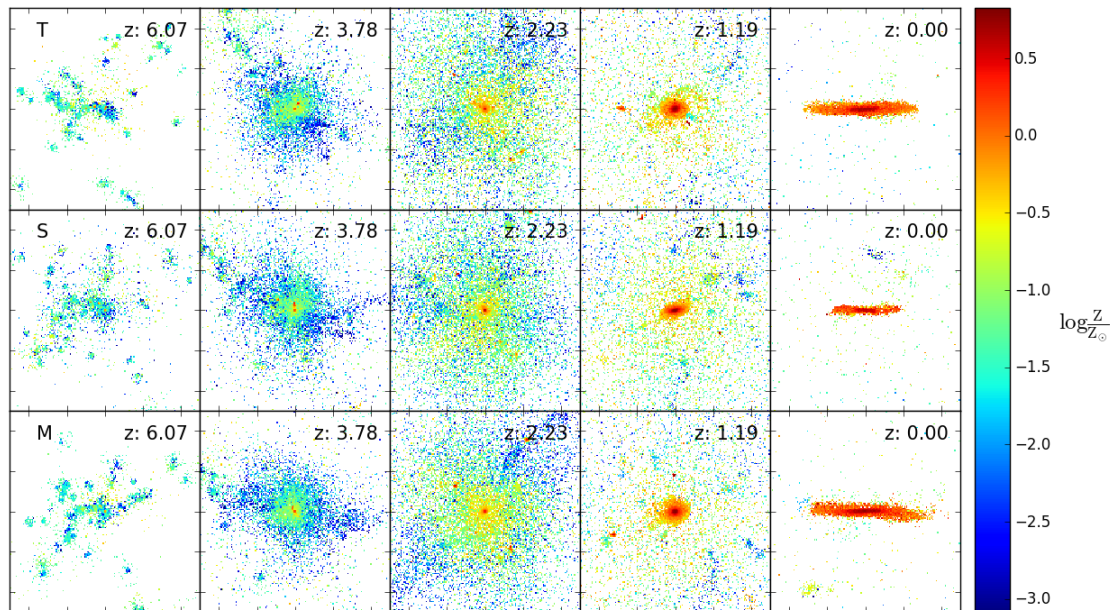
FIGURE 6.7: Positions of gas particles at redshift z within a 50 kpc box. Bins show the projected metallicity of gas particles with $Z/Z_\odot > -4$.

effective solar neighbourhood (solid lines). The stochastic and mechanical models both have higher SFRs than the thermal model, rather than supressing them.

One possible explanation for this is that the parameters adopted from the simpler isolated gas discs do not result in effective SFR rate suppression. Figure 6.2 shows that too low a choice of f results in stronger star formation than the thermal model in the isolated discs, suggesting that a higher parameter for the stochastic model may result in a lower SFR here. It is also worth noting that for the stochastic model, the change in the number of neighbour particles between the isolated gas discs and Milky Way-type simulations, from 36 to 64 respectively, should have had an effect. As the optimal choice of parameter appears to be approximately $f = N_{NGB}$ this also suggests that a high choice of f could reduce the SFR.

In Figure 6.9 we show the simulated galactic wind ejected over a radius of 1 Gpc. The panel
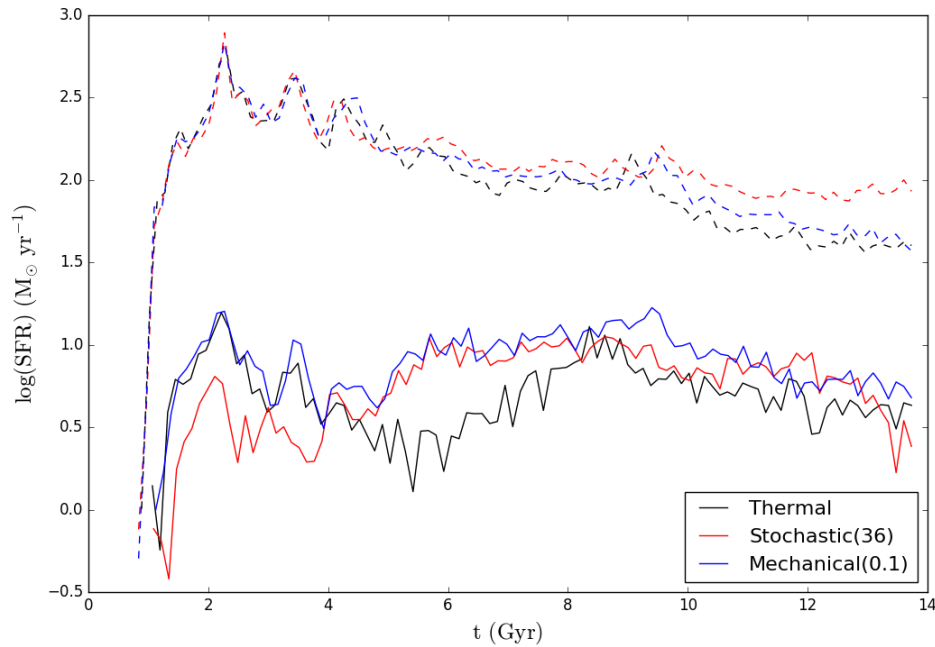
FIGURE 6.8: The SFR for the central 10 kpc disc with height ± 2 (dashed lines) and the solar neighbourhood (solid lines) for the thermal, stochastic and mechanical models.

layout is the same as used in Figure 6.5. Both the choice of feedback model and model parameter had a large impact on the galactic wind from the isolated dwarf disc galaxies. In particular, the ejection efficiency of the non-thermal models was significantly higher and resulted in greater mass ejection, even with lower SFR. However, the three Milky Way models show very little difference in wind rate, ejection efficiency of the metallicity of the ejected material. The stochastic model has a slightly higher ejection efficiency than the other two models. This leads to a second possible explanation for the lack of SFR suppression: that the steeper gravitational well is preventing efficient gas ejection, and it was this process that was reducing star formation rate within the isolated discs rather than gas heating.

To further examine this, we show the density-temperature phase space diagram in Figure 6.10. This shows the temperature and density relation for each gas particle with a central spherical volume with radius 1 Gpc in addition to showing the average distance from the centre for each bin. Each part of this figure shows a different region of the simulated galaxy. The central gas disc is comprised of the high density gas region, $\log_{10} n_H \gtrsim -1$. The large low density gas reserve $-7 \gtrsim \log_{10} n_H \gtrsim -4$ shows gas outside the main gas disc supplemented by heated gas ejected from the centre. The gas particles at $\log_{10} n_H \sim 0$ with elevated temperature are those heated by SNe feedback. The problem with the stochastic model can be seen clearly in this region; although gas particles are being heated (to a larger degree than the thermal and mechanical models), many of the particles left at lower temperatures and higher densities are more likely to form stars. A lower value of f would result in more star particles being heated, which might prevent the cooling. The mechanical model appears similar to the thermal model, with a slightly greater
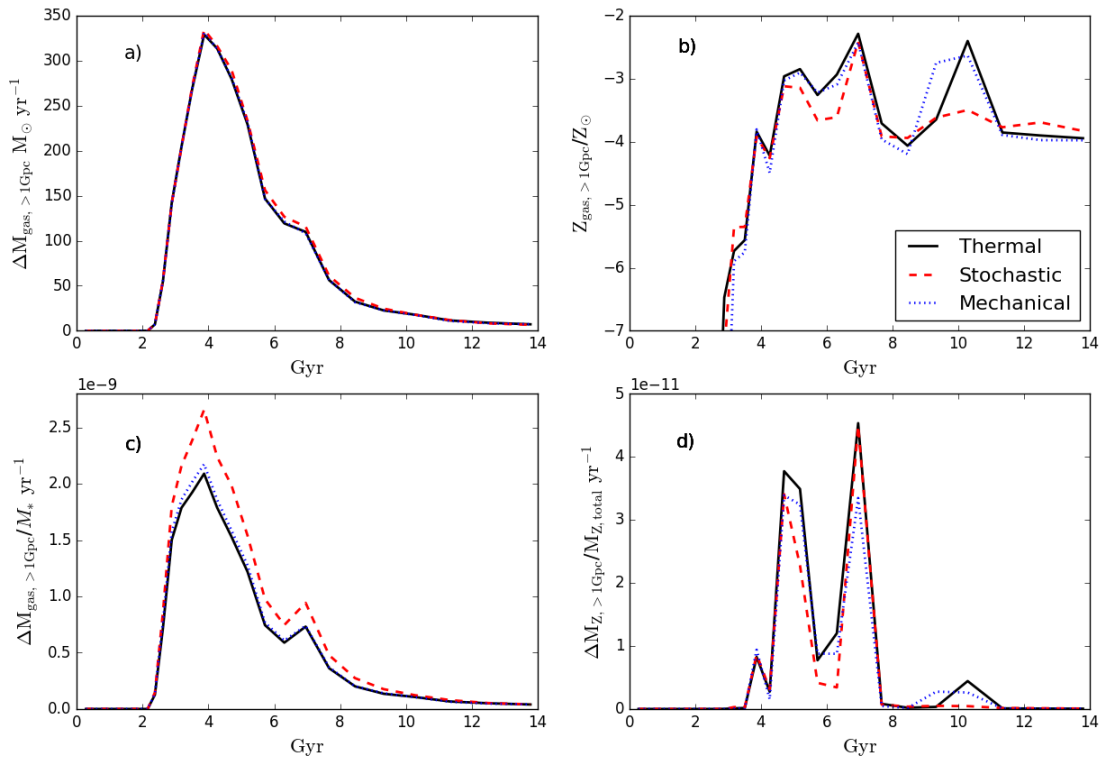
FIGURE 6.9: As Figure 6.5 but for the thermal, stochastic and mechanical models for the Milky Way-type galaxies, with an ejection radius of 1 Gpc.

number of high density particles. This is likely to be due to the slightly decreased thermal component.

6.4 Conclusions and Future Work

In this Chapter we have presented a comparison of four SNe feedback models: thermal, kinetic, stochastic and mechanical. Implementing them into models of isolated dwarf disc galaxies, we tested a number of parameters for them and we found that the kinetic ($f_k = 0.1$), stochastic ($f = 36$) and mechanical ($f_k = 0.1$) models decreased the SFR as intended. We additionally found that they did not proportionally eject more or less metals than the thermal model, however the metal content of galactic wind did vary naturally as a result of the lower SFR.

We then attempted to implement the feedback models into simulations of Milky Way-type galaxies and encountered several problems:

- Due to the increased mass, the kinetic feedback model becomes too efficient at ejecting material and would completely dismantle the gas disc.

- The stochastic and mechanical models adopting the parameters from the isolated gas disc models were showing an increased SFR, contrary to what was expected.
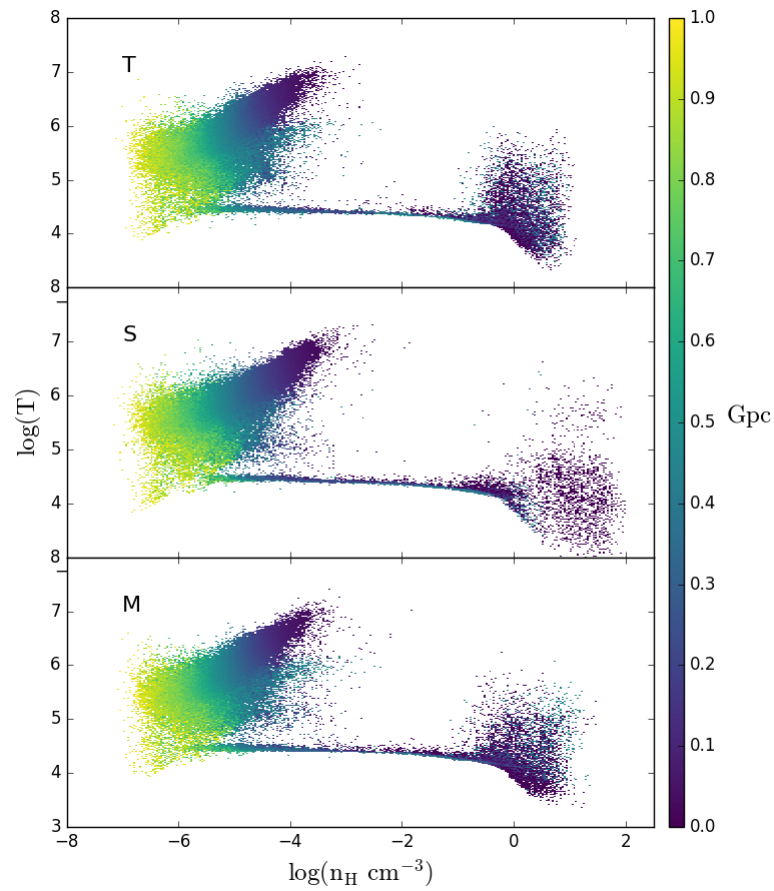
FIGURE 6.10: Density-temperature phase space diagram for the central sphere of radius 1 Gpc for the thermal, stochastic and mechanical models (T, S and M respectively). n_H is the hydrogen number density and the colour denotes distance in Gpc from the centre of the galactic disc.

One method to resolve these problems would be to determine parameters using Milky Way simulations for the kinetic, stochastic and mechanical models. In particular the stochastic model parameter affects both the energy a particle receives and how many particles are expected to receive it. This would be very time consuming however.

Chapter 7

Summary

In this Chapter I will present a brief summary of the work contained in this thesis.

In Chapter 2 I presented the theory and background behind the nucleosynthesis processes that could contribute to the creation of elements heavier than iron. Of these processes, the slow and rapid neutron capture processes were best able to explain the chemical abundances we observe today. I further examined some of the potential sites where the conditions for these processes were able to occur:

- A strong s-process in the thermal pulses of low mass AGB stars via the ^{13}C neutron source.

- A weak s-process in high mass AGB stars via the ^{22}Ne neutron source.

- A strong r-process source in the dynamic and neutron-rich ejecta of merging neutron stars.

- A strong r-process source in the supernovae of highly magnetised and rapidly rotating massive stars, ejected by polar jets.

- A weak r-process source in electron capture supernovae.

- A weak r-process source in the neutrino driven winds of supernovae.

I presented in Chapter 3 an overview of the chemodynamical code used in the simulations, including the hydrodynamics, star formation process, chemical enrichment, supernova yields and supernova feedback. I then discussed the implementation of the processes I examined in Chapter 2 into the code. Yields were adopted for AGB stars and included in the chemical enrichment. For neutron star mergers, yields and a delay time distribution for formation and coalescence of binary neutron stars were adopted and combined to simulate the dynamic ejecta. Magneto-rotational supernova yields were adopted and used to replace a fraction of high mass supernovae events with an adjustable parameter. Electron capture supernova yields were included with a

metallicity dependent mass range and neutrino driven wind yields were added for stars with $M > 13M_\odot$. I also present here the implementation of several alternative supernova feedback models in addition to the thermal and kinetic models already available: a stochastic model designed to heat a smaller number of particles by a fixed energy and a mechanical model designed to take into account the work done during the Sedov Taylor phase of supernova expansion.

In Chapter 4 I presented my first paper, previously accepted and published in Monthly Notices of the Royal Astronomical Society, largely unchanged. In it I presented chemodynamical simulations comparing NS mergers, MRSNe, ECSNe and neutrino winds in the context of both isolated dwarf disc galaxies and Milky Way-type galaxies. Using analysis of the [Eu/(Fe,α)] - [Fe/H] relations I concluded that, although NS mergers likely contribute to the galactic r-process, they are unable to explain early, low [Fe/H] r-process enrichment and that an additional r-process site, such as MRSNe, would be required to match observations.

In Chapter 5 I presented my second paper, largely ready for submission, that further examined the role of MRSNe as a the driver of early galactic r-process enrichment. In particular, I adopted the Z-dependency of hypernovae and applied this to the MRSNe model on the basis that the rotation condition for MRSNe would be hampered by angular momentum loss due to increased metallicity. I compared this ZMRSNe model with NS merger models for Chapter 4 and presented a combined ECSNe, NS mergers and ZMRSNe model that was able to reproduce low metallicity observations for Eu, Nd, Dy, Er and Zr very well and this provided an improvement on my previous paper.

In Chapter 6 I presented final paper comparing the thermal and kinetic feedback models to the stochastic and mechanical feedback models. I found that the models worked well in the parameter study using isolated dwarf disc galaxies, and were able to suppress SFR when compared to the thermal model. Although it appears that the metallicity of the galactic wind was increase in the thermal model, it appears that this is due to the higher SFR. The chosen parameters did not translate well to the Milky Way-type galaxies, although feedback appears to be inefficient in MW type galaxies. This will require further study of the parameters for MW type galaxies.

7.0.1 Key Conclusions

The primary conclusions drawn from this work are listed below:

- MRSNe are shown to play an important role in the early r-process (traced by europium, dysprosium, neodymium and ytterbium) enrichment of Milky Way type galaxies. In the case of europium enrichment, this holds for both [Eu/Fe] and [Eu/α].

- NS mergers alone are unable to account for r-process enrichment in the early Milky Way, despite being able to produce stars with solar [Eu/Fe] abundances at solar [Fe/H].

- MRSNe with an metallicity dependence adopted from studies of HNe and combined with NS mergers are able to accurately reproduce r-process trends.

7.0.2 Future Work

Finally here I list future work I would like to undertake myself and other future work that would be beneficial to galactic archaeology:

- Higher resolution runs of the combined NS merger and ZMRSNe model presented in Chapter 5. The simulation code includes inital conditions at two higher resolutions, so the primary limiting factor is the long run times required (a rough estimation of at least six months for the lower of the higher resolutions). This would allow me to better discuss any resolution dependence and provide a much larger sample of low [Fe/H] star particles for comparison to observations.

- In Chapter 5 I found that the simulated [Ba/Fe] matched poorly with the observed trend, particularly at low [Fe/H]. In order to address this I would like to run simulations comparing the effects of the new AGB yields on s-process production. Additionally, updated yields from rapidly rotating stars may have increased s-process production (disucssed in Chapter 5); I would like to modify the code to include these in a similar way to MRSNe (including these in conjunction with MRSNe may prove challenging as both have similar progenitor stars).

- I would like to compare the effects of NS merger DTDs and the effect the choice has on [Eu/Fe] – [Fe/H]. In particular, I would be interested to see the effect DTD choice could have on the slope gradient at solar [Fe/H]. It currently appears unlikely that DTD choice could enable NS mergers to explain r-process abundance patterns alone, however a study into DTD choice would still prove valuable.

- The Milky Way feedback parameter testing discussed in Chapter 6. The parameter selection based on the isolated dwarf disc galaxies did not produce the same effects when transferred to the Milky Way type galaxies; a study of these parameters using Milky Way type galaxies may result in an improved feedback model. In particular I would interested to see the effects on r-process nucleosynthesis.

Bibliography

Abbott, B.P., Abbott, R., Abbott, T.D., et al., 2017a. Gravitational Waves and Gamma-Rays from a Binary Neutron Star Merger: GW170817 and GRB 170817A. *ApJ*, 848:L13.

Abbott, B.P., Abbott, R., Abbott, T.D., et al., 2017b. GW170817: Observation of Gravitational Waves from a Binary Neutron Star Inspiral. *Physical Review Letters*, 119(16):161101.

Anders, E. and Grevesse, N., 1989. Abundances of the elements - Meteoritic and solar. *Geochimica et Cosmochimica Acta*, 53:197.

Arcones, A., Janka, H.T., and Scheck, L., 2007. Nucleosynthesis-relevant conditions in neutrino-driven supernova outflows. I. Spherically symmetric hydrodynamic simulations. *A&A*, 467:1227.

Argast, D., Samland, M., Thielemann, F.K., et al., 2004. Neutron star mergers versus core-collapse supernovae as dominant r-process sites in the early Galaxy. *A&A*, 416:997.

Arnould, M. and Goriely, S., 2003. The p-process of stellar nucleosynthesis: astrophysics and nuclear physics status. *Physics Reports*, 384:1.

Beer, H. and Macklin, R.L., 1989. Measurement of the Rb-85 and Rb-87 capture cross sections for s-process studies. *ApJ*, 339:962.

Beniamini, P., Hotokezaka, K., and Piran, T., 2016. Natal Kicks and Time Delays in Merging Neutron Star Binaries: Implications for r-process Nucleosynthesis in Ultra-faint Dwarfs and in the Milky Way. *ApJ*, 829:L13.

Beniamini, P. and Piran, T., 2019. The Gravitational waves merger time distribution of binary neutron star systems. *MNRAS*, 487:4847.

Berger, M.J. Colella, P., 1989. Local adaptive mesh refinement for shock hydrodynamics. *Journal of Computational Physics*, 82:64.

Bisterzo, S., Gallino, R., Straniero, O., et al., 2011. The s-process in low-metallicity stars - II. Interpretation of high-resolution spectroscopic observations with asymptotic giant branch models. *MNRAS*, 418:284.

Buder, S., Asplund, M., Duong, L., et al., 2018. The GALAH Survey: Second Data Release. *MNRAS*.

Burbidge, E.M., Burbidge, G.R., Fowler, W.A., et al., 1957. Synthesis of the Elements in Stars. *Reviews of Modern Physics*, 29:547.

Cameron, A.G.W., 1957. NUCLEAR REACTIONS IN STARS AND NUCLEOGENESIS. *Astronomical Society of the Pacific*, 69:201.

Cameron, A.G.W., 1960. New Neutron Sources of Possible Astrophysical Importance. *aj*, 65:485.

Cameron, A.G.W., 2001. Some Properties of r-Process Accretion Disks and Jets. *ApJ*, 562:456.

Cameron, A.G.W., 2003. Some Nucleosynthesis Effects Associated with r-Process Jets. *ApJ*, 587:327.

Cescutti, G., Romano, D., Matteucci, F., et al., 2015. The role of neutron star mergers in the chemical evolution of the Galactic halo. *A&A*, 577:A139.

Chiappini, C., Frischknecht, U., Meynet, G., et al., 2011. Imprints of fast-rotating massive stars in the Galactic Bulge. *Nature*, 472:454.

Côté, B., Eichler, M., Arcones, A., et al., 2018. Neutron Star Mergers Might not be the Only Source of r-Process Elements in the Milky Way. *ArXiv e-prints*.

Cowan, J.J. and Rose, W.K., 1977. Production of C-14 and neutrons in red giants. *Astrophysical Journal*, 212:149.

Crain, R.A., McCarthy, I.G., Schaye, J., et al., 2013. Enriching the hot circumgalactic medium. *MNRAS*, 432:3005.

Crain, R.A., Schaye, J., Bower, R.G., et al., 2015. The EAGLE simulations of galaxy formation: calibration of subgrid physics and model variations. *MNRAS*, 450:1937.

Dalla Vecchia, C. and Schaye, J., 2008. Simulating galactic outflows with kinetic supernova feedback. *MNRAS*, 387:1431.

Dalla Vecchia, C. and Schaye, J., 2012. Simulating galactic outflows with thermal supernova feedback. *MNRAS*, 426:140.

Doherty, C.L., Gil-Pons, P., Siess, L., et al., 2015. Super- and massive AGB stars - IV. Final fates - initial-to-final mass relation. *MNRAS*, 446:2599.

Freiburghaus, C., Rembges, J.F., Rauscher, T., et al., 1999a. The Astrophysical r-Process: A Comparison of Calculations following Adiabatic Expansion with Classical Calculations Based on Neutron Densities and Temperatures. *ApJ*, 516:381.

Freiburghaus, C., Rosswog, S., and Thielemann, F.K., 1999b. R-Process in Neutron Star Mergers. *ApJ*, 525:L121.

Frischknecht, U., Hirschi, R., Pignatari, M., et al., 2016. s-process production in rotating massive stars at solar and low metallicities. *MNRAS*, 456:1803.

Fröhlich, C., Martínez-Pinedo, G., Liebendörfer, M., et al., 2006. Neutrino-Induced Nucleosynthesis of A>64 Nuclei: The νp Process. *Physical Review Letters*, 96(14):142502.

Gallino, R., Arlandini, C., Busso, M., et al., 1998. Evolution and Nucleosynthesis in Low-Mass Asymptotic Giant Branch Stars. II. Neutron Capture and the S-Process. *ApJ*, 497:388.

Gilroy, K.K., Sneden, C., Pilachowski, C.A., et al., 1988. Abundances of neutron capture elements in Population II stars. *ApJ*, 327:298.

Gingold, R.A. and Monaghan, J.J., 1977. Smoothed particle hydrodynamics - Theory and application to non-spherical stars. *MNRAS*, 181:375.

Hansen, C.J., Nordström, B., Hansen, T.T., et al., 2016. Abundances of carbon-enhanced metal-poor stars as constraints on their formation. *A&A*, 588:A37.

Hansen, T.T., Holmbeck, E.M., Beers, T.C., et al., 2018. The R-process Alliance: First Release from the Southern Search for R-process-enhanced Stars in the Galactic Halo. *ApJ*, 858:92.

Haynes, C.J. and Kobayashi, C., 2019. Galactic simulations of r-process elemental abundances. *MNRAS*, 483:5123.

Hernquist, L. and Katz, N., 1989. TREESPH - A unification of SPH with the hierarchical tree method. *ApJ*, 70:419.

Honda, S., Aoki, W., Ishimaru, Y., et al., 2006. Neutron-Capture Elements in the Very Metal Poor Star HD 122563. *ApJ*, 643:1180.

Hopkins, P.F., Kereš, D., Oñorbe, J., et al., 2014. Galaxies on FIRE (Feedback In Realistic Environments): stellar feedback explains cosmologically inefficient star formation. *MNRAS*, 445:581.

Iben, Jr., I. and Renzini, A., 1982a. On the formation of carbon star characteristics and the production of neutron-rich isotopes in asymptotic giant branch stars of small core mass. *ApJ*, 263:L23.

Iben, Jr., I. and Renzini, A., 1982b. The role of semiconvection in bringing carbon to the surface of asymptotic giant branch stars of small core mass. *ApJ*, 259:L79.

Janka, H.T., 2012. Explosion Mechanisms of Core-Collapse Supernovae. *Annual Review of Nuclear and Particle Science*, 62:407.

Ji, A.P., Frebel, A., Simon, J.D., et al., 2016. Complete Element Abundances of Nine Stars in the r-process Galaxy Reticulum II. *ApJ*, 830:93.

Käppeler, F., Gallino, R., Bisterzo, S., et al., 2011. The s process: Nuclear physics, stellar models, and observations. *Reviews of Modern Physics*, 83:157.

Karakas, A.I., 2010. Updated stellar yields from asymptotic giant branch models. *MNRAS*, 403:1413.

Karakas, A.I., García-Hernández, D.A., and Lugaro, M., 2012. Heavy Element Nucleosynthesis in the Brightest Galactic Asymptotic Giant Branch Stars. *ApJ*, 751:8.

Karakas, A.I. and Lugaro, M., 2016. Stellar Yields from Metal-rich Asymptotic Giant Branch Models. *ApJ*, 825:26.

Katz, N., 1992. Dissipational galaxy formation. ii-effects of star formation. *ApJ*, 391:502.

Kobayashi, C., 2004. GRAPE-SPH chemodynamical simulation of elliptical galaxies - I. Evolution of metallicity gradients. *MNRAS*, 347:740.

Kobayashi, C., 2005. GRAPE-SPH chemodynamical simulation of elliptical galaxies - II. Scaling relations and the fundamental plane. *MNRAS*, 361:1216.

Kobayashi, C., Karakas, A.I., and Umeda, H., 2011. The evolution of isotope ratios in the Milky Way Galaxy. *MNRAS*, 414:3231.

Kobayashi, C. and Nakasato, N., 2011. Chemodynamical Simulations of the Milky Way Galaxy. *ApJ*, 729:16.

Kobayashi, C. and Nomoto, K., 2009. The Role of Type Ia Supernovae in Chemical Evolution. I. Lifetime of Type Ia Supernovae and Metallicity Effect. *ApJ*, 707:1466.

Kobayashi, C., Nomoto, K., and Hachisu, I., 2015. Subclasses of Type Ia Supernovae as the Origin of [α/Fe] Ratios in Dwarf Spheroidal Galaxies. *ApJ*, 804:L24.

Kobayashi, C., Springel, V., and White, S.D.M., 2007a. Simulations of Cosmic Chemical Enrichment. *MNRAS*, 376:1465.

Kobayashi, C., Springel, V., and White, S.D.M., 2007b. Simulations of Cosmic Chemical Enrichment. *MNRAS*, 376:1465.

Kodama, T. and Arimoto, N., 1997. Origin of the colour-magnitude relation of elliptical galaxies. *A&A*, 320:41.

Korobkin, O., Rosswog, S., Arcones, A., et al., 2012. On the astrophysical robustness of the neutron star merger r-process. *MNRAS*, 426:1940.

Kroupa, P., 2001. On the variation of the initial mass function. *MNRAS*, 322:231.

Kroupa, P., 2008. The IMF of Simple and Composite Populations. In J.H. Knapen, T.J. Mahoney, and A. Vazdekis, editors, *Pathways Through an Eclectic Universe*, volume 390 of *Astronomical Society of the Pacific Conference Series*, page 3.

Lattimer, J.M. and Schramm, D.N., 1974. Black-hole-neutron-star collisions. *ApJ*, 192:L145.

Lucy, L.B., 1977. A numerical approach to the testing of the fission hypothesis. *AJ*, 82:1013.

Lugaro, M., Ugalde, C., Karakas, A.I., et al., 2004. Reaction Rate Uncertainties and the Production of ^{19}F in Asymptotic Giant Branch Stars. *ApJ*, 615:934.

Mackereth, J.T., Crain, R.A., Schiavon, R.P., et al., 2018. The origin of diverse α-element abundances in galaxy discs. *MNRAS*, 477:5072.

Maoz, D., Mannucci, F., and Nelemans, G., 2014. Observational Clues to the Progenitors of Type Ia Supernovae. *Annual Review of Astronomy and Astrophysics*, 52:107.

Mennekens, N. and Vanbeveren, D., 2014. Massive double compact object mergers: gravitational wave sources and r-process element production sites. *A&A*, 564:A134.

Merrill, P., 1952. Spectroscopic observations of stars of class Md. *Astrophysics Journal*, 116.

Metzger, B.D. and Fernández, R., 2014. Red or blue? A potential kilonova imprint of the delay until black hole formation following a neutron star merger. *MNRAS*, 441:3444.

Miyaji, S., Sugimoto, D., Nomoto, K., et al., 1980. Supernova explosion triggered by electron capture and formation of a neutron star. *International Cosmic Ray Conference*, 2:13.

Mösta, P., Roberts, L.F., Halevi, G., et al., 2018. r-process Nucleosynthesis from Three-dimensional Magnetorotational Core-collapse Supernovae. *ApJ*, 864:171.

Navarro, J.F. and White, S.D.M., 1993. Simulations of Dissipative Galaxy Formation in Hierarchically Clustering Universes - Part One - Tests of the Code. *MNRAS*, 265:271.

Nishimura, N., Takiwaki, T., and Thielemann, F.K., 2015. The r-process Nucleosynthesis in the Various Jet-like Explosions of Magnetorotational Core-collapse Supernovae. *ApJ*, 810:109.

Nomoto, K., Iwamoto, K., Nakasato, N., et al., 1997. Nucleosynthesis in type Ia supernovae. *Nuclear Physics A*, 621:467.

Ojima, T., Ishimaru, Y., Wanajo, S., et al., 2017. Stochastic Chemical Evolution of Sub-Halos and the Origin of r-Process Elements. In S. Kubono, T. Kajino, S. Nishimura, T. Isobe, S. Nagataki, T. Shima, and Y. Takeda, editors, *14th International Symposium on Nuclei in the Cosmos (NIC2016)*, page 020208.

Ojima, T., Ishimaru, Y., Wanajo, S., et al., 2018. Stochastic Chemical Evolution of Galactic Subhalos and the Origin of r-process Elements. *ApJ*, 865:87.

Prantzos, N., Hashimoto, M., and Nomoto, K., 1990. The s-process in massive stars - Yields as a function of stellar mass and metallicity. *A&A*, 234:211.

Roederer, I.U., 2017. The Origin of the Heaviest Metals in Most Ultra-faint Dwarf Galaxies. *ApJ*, 835:23.

Roederer, I.U., Cowan, J.J., Karakas, A.I., et al., 2010. The Ubiquity of the Rapid Neutron-capture Process. *ApJ*, 724:975.

Roederer, I.U., Preston, G.W., Thompson, I.B., et al., 2014. A Search for Stars of Very Low Metal Abundance. VI. Detailed Abundances of 313 Metal-poor Stars. *aj*, 147:136.

Ruffert, M., Janka, H.T., and Schaefer, G., 1996. Coalescing neutron stars - a step towards physical models. I. Hydrodynamic evolution and gravitational-wave emission. *A&A*, 311:532.

Scannapieco, C., Wadepuhl, M., Parry, O.H., et al., 2012. The Aquila comparison project: the effects of feedback and numerical methods on simulations of galaxy formation. *MNRAS*, 423:1726.

Shen, S., Cooke, R.J., Ramirez-Ruiz, E., et al., 2015. The History of R-Process Enrichment in the Milky Way. *ApJ*, 807:115.

Shen, S., Wadsley, J., and Stinson, G., 2010. The enrichment of the intergalactic medium with adiabatic feedback - I. Metal cooling and metal diffusion. *MNRAS*, 407:1581.

Shibata, M. and Uryū, K.ō., 2000. Simulation of merging binary neutron stars in full general relativity: Γ=2 case. *Physical Review D*, 61(6):064001.

Smith, M.C., Sijacki, D., and Shen, S., 2018. Supernova feedback in numerical simulations of galaxy formation: separating physics from numerics. *MNRAS*, 478:302.

Smith, V.V. and Lambert, D.L., 1986. The chemical composition of red giants. II - Helium burning and the s-process in the MS and S stars. *ApJ*, 311:843.

Smith, V.V. and Lambert, D.L., 1990. The chemical composition of red giants. III - Further CNO isotopic and s-process abundances in thermally pulsing asymptotic giant branch stars. *ApJ*, 72:387.

Sneden, C., Cowan, J.J., and Gallino, R., 2008. Neutron-Capture Elements in the Early Galaxy. *Annual Review of Astronomy and Astrophysics*, 46:241.

Sneden, C. and Parthasarathy, M., 1983. The r- and s-process nuclei in the early history of the galaxy - HD 122563. *ApJ*, 267:757.

Sneden, C., Preston, G.W., McWilliam, A., et al., 1994. Ultrametal-poor halo stars: The remarkable spectrum of CS 22892-052. *ApJ*, 431:L27.

Springel, V., 2005. The cosmological simulation code GADGET-2. *MNRAS*, 364:1105.

Springel, V. and Hernquist, L., 2002. Cosmological smoothed particle hydrodynamics simulations: the entropy equation. *MNRAS*, 333:649.

Springel, V. and Hernquist, L., 2003. Cosmological smoothed particle hydrodynamics simulations: a hybrid multiphase model for star formation. *MNRAS*, 339:289.

Sterling, N.C. and Dinerstein, H.L., 2008. The Abundances of Light Neutron-Capture Elements in Planetary Nebulae. II. s-Process Enrichments and Interpretation. *ApJ*, 174:158.

Stinson, G., Seth, A., Katz, N., et al., 2006. Star formation and feedback in smoothed particle hydrodynamic simulations - I. Isolated galaxies. *MNRAS*, 373:1074.

Sutherland, R. and Dopita, M., 1993. Cooling functions for low-density astrophysical plasmas. *ApJ*, 88:253 .

Tanaka, M., Utsumi, Y., Mazzali, P.A., et al., 2017. Kilonova from post-merger ejecta as an optical and near-Infrared counterpart of GW170817. *Publications of the Astronomical Society of Japan*, 69:102.

Taylor, P. and Kobayashi, C., 2014. Seeding black holes in cosmological simulations. *MNRAS*, 442:2751.

Teyssier, R., Pontzen, A., Dubois, Y., et al., 2013. Cusp-core transformations in dwarf galaxies: observational predictions. *MNRAS*, 429:3068.

Tolstoy, E., Hill, V., and Tosi, M., 2009. Star-Formation Histories, Abundances, and Kinematics of Dwarf Galaxies in the Local Group. *Annual Review of Astronomy and Astrophysics*, 47:371.

Valenti, S., David, Sand, J., et al., 2017. The Discovery of the Electromagnetic Counterpart of GW170817: Kilonova AT 2017gfo/DLT17ck. *ApJ*, 848:L24.

van Aarle, E., Van Winckel, H., De Smedt, K., et al., 2013. Detailed abundance study of four s-process enriched post-AGB stars in the Large Magellanic Cloud. *A&A*, 554:A106.

van de Voort, F., Quataert, E., Hopkins, P.F., et al., 2015. Galactic r-process enrichment by neutron star mergers in cosmological simulations of a Milky Way-mass galaxy. *MNRAS*, 447:140.

Wanajo, S., 2007. Cold r-Process in Neutrino-driven Winds. *ApJ*, 666:L77.

Wanajo, S., 2013. The r-process in Proto-neutron-star Wind Revisited. *ApJ*, 770:L22.

Wanajo, S., Janka, H.T., and Müller, B., 2011. Electron-capture Supernovae as The Origin of Elements Beyond Iron. *ApJ*, 726:L15.

Wanajo, S., Janka, H.T., and Müller, B., 2013. Electron-capture Supernovae as Origin of ^{48}Ca. *ApJ*, 767:L26.

Wanajo, S., Kajino, T., Mathews, G.J., et al., 2001. The r-Process in Neutrino-driven Winds from Nascent, "Compact" Neutron Stars of Core-Collapse Supernovae. *ApJ*, 554:578.

Wanajo, S., Sekiguchi, Y., Nishimura, N., et al., 2014. Production of All the r-process Nuclides in the Dynamical Ejecta of Neutron Star Mergers. *ApJ*, 789:L39.

Wehmeyer, B., Pignatari, M., and Thielemann, F.K., 2015. Galactic evolution of rapid neutron capture process abundances: the inhomogeneous approach. *MNRAS*, 452:1970.

Wiersma, R.P.C., Schaye, J., Theuns, T., et al., 2009. Chemical enrichment in cosmological, smoothed particle hydrodynamics simulations. *MNRAS*, 399:574.

Winteler, C., Käppeli, R., Perego, A., et al., 2012. Magnetorotationally Driven Supernovae as the Origin of Early Galaxy r-process Elements? *ApJ*, 750:L22.

Woosley, S.E., Hartmann, D.H., Hoffman, R.D., et al., 1990. The nu-process. *Astrophysical Journal*, 356:272.

Zhao, G., Mashonkina, L., Yan, H.L., et al., 2016. Systematic Non-LTE Study of the $-.6 \leq$ [Fe/H] ≤ 0.2 F and G Dwarfs in the Solar Neighborhood. II. Abundance Patterns from Li to Eu. *ApJ*, 833:225.